

國立交通大學

電子物理研究所
博士論文

邊界效應對高階雷射模態之產生和雷射
激發水柱之噴濺的影響

Boundary effects on generation of
high-order laser modes and morphology of
laser-induced water jets

研究生：陳建至

指導教授：陳永富 教授

中華民國 102 年 5 月

邊界效應對高階雷射模態之產生和雷射激發水柱之噴濺的影響

Boundary effects on generation of high-order laser modes and morphology
of laser-induced water jets

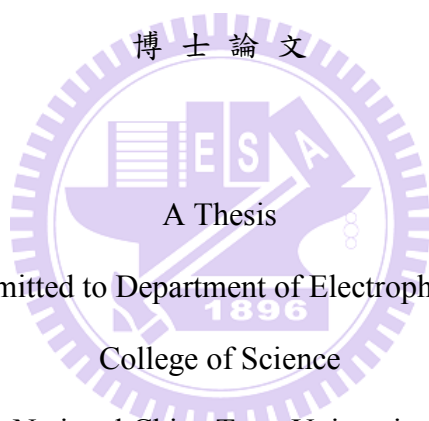
研究生：陳建至 Student : Ross C. C. Chen

指導教授：陳永富 Advisor : Yung-Fu Chen

國立交通大學

電子物理學系

博士論文



Submitted to Department of Electrophysics

College of Science

National Chiao Tung University

in partial Fulfillment of the Requirements

for the Degree of

PhD

In

Electrophysics

May 2013

Hsinchu, Taiwan, Republic of China

中華民國一百零二年五月

邊界效應對高階雷射模態之產生和雷射激發水柱之噴 濺的影響

學生：陳建至

指導教授：陳永富

國立交通大學電子物理學系博士班



摘要

本文的第一部分，利用半導體雷射VCSEL類比研究橫向邊界下的橫向高階模態，並且從近場至遠場的觀察，研究橫向模態出光的特性和方向性。相較於微腔體發光元件之出光特性的研究，利用VCSEL可以更直接的觀察到其模態的空間演進。從研究結果中，我們證明了近場橫向模態和出光的方向性並非絕對一對一的關係。當近場橫向模態有著圖像上顯著的差異，其遠場仍有可能具有大致相同的方向性。更進一步，我們藉由量子彈子球檯的模型和近軸光學的繞射來理論分析觀察到的實驗結果。

第二部分，我們對雷射激發水柱之噴濺的形成作了深入的研究。將雷射垂直聚焦入射於水面之下，利用高速攝影觀察水面上之噴濺的行為，並針對其結構和形成機制做了細節的探討。在水柱於空間行進的演化中，水柱中間會產生一個氣泡，並且在適當的雷射聚焦深度下，此氣泡中會包含一顆水滴。此外，由於雷射產生的電漿具有很大的動能平行於入射方向，因此當我們將雷射水平入射聚焦於水中時，水面的噴濺將不再是柱對稱結構，具有平面結構的特徵變化。

Boundary effects on generation of high-order laser modes and morphology of laser-induced water jets

Student: Ross C. C. Chen

Advisor: Prof. Yung-Fu Chen

Institute and Department of Electrophysics
National Chiao-Tung University

Abstract

In this work, we investigate the high-order laser modes by a large-aperture VCSEL in different shapes of transverse confinement. VCSELs bear the potential to allow for directly observing the transverse modes and its free space propagation. Additionally, the light emitted from VCSEL is meaningful for studying the time diffraction from a high-order quantum mode. The experiment is reconstructed very well by theories of quantum billiard and Fresnel diffraction. We show that the far-field directional emission from a microcavity is just a necessary not sufficient condition for the emergence of a superscar mode.

In next part, we investigate the laser-induced liquid jet. A pulsed laser is vertically focused into a tap water to induce a water jet on a flat water surface. The water jet is observed by a high speed camera and the mechanism is discussed in detail. In the temporal evolution of the water jet, there is an air bubble with a water drop inside formed in the water jet. Additionally, we horizontally focus the laser beam into the water and observe the water jet. This water jet shows a sheet features.

誌謝

Acknowledgement

進入實驗室是在大學三年級的時候，之後逕讀博士到畢業共六年的研究生涯，其中，曾一度隨著自己的任性與興趣而徘徊或中斷，但最後終於完成了它。這六年中，非常感謝陳永富老師對我的提攜、關懷與照顧。在這浩瀚無垠的知識，永無止盡求學之道，能遇到兼具實作經驗及深厚理論分析能力的陳老師，指引著我如何做研究。陳老師的因材施教更讓學生能夠對於自己的長處有所發揮，並學習獨立思考和自我要求。與陳老師互動討論，著實讓我受益良多。另一個要感謝的是黃凱風老師。學識淵博的黃老師，總是能以清晰的物理圖像解釋實驗及理論結果，並給予關於研究更好的建議，更是讓我欽佩不已。總之，縱有千言萬語，也無法表達我對這兩位老師的感激之情。

再來要感謝的是在研究求學期間給予我無限支持及鼓勵的家人及朋友，感謝我的父親陳振芳教授對我的研究和論文寫作的幫助，感謝母親讓我在每一天的研究完回家時能有一頓豐盛的晚餐，並時時關心我的狀況；感謝我阿姨和外婆對我的呵護；感謝陸爸爸陸媽媽一家對我的關愛及鼓勵。這些重要的人陪伴我走過無數的困頓、煩憂。

最後，感謝蘇老大在實驗上的指導和獨到的見解，感謝教導我做實驗的建誠和彥廷學長，感謝他們的熱心分享所學。非常感謝實驗室的同仁興弛學長、亭樺學姊、依萍學姊、雅婷學姊、哲彥學長、仕璋學長、漢龍學長、小江、文政、易純、威哲、毅帆、毓捷、郁仁、舜子、國維、威霖、凱勝、容辰、段必、小佑、及政猷，使我的研究所生涯更豐碩。

誠摯感謝實驗室的各位帶給我的一切，讓我能砥礪自我並更向前邁進。

Content

Abstract (Chinese)	i
Abstract	ii
Acknowledgement	iii
Contents	iv
List of Figures	vi
Chapter 1. Introduction	1
1.1 High-order transverse modes	1
1.2 VCSEL – vertical cavity surface emitting laser	3
1.3 Jet formation – Laser-induced water jet	10
Reference	13
Chapter 2. High-order lasing mode and free space propagation of large-aperture VCSELs	18
2.1 Large-aperture square VCSEL	18
2.1.1 Theoretical analysis	18
2.1.2 Experimental setup	24
2.1.3 Results and discussion	26
2.2 Large-aperture equilateral-triangular VCSEL	33
2.2.1 Theoretical analysis	33
2.2.2 Experimental setup	38
2.2.3 Results and discussion	39
Reference	52
Chapter 3. Laser-induced breakdown beneath a flat water surface – Vertical focusing	54
3.1 Experimental setup	54
3.2 Results and discussion	59
3.2.1 Thin jet, thick jet, and crown formation	59
3.2.2 Temporal evolution of laser-induced water jet	73

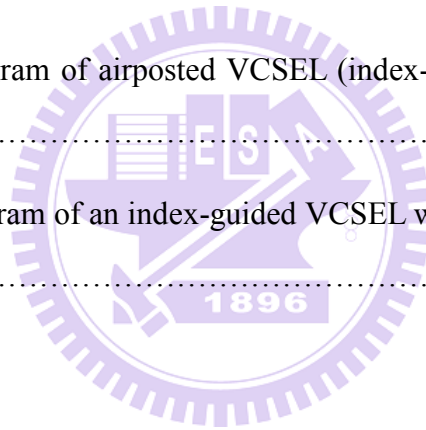
Reference.....	80
Chapter 4. Laser-induced breakdown beneath a flat water surface – Parallel focusing.....	83
4.1 Laser-induced elongated bubble in infinite surrounding	84
4.2 Experimental setup.....	86
4.3 Results and discussion	88
Reference.....	101
Chapter 5. Summary and Future works	103
Reference.....	106
Appendix A.....	107
Appendix B.....	111
Reference for Appendix	117
Curriculum Vitae.....	119
Publication List.....	120



List of Figures

Chapter 1

- Fig. 1.1** Schematic diagram of a gain-guided VCSEL with ion implantation regions to confine the injection current as the effective active transverse region [13, Fig. 1.9].7
- Fig. 1.2** Schematic diagram of airposted VCSEL (index-guided structure) [14, Fig. 1.].8
- Fig. 1.3** Schematic diagram of an index-guided VCSEL with oxide aperture [17, Fig. 6.].9



Chapter 2

- Fig. 2.1** Eigenfunctions with Eigenvalues $n=1, 2,$ and 3 of 1D infinity potential well. 21
- Fig. 2.2** Low order eigenstates and a slight high-order mode $(30, 30)$. We can expect that properties of classical periodic orbits can not manifest and construct only by the conventional eigenstates even in the correspondence limit of large quantum numbers. 22

Fig. 2.3	Stationary coherent states of $ \Psi_{20,20}^{p,q,\phi}(x,y) $ with different (p,q,ϕ) . The ϕ is set to be 0 to π and the values of (p,q) are $(1,1)$, $(1,2)$, and $(2,2)$	23
Fig. 2.4	The schematic experimental setup for observing the near, far field, and the free space propagation of VCSELs.	24
Fig. 2.5	Schematic of the large-aperture square VCSELs device structure.	25
Fig. 2.6	(a) The Bouncing-ball lasing mode at temperature 275K; (b) superscar lasing mode $(1,1)$ at temperature 260K. The far-field patterns (a'), and (b') correspond to (a), and (b), respectively.	28
Fig. 2.7	(a) The theoretical Bouncing-ball mode; (b) superscar mode $(1,1)$. The far-field patterns (a'), and (b') correspond to (a), and (b), respectively.	29
Fig. 2.8	The free-space propagation of a bouncing-ball near field. The experimental results are shown in first and third rows and the theoretical results are shown in the second and forth rows.	31
Fig. 2.9	The free-space propagation of a diamond-like superscar near field.	32
Fig. 2.10	(a) Some eigenstates of equilateral-triangular 2D infinity potential well $ \Phi_{m,n}^{(C)}(x,y) $. (b) Some eigenstates of equilateral-triangular 2D infinity potential well $ \Phi_{m,n}^{(S)}(x,y) $. When $m=2n$, $\Phi_{m,n}^{(S)}(x,y) = 0$	35, 36
Fig. 2.11	Stationary coherent states of $ \Psi_{42,20}^+(x,y;1,0,\phi) $ with different ϕ	37
Fig. 2.12	Schematic of the large-aperture equilateral-triangular laser device structure.	38
Fig. 2.13	Experimental near-field morphologies: (a) honeycomb eigenmode, (b) cane-like superscar $(1,0)$ mode, (c) superscar $(1,1)$ mode. The far-field patterns (a'), (b'), and (c') correspond to (a), (b), and (c), respectively.	43

Fig. 2.14 Theoretical near-field morphologies: (a) honeycomb eigenmode, (b) cane-like superscar (1,0) mode, (c) superscar (1,1) mode. The far-field patterns (a'), (b'), and (c') correspond to (a), (b), and (c), respectively. 44

Fig. 2.15 The experimental and Theoretical far-field patterns from honeycomb pattern (above) and superscar (1,1) mode (bottom) in near field. The morphology of the numerical patterns is enhanced. 45

Fig. 2.16 Six points on one of the triangular of Magen David is connected with only one touch. 46

Fig. 2.17 Experimental and theoretical results of free-space propagation of the honeycomb eigenmode. The experimental results are shown in first and third rows and the theoretical results are shown in the second and forth rows. 48

Fig. 2.18 Experimental and theoretical results of free-space propagation of the cane-like superscar (1,0) mode. The experimental results are shown in first and third rows and the theoretical results are shown in the second and forth rows. 49

Fig. 2.19 Experimental and theoretical results of free-space propagation of the superscar (1,1) mode. The experimental results are shown in first and third rows and the theoretical results are shown in the second and forth rows. .. 50

Fig. 2.20 The formation about six points in the diffraction pattern of the experimental results. 51

Chapter 3

- Fig. 3.1** (a) The Experimental setup. (b) The high speed camera of GX-3 which is setup at the right down corner of Fig. 3.1(a). **56**
- Fig. 3.2** The initial bubble shape with different laser energy. The frame rate is 10,000 fps and the time of each frame is labeled on the top. **57**
- Fig. 3.3** The maximum bubble diameter with different laser energy. The solid line is a guide for the eye. **58**
- Fig. 3.4** A complete water jet is generated on a flat free surface with $\gamma = 0.8$. The frame rate is 80,000 fps. In the pictures of surface sinking, the exposure time is set to $1\mu\text{s}$ **60**
- Fig. 3.5** The numerical simulation and curvature schematic of the surface depression are shown. The z and r of cylindrical coordinate are normalized to the R_{max} of the bubble. **62**
- Fig. 3.6** A surface schematic of the circular ring-shaped crater is shown, which is generated around the thin jet during the surface depression induced by the downward collapse bubble. **63**
- Fig. 3.7** The frame rate is 80,000 fps as same as Fig. 3.4. Figures 3.7(a) and (c) illustrate the non-crown formation when γ -value is smaller than 0.5 and larger than 1.1, respectively. Figure 3.7(b) shows another structure of the crown formation as compared to Fig. 3.4. This crown is denoted as unstable crown formation. **65-67**
- Fig. 3.8** (a) The Schlieren photograph about the interaction between the shock wave emitted from the bubble and the free surface [13, Fig. 5]. (b) A zero pressure region is formed between the bubble and the bottom of the thin jet [3, Fig. 4(g)]. **69**

Fig. 3.9 The structures of the thin jets and crowns with different γ -values which are labeled on the left top of each image. The frame rate is 30,000 fps but the time interval between each frame is 0.166 ms. The arrow shows the orientation of the crown wall, which rotates counterclockwise to vertical direction when γ is increased from 0.5 to 1.02. 71

Fig. 3.10 A typical result for the experimental result for the morphological variations in the temporal evolution of the water jet generated by laser-induced breakdown at a depth of $\gamma = 0.9$. The time (in μs) is indicated at the bottom of each frame. 75

Fig. 3.11 A typical result for the morphological variations in the temporal evolution of the water jet generated at a depth of $\gamma = 0.7$ 77

Fig. 3.12 A typical result for the morphological variations in the temporal evolution of the water jet generated at a depth of $\gamma = 1.04$. The time (in μs) is indicated at the bottom of each frame. 78

Fig. 3.13 Dependence of the pinched altitude H of the crown-shaped water jet on the depth parameter γ in the range of 0.6-1.1. The time (in μs) is indicated at the bottom of each frame. 79

Chapter 4

Fig. 4.1 The oscillation of an elongated bubble in infinite surrounding. The frame rate is 100,000 and the exposure time is $1\mu\text{s}$ 85

Fig. 4.2 The schematic experimental setup for observing the water jet on the free surface. Laser is horizontally focused into the water. 87

Fig. 4.3 The water jet for $\gamma = 1.18$. The major axis of the bubble is parallel to the water surface. The frame rate is 30,000 and the exposure time is $10\mu\text{s}$ **90**

Fig. 4.4 The water jet for $\gamma = 0.76$. The time (in μs) is indicated at the bottom of each frame. The top of the thick jet shows an asymmetry crown-shape water jet. **91**

Fig. 4.5 (a) The water jet for $\gamma = 0.73$. The exposure time is $10\mu\text{s}$ and the time (in μs) is indicated at the bottom of each frame. The thin jet analogously rotates like drill. (b) The zoom-in pictures around the surface depression. The frame rate is 50,000 and the shutter speed is $3\mu\text{s}$. The time (in μs) is indicated at the bottom of each frame. **95**

Fig. 4.6 The breakup of a water jet induced by vertically focusing the laser beam beneath the free water surface. The waving on the water jet is cylindrical symmetry and the water jet gradually breaks up into several drops. Additionally, the breakup of the thin part of the water jet has similar result. **96**

Fig. 4.7 (a) The vibrations on the thin jet with directions on major and minor axes are unmatched to each other. (b) The schematic of the circular polarized of an electromagnetic wave. **97**

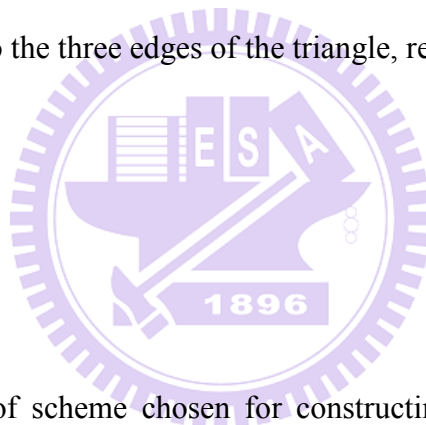
Fig. 4.8 The water jet for $\gamma = 0.63$. The exposure time is $10\mu\text{s}$ and the time (in μs) is indicated at the bottom of each frame. The thin jet is pulled outward by the two arms and forms a sheet structure. **98**

Fig. 4.9 A sheet thin jet with shape in non-isosceles triangle is generated when the laser is focused with focus length in 120mm. As we can see in the first frame, the shape of the elongated bubble is twist due to the energy distribution around the focus volume induced by increasing the focus length. **99**

Fig. 4.10 The water jet for $\gamma = 0.55$. The exposure time is $10\mu\text{s}$ and the time (in μs) is indicated at the bottom of each frame. The thick jet shows a sheet structure and gradually shrinks back to a cylinder-like structure.100

Chapter 5

Fig. 5.1 A laser-induced water jet is generated by vertically focusing the laser beam beneath a free surface with a lateral equilateral triangular boundary inserted below the free surface. There are three arms forms on the crown, which are perpendicular to the three edges of the triangle, respectively.105



Appendix

Fig. B.1 The geometry of scheme chosen for constructing the model of pulsation bubble beneath a free surface. The normal vector points out from the fluid domain. The azimuth angle is θ116

Chapter 1. Introduction

The effects of boundaries are popular in sciences, technology applications, and even in our daily life. In quantum mechanics, the potential wells of boundaries quantize the energy states and determine the wave function. The general types of potential well are infinity potential and quantum harmonic oscillator. The wave function of these potential well are the types of the few quantum-mechanical systems for which an exact, analytical solution is known. In classical mechanics, boundary is important for studying the properties of system. For example, a thermodynamic system is defined by boundaries or walls of specific natures, together with the physical surroundings of that region, which determine the processes allowed to affect the interior of the region.

In this work, we studied the boundary effects on transverse modes in optics and the laser-induced water jet in fluid mechanics, and firstly, in this chapter, we briefly review the previous works in these fields.

1.1 High-order transverse modes

Resonant cavity is essential to laser or other optical devices and determines the special feature of the emitted light, e.g. power, beam directionality, quality factor, output spectrum. In microdisk laser, for achieving low threshold, the shape of cavity can be designed in circular disk or cylinder to achieve the high-Q modes due to the well-known whispering-gallery mode in a circular-shaped planar cavity [1-3]. In addition to the threshold, integration of microdisk laser into an optoelectronic system

will require coupling the light from microdisk laser to outer system like fiber or another microdisk. The well control directional emission is necessary for high-Q microdisk applications.

The general method to implement a directional emission is the shape deformation. Asymmetric resonant cavities slightly deformed from perfect symmetry cavities (e.g. circular or spherical cavities) lead to partially chaotic ray dynamic. The ray in such deformed cavity can not be completely confined by the total internal reflection of the boundary, and finally leaks at an artificial gap on the cavity to achieve the desired directional emission. Recently, the research on shape deforming, e.g., a deformed circular cavity by J. U. Nockel & A. Douglas Stone [4,5], G. D. Chern 2003 [6], and J. Lee 2008 [7]; a deformed square cavity by Tao Ling [8]; corner-cut square cavity by Chung Yan Fong [9]. In addition to the method of deformation, stadium shape is another way to implement the directional emission, which is classified to irregular billiard and studied in the fields of classical and quantum chaos [10]. The stadium resonator consists of two half-circles connected by two straight side walls. In classical billiard model in which classical particle moves freely and bounces elastically with no energy loss, there are two types of orbits: stable periodic orbit (PO) and unstable PO. Stable POs form a close loop and always exist in a regular billiard because of their high symmetry. On the other hand, unstable POs are determined according to that the PO is diverged and can not form a close loop when the trajectories of the PO have slightly dislocation or shift. For example, in a stadium resonator, the diamond periodic orbit is an unstable PO and the bouncing ball between the straight side walls is a stable PO. In a quantum model, interference patterns of wave functions localized around the unstable periodic orbits are called "scars" named by Heller [11]. In addition to scars, wave functions localize on the perturbation stable

periodic orbits are so-called “superscars”, which was originally used by Heller [11] to make a difference with scar.

The main drawback in the studies of microcavity or microdisc laser is that the transverse mode can not be directly measured. Generally, the transverse modes of a microdisc laser are theoretically constructed from the directional emission of output in experiment. In this article, vertical cavity surface emitting lasers named VCSELs are used to study the high-order transverse modes in certain shapes of boundaries. As shown in next section, VCSELs can be analogously investigated the transverse modes in a microcavity and the output emitted light from VCSEL bears the potential to allow for directly measuring the transverse modes and directional emissions.

1.2 VCSEL – vertical cavity surface emitting laser

Vertical-cavity surface-emitting lasers (VCSELs) are made by sandwiching a light emitting layer between two highly reflective mirrors. The light emitting layer is generally composed in multi-quantum layer for high gain efficiency and the high reflective mirror can be dielectric multilayered or distributed Bragg reflectors (DBRs).

The transverse confinement of optical field and electrical current is important for designing VCSELs. Generally, there are three types to confine the transverse optical field: gain guiding, index guiding, or antiguiding mechanisms. In Fig. 1.1, gain guiding is generally achieved by ion implantation into the DBR to control the flow of the injection current into the active layer [12,13]. However the configuration of ion-implanted region can not well define the diffusion of carrier concentration along the transverse direction of the active layer. Additionally, it is hard to apply the ion implantation to the active region for well defining the current distribution because it

will increase the optical absorption loss of the VCSEL. Thus, at high power operation, the VCSEL with ion implantation can be excited high-order transverse modes due to the thermal lensing because of the non-well defined transverse confinement of the active layer. The other problem is the electrical resistivity of the DBR, which may increase the heat generation inside the laser cavity. The only benefit of this structure is planer configuration, which improves the simplification in fabrication process so the low production cost could achieve.

Compared to the gain-guided VCSELs, index-guided VCSELs have better transverse confinement of optical field. The index-guided VCSELs are implemented by inserting a material which has a low refractive index then the semiconductor of active layer to confine the optical field of transverse mode. This structure is similar to the waveguide of a fiber. Several types of index-guided VCSELs are implemented such as airposted, etched mesa and oxide aperture. These types have different mechanisms to confine the optical field and injection current as well as different production costs in fabrication process. The airposted VCSELs [14] as shown in Figure 1.2, the edge of active layer is direct contact with the outside air. The large difference in refractive index between the semiconductor material and the air provide very robust transverse confinement on optical field. But the roughness of the sidewall and the aperture-like structure from the active layer to the downside DBR increase the scattering and diffraction loss respectively. According to the research of waveguide, the larger the difference of refractive index between the materials of core and cladding layer the stronger confinement of optical field in the core, but conversely, the mode number will increase. Thus the single-mode operation is not stable in airposted VCSELs, especially at high injection current. Another type of index-guide VCSELs called oxide aperture VCSEL (Fig. 1.3) are now the most popular and promising devices for several applications such as short range communication, optical disk

readout head, laser printing, and sensor application [15-17]. For the confinement of optical field, effective refractive index between the oxide aperture and the surrounding semiconductor material can be controlled through the thickness of the oxide aperture and the location relative to the active layer. Additionally, the insulation of silicon oxide of oxide aperture forces the injection current through the aperture, which enhance the wall-plug efficiency [18]. As a result, the oxide aperture VCSELs have advantages on the well define of transverse lasing modes, extremely low threshold current [19], and low cost and high yield production of the oxidation procedure.

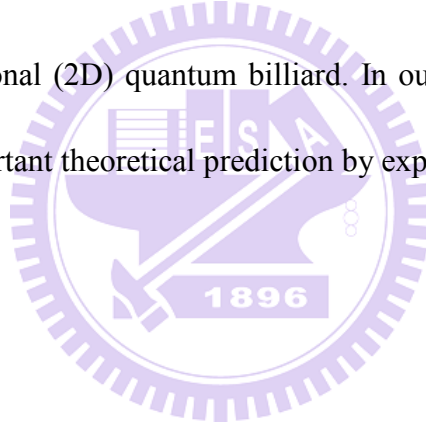
For analogously studying the direction emission from a transverse mode of a microcavity by VCSEL, we have to confirm the relation between the transverse mode of a microcavity and the transverse optical field of VCSELs. The electric field of optical beams obeys the wave equation $(\nabla^2 - \mu_0 \varepsilon \partial^2 / \partial t^2) \vec{E}(x, y, z : t) = 0$. According to the waveguide theory, the electric fields with a predominantly z direction of propagation can be approximated as $\vec{E}(x, y, z : t) = \vec{E}(x, y) e^{i(k_z z - \omega t)}$, where k_z is the wave vector along z-direction and ω is the angular frequency [20]. Although VCSELs have highly symmetric structure, the existence of anisotropy can break the degeneracy of transverse modes in two orthogonal polarizations, resulting in a split in oscillation frequency. Therefore, total electric field includes the two polarized states can be expressed as

$$\vec{E}(x, y, z : t) = E_x(x, y) e^{i(k_{z,x} z - \omega_x t)} \hat{a}_x + E_y(x, y) e^{i(k_{z,y} z - \omega_y t)} \hat{a}_y, \quad (1.1)$$

where $k_{z,x}$ and $k_{z,y}$ are the wave vector along z-direction, and the ω_i is the angular frequency in i -polarized state. After separating the z component in the wave equation, we are left with a two-dimensional Helmholtz equation in the two polarized states

$$\begin{cases} \left[\nabla_i^2 + (\mu_0 \varepsilon \omega_x^2 - k_{z,x}^2) \right] E_x(x, y) = 0 \\ \left[\nabla_i^2 + (\mu_0 \varepsilon \omega_y^2 - k_{z,y}^2) \right] E_y(x, y) = 0 \end{cases} \quad (1.2)$$

where ∇_i^2 means the Laplacian operator operating on the transverse x and y coordinates. Since the electric field in VCSELs experience total reflection on the lateral walls, transverse optical field at the boundary of cavity can be approximated as $E_i(x, y)|_{x,y \in \partial \Omega} = 0$ with $i = x$ or y . Obviously, transverse electric fields of VCSELs are thoroughly equivalent to eigenfunctions of 2D Schrödinger equation with infinity potential well of the same geometry. In other words, the transverse optical fields $E_i(x, y)$ of VCSELs can be used to analogously investigate the wave functions $\psi(x, y)$ in two-dimensional (2D) quantum billiard. In our previous works [21], we have confirmed this important theoretical prediction by experiment.



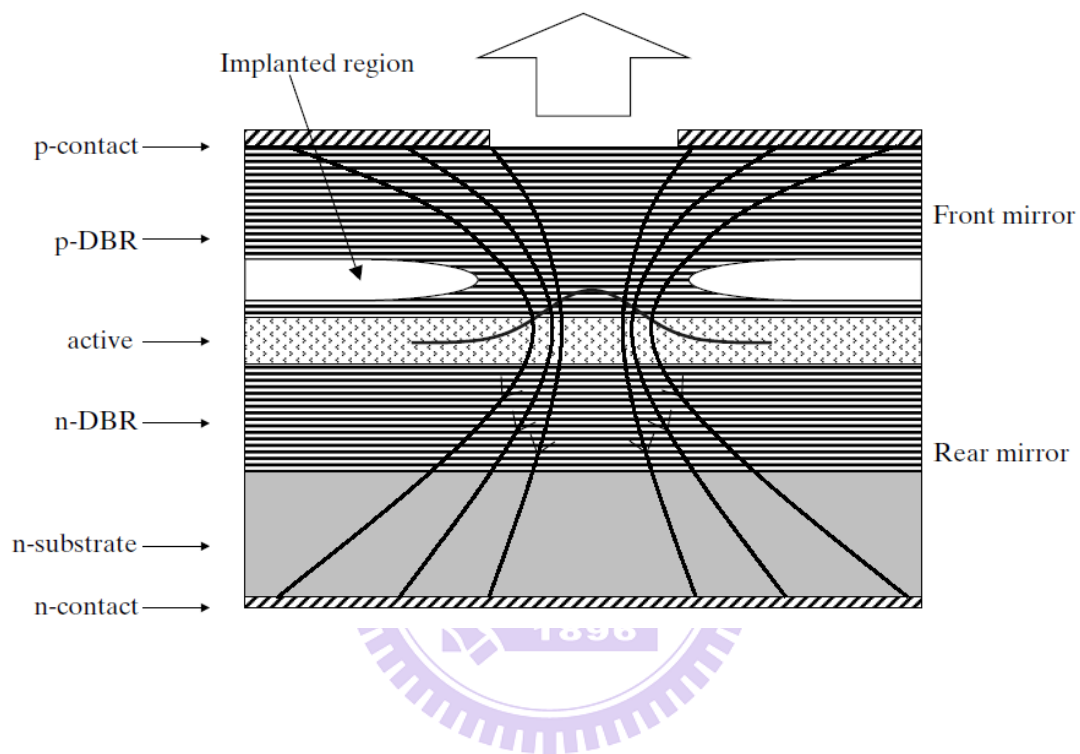


Fig. 1.1 Schematic diagram of a gain-guided VCSEL with ion implantation regions to confine the injection current as the effective active transverse region [13, Fig. 1.9].

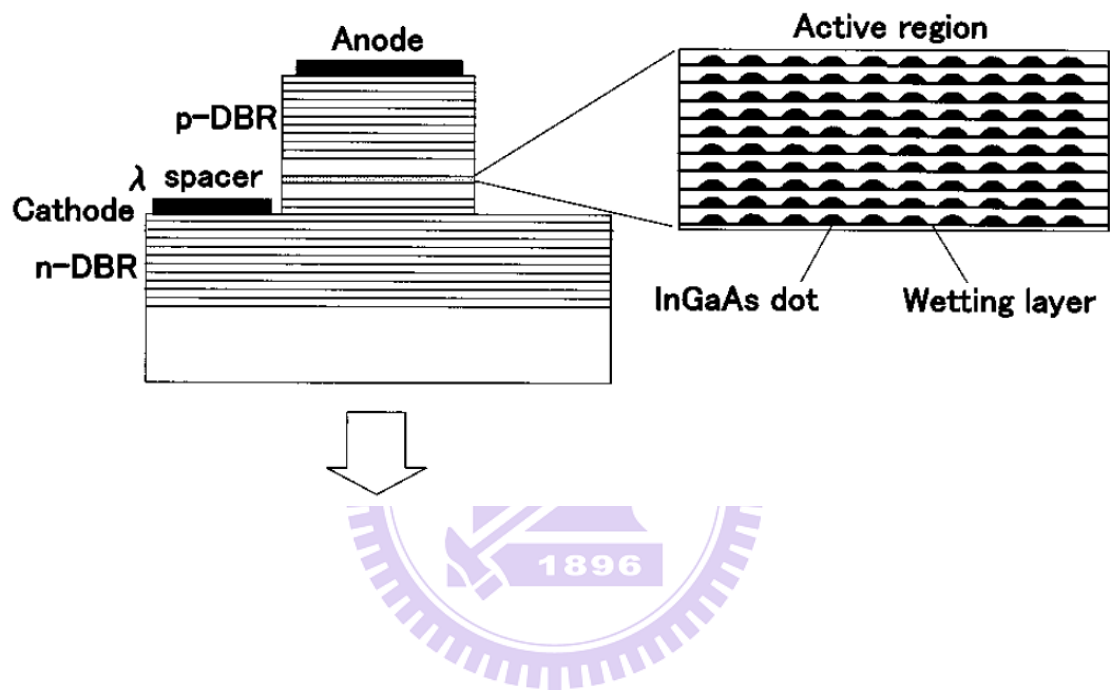


Fig. 1.2 Schematic diagram of airposted VCSEL (index-guided structure) [14, Fig. 1.].

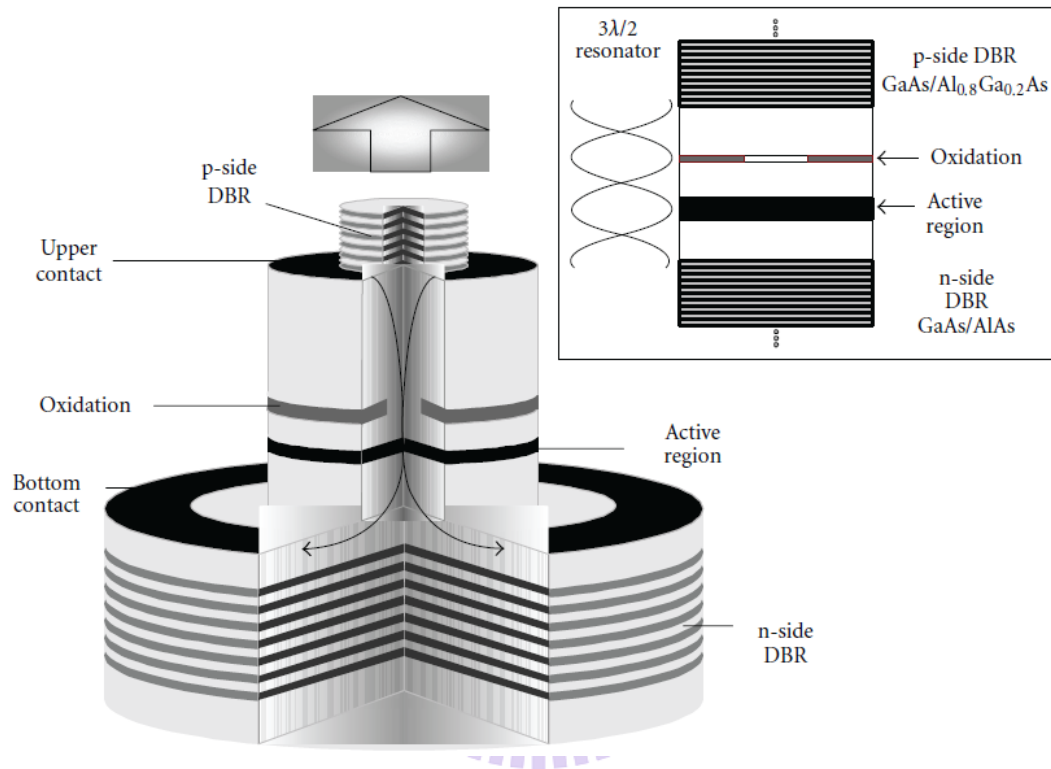


Fig. 1.3 Schematic diagram of an index-guided VCSEL with oxide aperture [17, Fig. 6.].

1.3 Jet formation – Laser-induced water jet

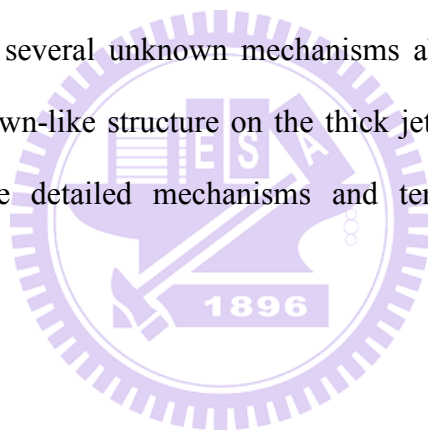
In the next part of this work, we investigate the liquid jet formation. These studies are widely encountered in nature and various applications such as ink-jet printing, spray cooling, quenching and cutting of metal, liquid jet based needle-free injectors, DNA sampling, nuclear fission, powder technology [22-25]. On the other hand, jet dynamic investigates several physical properties of fluid, such as surface tension, viscosity, and non-Newtonian rheology. Almost all classical physics comes into play in the dynamic of jet, and still remains several challenging cases. In this article, we focus on the laser-induced liquid jet on a free surface. Free surface flows are almost the most beautiful and complicate phenomena encountered in fluid mechanics. This is especially true when a liquid surface is disturbed by a violent event beneath the free surface in the fluid domain or from the outside world to the fluid domain like an object impact or a reflecting shock wave.

When an object travels through a free surface of a fluid, a familiar jet formation exists, which is called Worthington jet [26] after the pioneering work on time-resolved imaging of A.M. Worthington. The object impacting on the free surface causes a crater on the free surface, and the collapse of this crater generates a vertical upward jet. Eruption of liquid jets from collapsing depressions has indeed been observed in a number of diverse instances, such as forcing the standing Faraday waves in a liquid surface [27], during the burst of bubbles [28], and tubular jet [29]. The tubular jet is formed in a tube when the tube is initially immersed in a tank of fluid and then suddenly released [29]. In addition to the fluid, a bed of fine, loose sand which nearly has no surface tension can also generate a remarkably different jet dynamics called granular jet when a particle falls and impacts into the sand [30].

Compared to the jet formed from a crater, a jet or splash forms on a free surface when an object is expanding very fast beneath a water surface such as material explosion which was studied extensively since World War II in the field of underwater explosions [31]. These studies, dealing with a large-size explosion bubble in underwater explosion, mainly focused on the bubble oscillation and the generation of spray on the free surface [31,32]. Recently, a small-scale cavitation bubble in millimeter size was used and the results showed more qualitative behaviors compared to the large-size explosion bubble for further theoretical simulations [33]. Understanding these behaviors is believed to shed light on the mechanisms of the erosion damages on a deformable surface caused by a nearby collapsing bubble [34,35]. Such a small-scale bubble was generally generated by using spark discharge [36] and these studies showed that, universally, an oscillating bubble develops into a toroidal shape during its collapse [33-35]. This shape evolution was reconstructed well in theoretical simulations [33-35]. In addition to the bubble, a liquid jet was seen to burst out from the free surface, and for a certain bubble depth, there emerged a thin jet followed by a markedly thicker jet and a circular crown-like jet perfectly connected on the shoulder of the thick jet transited to the thin jet [34,37].

The main drawbacks of the spark discharge and material explosive are the unavoidable influence of the electrodes and remained explosives on the dynamics of the bubble and liquid jet. In contrast, lasers have been shown to be useful and precisely controllable for generating a bubble by direct optical breakdown with pulsed lasers [38,39] or thermocavitation with CW lasers [40]. Several dynamics with different boundary systems were observed such as rigid wall for applications of erosion damages and fluid pumping [38,41,42], membrane or living cell for tissue engineering applications [43,44]. The oscillation times of a cavitation bubble near a rigid wall and free surface were investigated and compared with modified Rayleigh's

model [45]. Very recently, a liquid jet on a flat free surface induced by a femtosecond pulsed laser was implemented in a new laser printing technique named film-free laser induced forward transfer (LIFT) to overcome the constraint of solid or liquid film preparation [46]. Furthermore, the laser-induced breakdown bears the potential to generate a more complex and flexible jet formation by controlling the shape of the bubble. K. Y. Lim *et al.* in 2010 [47] showed that complex bubble patterns can be generated using a holographic element in which the laser energy distribution is controlled by the patterns displayed on a spatial light modulator (SLM) acting as a phase object by a Fourier transform. As a result, bubble shaping and multiple bubble are achievable for inducing desired liquid jet. However, despite the great potential in future, there still remain several unknown mechanisms about the liquid jet and its evolution such as the crown-like structure on the thick jet [37]. The purpose in this article is to explore the detailed mechanisms and temporal evolutions of the laser-induced liquid jet.



Reference

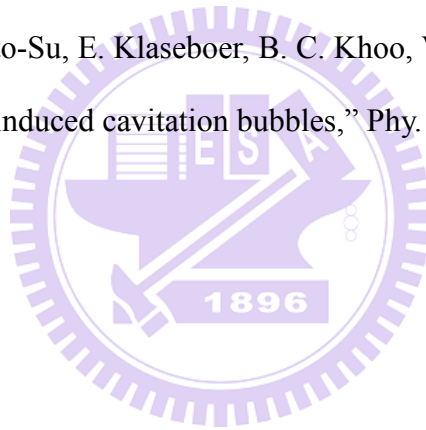
- [1] S. L. McCall, A. F. J. Levi, R. E. Slusher, S. J. Pearton, and R. A. Logan, “Whispering-gallery mode microdisk lasers,” *Appl. Phys. Lett.* **60**, 289-291 (1992).
- [2] Kerry Vahala, *Optical Microcavities* (World Scientific Publishing Co. Pte. Ltd. 2004).
- [3] D. K. Armani, T. J. Kippenberg, S. M. Spillane, and K. J. Vahala, “Ultra-high-Q toroid microcavity on a chip,” *Nature*, **421**, 925-928 (2003).
- [4] J. U. Nockel, A. D. Stone, and R. K. Chang, “Q spoiling and directionality in deformed ring cavities,” *Opt. Letts.* **19**(21), 1693-1695 (1994).
- [5] J. U. Nockel and A. D. Stone, “Ray and wave chaos in asymmetric resonant optical cavities,” *Nature*, **385**, 45-47 (1997).
- [6] G. D. Chern, H. E. Tureci, A. D. Stone, R. K. Chang, M. Kneissl, and N. M. Johnson, “Unidirectional lasing from InGaN multiple-quantum-well spiral-shaped micropillars,” *Appl. Phys. Lett.* **83**(9), 1710-1712 (2003).
- [7] J. Lee, S. Rim, J. Cho, and C. M. Kim, “Resonances near the Classical Separatrix of a Weakly Deformed Circular Microcavity,” *Phys. Rev. Lett.* **101**, 064101 (2008).
- [8] T. Ling, L. Liu, Q. Song, L. Xu, and W. Wang, “Intense directional lasing from a deformed square-shaped organic–inorganic hybrid glass microring cavity,” *Opt. Letts.* **28**(19) 1784-1786 (2003).
- [9] C. Y. Fong and A. W. Poon, “Planar corner-cut square microcavities: ray optics and FDTD analysis,” *Opt. Express*, **12**, 4864-4874 (2004).
- [10] M. C. Gutzwiller, *Chaos in Classical and Quantum Mechanics* (Springer-Verlag, New York, 1990).

- [11] E. J. Heller, “Bound-State Eigenfunctions of Classically Chaotic Hamiltonian Systems: Scars of Periodic Orbits,” *Phys. Rev. Lett.* **53**, 1515-1518 (1984).
- [12] Y. J. Yang, T. G. Dziura, T. Bardin, S. C. Wang, and Fernandez, “Continuous wave single transverse mode vertical cavity surface emitting lasers fabricated by Helium implantation and zinc diffusion,” *Electron. Lett.* **28**(3), 274-275, (1992).
- [13] S. F. Yu, *Analysis and Design of Vertical Cavity Surface Emitting Lasers* (Wiley Series in Lasers and Applications, 2003).
- [14] H. Saito, K. Nishi, I. Ogura, S. Sugou, and Y. Sugimoto, “Room temperature lasing operation of a quantum dot vertical cavity surface emitting lasers,” *Appl. Phys. Lett.* **69**(21) 3140–3142 (1996).
- [15] T. H. Oh, D. L. Huffaker, and D. G. Deppe, “Comparison of vertical cavity surface emitting lasers with half-wave cavity confined by single- or double oxide apertures,” *IEEE Photon. Technol. Lett.* **9**(7) 875–877, (1997).
- [16] S. A. Blokhin, J. A. Lott, A. Mutig, G. Fiol, N. N. Ledentsov, M. V. Maximov, A. M. Nadtochiy, V. A. Shchukin, and D. Bimberg “Oxide-confined 850 nm VCSELs operating at bit rates up to 40 Gbit/s,” *Electron. Lett.* **45**(10), 501-503 (2009).
- [17] R. Sarzała, T. Czyszanowski, M. Wasiak, M. Dems, Ł. Piskorski, W. Nakwaski, and K. Panajotov “Numerical Self-Consistent Analysis of VCSELs,” *Adv. Opt. Tech.* **2012**, 689519 (2012).
- [18] P. W. Evans, J. J. Wierer, and N. Holonyak, “Al_xGa_{1-x}As native oxide based distributed Bragg reflectors for vertical cavity surface emitting lasers,” *J. Appl. Phys.* **84**(10), 5436–5440 (1998).
- [19] G. M. Yang, M. MacDougal, and P. D. Dupkus, “Ultralow threshold current vertical cavity surface emitting laser obtained with selective oxidation,” *Electron. Lett.* **31**, 886–888 (1995).

- [20] J. D. Jackson, *classical electrodynamics* (Wiley, New York, 1975), Chap. 8.
- [21] K. F. Huang, Y. F. Chen, and H. C. Lai, and Y. P. Lan, “Observation of the wave function of a quantum billiard from the transverse patterns of vertical cavity surface emitting lasers,” *Phys. Rev. Lett.* **89**, 224102 (2002).
- [22] H. P. Le, “Progress and Trends in Ink-jet Printing Technology,” *J. Imaging Sci. Techn.* **42**(1), 49-62 (1998).
- [23] J. Kim, “Spray cooling heat transfer: the state of the art,” *Int. J. Heat Fluid Fl.* **28**, 753–767 (2007).
- [24] S. Mitragotri, “Current status and future prospects of needle-free liquid jet injectors,” *Nat. Rev. Drug Discov.* **5**, 543-548 (2006).
- [25] L. R. Allain, M. Askari, D. L. Stokes, and T. Vo-Dinh “Microarray sampling-platform fabrication using bubble-jet technology for a biochip system,” *Fresen. J. Anal. Chem.* **371**, 146–150 (2001).
- [26] A. M. Worthington, *A Study of Splashes* (Longmans, Green and Co., London, 1908).
- [27] B. W. Zeff, B. Kleber, J. Fineberg, and D. P. Lathrop, “Singularity dynamics in curvature collapse and jet eruption on a fluid surface,” *Nature* **403**, 401-404 (2000).
- [28] J. M. Boulton-Stone and J. R. Blake, “Gas Bubble bursting at a free surface,” *J. Fluid Mech.* **254**, 437-466 (1993).
- [29] R. Bergmann, E. D. Jong, J. B. Choimet, D. V. D. Meer, and D. Lohse, “The origin of the tubular jet,” *J. Fluid Mech.* **600**, 19-43 (2008).
- [30] S. T. Thoroddsen and A. Q. Shen, “Granular jets,” *Phys. Fluids* **13**, 4-6 (2001).
- [31] R. H. Cole, “*Underwater explosions*” (Princeton, Princeton Univ. Press., 1948).
- [32] J. B. Keller and I. I. Kolodner, “Damping of underwater explosion bubble oscillations,” *J. Appl. Phys.* **27**, 1152-1161 (1956).

- [33] A. Pearson, E. Cox, J. R. Blake, and S. R. Otto, "Bubble interactions near a free surface," *Eng. Anal. Bound. Elem.* **28**, 295–313 (2004).
- [34] G. L. Chahine, "Interaction between an oscillating bubble and a free Surface," *J. Fluids Eng.* **99**, 709-716 (1977).
- [35] P. B. Robinson, J. R. Blake, T. Kodama, A. Shima, and Y. Tomita, "Interaction of cavitation bubbles with a free surface," *J. Appl. Phys.* **89**, 8225-8237 (2001).
- [36] R. H. Mellen, "An experimental study of the collapse of a spherical Cavity in Water," *J. Acoust. Soc. Am.* **28**, 447-454 (1956).
- [37] A. Pain, B. H. T. Goh, E. Klaseboer, S. W. Ohl, and B. C. Khoo, "Jets in quiescent bubbles caused by a nearby oscillating bubble," *J. Appl. Phys.* **111**, 054912 (2012).
- [38] W. Lauterborn and H. Bolle, "Experimental investigations of cavitation-bubble collapse in the neighbourhood of a solid boundary," *J. Fluid Mech.* **72**, 391-339 (1975).
- [39] P. A. Quinto-Su, V. Venugopalan, and C. D. Ohl "Generation of laser-induced cavitation bubbles with a digital hologram," *Opt. Express* **16**(23), 18964-18969 (2008).
- [40] J.C. Ramirez-San-Juan, E. Rodriguez-Aboytes, A. E. Martinez-Canton, O. Baldovino-Pantaleon, A. Robledo-Martinez, N. Korneev, and R. Ramos-Garcia, "Time-resolved analysis of cavitation induced by CW lasers in absorbing liquids," *Opt. Express* **18**(9), 8735-8742 (2010).
- [41] A. Philipp and W. Lauterborn, "Cavitation erosion by single laser-produced bubbles," *J. Fluid Mech.* **361**, 75-116 (1998).
- [42] R. Dijkink and C. D. Ohl, "Laser-induced cavitation based micropump," *Lab Chip* **8**(10), 1676-1681 (2008).

- [43] Y. Tomita and T. Kodama, “Interaction of laser-induced cavitation bubbles with composite surfaces,” *J. Appl. Phys.* **94**, 2809-2816 (2003).
- [44] T. H. Wu, S. Kalim, C. Callahan, M. A. Teitell, and P. Y. Chiou, “Image patterned molecular delivery into live cells using gold particle coated substrates,” *Opt. Express* **18**(2), 938-946 (2010).
- [45] P. Gregorčič, R. Petkovšek, and J. Možina, “Investigation of a cavitation bubble between a rigid boundary and a free surface,” *J. Appl. Phys.* **102**, 094904 (2007).
- [46] M. Duocastella, A. Patrascioiu, J. M. Fernández-Pradas, J. L. Morenza, and P. Serra, “Film-free laser forward printing of transparent and weakly absorbing liquids,” *Opt. Express* **18**(21), 21815-21825 (2010).
- [47] K.Y. Lim, P.A. Quinto-Su, E. Klaseboer, B. C. Khoo, V. Venugopalan, C. D. Ohl, “Nonspherical laser-induced cavitation bubbles,” *Phy. Rev. E* **81**, 016308 (2010).



Chapter 2. High-order lasing mode and free space propagation of large-aperture VCSELs

In this chapter, we study the high-order transverse modes emitted from VCSELs. Square and equilateral triangular shapes of the aperture of VCSELs are studied in chapters 2.1 and 2.2, respectively. In each chapter, firstly, the theoretical model for constructing the near-field transverse mode is studied. Next, the experimental results analyzed with the simulations are discussed.

2.1 Large-aperture square VCSEL

2.1.1 Theoretical analysis

A 1D cavity with rigid wall of boundary can be modeled from the infinity potential well which is the most simple and well known system in every textbook of quantum mechanics [1,2]. The eigenfunction of Schrodinger equation in 1D infinity potential well is solved as a sinusoid wave (Fig. 2.1) in which n is the quantum number.

$$\psi_n(x) = \sqrt{\frac{2}{a}} \sin\left(\frac{n\pi x}{a}\right) \quad (2.1)$$

Because the orthogonal and separable properties between the x and y coordinates, the eigenstates of 2D planer square infinity potential well can be described below

$$\psi_{n_1, n_2}(x, y) = \frac{2}{a} \sin\left(\frac{n_1 \pi x}{a}\right) \sin\left(\frac{n_2 \pi y}{a}\right) \quad (2.2)$$

Figure 2.2 displays some of the eigenstates with their quantum numbers labeled below each figure. The eigenstates of regular square shape are like a chessboard and distribute averagely over the space which don't show any indications of localization on periodic orbits even the quantum number approaches infinity.

According to the correspondence principle, when the quantum number approaches infinity, the probability of wave function will agree with the classical limit. Nevertheless, the wave function doesn't become to a particle in classical limit. The way to connect the wave in quantum and particle in classical, is used the coherent states. The idea of coherent states is the superposition of a set of eigenstates with different eigenvalues and certain phase relations between each eigenstates [3]. As a result, a moving particle can be represented by the superposition of time-variant Schrodinger solution. Extracting the stationary states from the result of superposition of time-variant Schrodinger solution, we can get a wave function associated with periodic orbits.

The stationary coherent states in square shape infinity potential well can be displayed as followed [4]:

$$\begin{aligned} \Psi_{N, M}^{p, q, \phi}(x, y) &= \frac{1}{\sqrt{2^M}} \sum_{K=0}^{M-1} \sqrt{C_K^M} e^{iK\phi} \psi_{qN+pK, pN+q(M-1-K)}(x, y) \\ &= \frac{2}{a\sqrt{2^M}} \sum_{K=0}^{M-1} \sqrt{C_K^M} e^{iK\phi} \sin\left[\frac{(qN+pK)\pi x}{a}\right] \sin\left[\frac{[pN+q(M-1-K)]\pi y}{a}\right] \end{aligned} \quad (2.3)$$

Figure 2.3 displays the stationary coherent states $\Psi_{N,M}^{p,q,\phi}(x,y)$ with different (p,q,ϕ) . Obviously, the two positive integers p and q are related to the number of collisions with horizontal and vertical walls, and the ϕ ($0 \leq \phi \leq 2\pi$) is the wall position of specular reflection points [5].



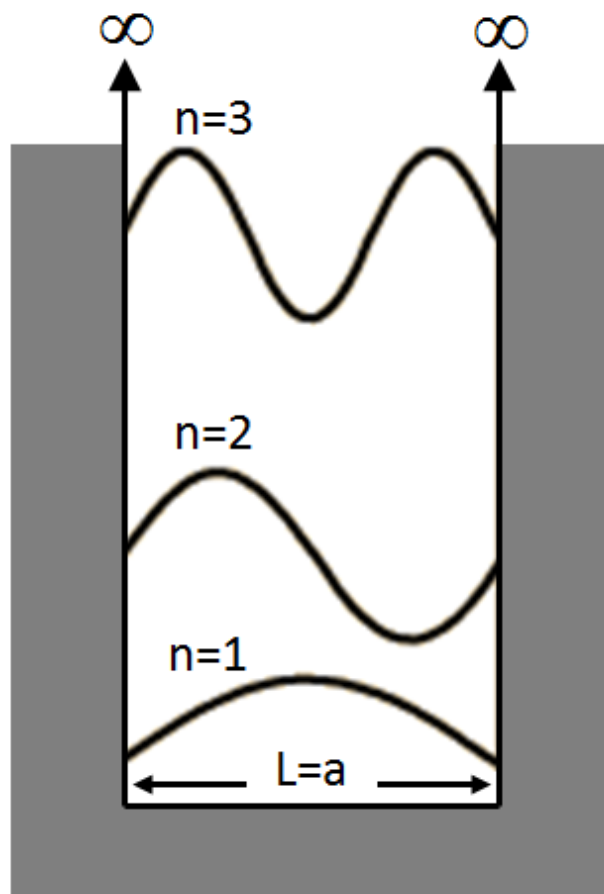


Fig. 2.1 Eigenfunctions with Eigenvalues $n=1, 2,$ and 3 of 1D infinity potential well.

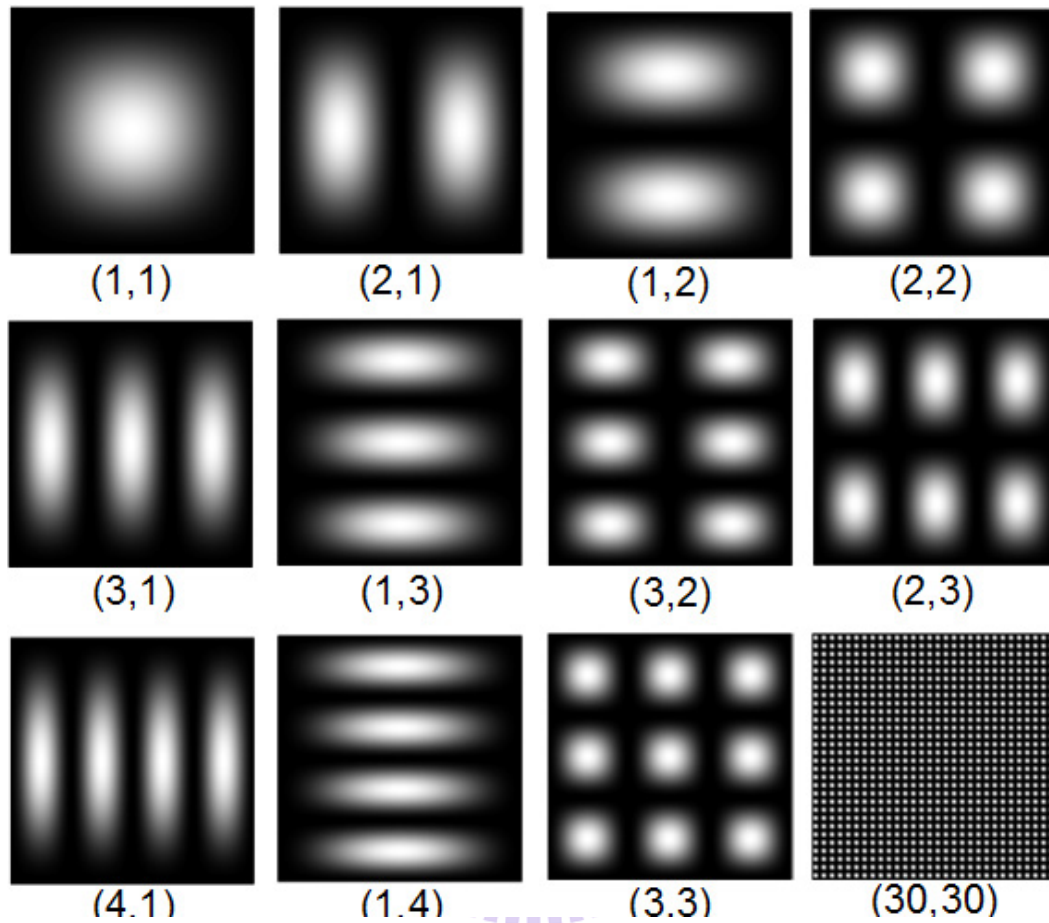


Fig. 2.2 Low order eigenstates and a slight high-order mode (30, 30). The properties of classical periodic orbits can not manifest and construct only by the conventional eigenstates even in the correspondence limit of large quantum numbers.

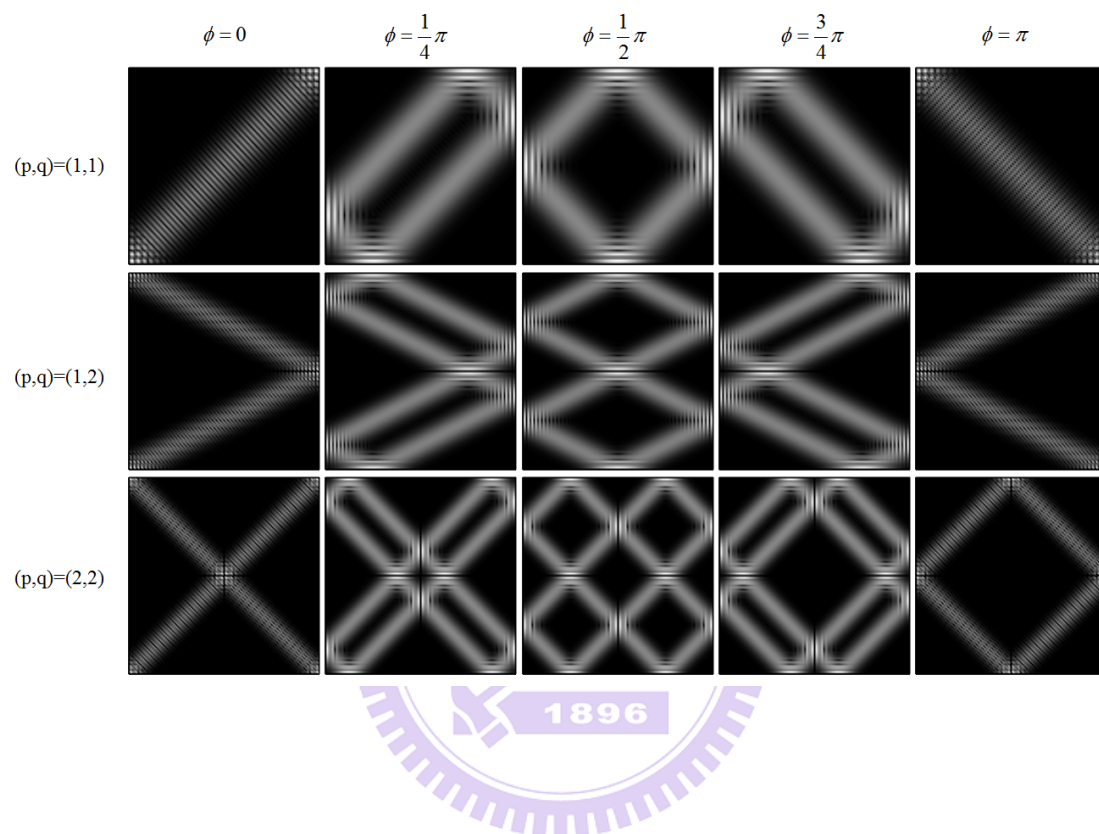


Fig. 2.3 Stationary coherent states of $|\Psi_{20,20}^{p,q,\phi}(x,y)|$ with different (p,q,ϕ) . The ϕ is set to be 0 to π and the values of (p,q) are $(1,1)$, $(1,2)$, and $(2,2)$.

2.1.2 Experimental setup

The experimental setup is shown in Fig. 2.4. The VCSEL device was placed in a cryogenic system with a temperature stability of 0.01 K in the range of 80–300 K. A DC power supplier (KEITHLEY 2400) with a precision of 0.005 mA is used to drive the VCSEL device. The near-field patterns were reimaged into a charge-coupled device (CCD) camera (Coherent, Beam Code) with an objective lens (Mitsutoyo, NA of 0.9). The far-field patterns are measured with a CCD placed behind a screen. The control parameters of the VCSEL in this experiment are the device temperature and pumping currents which are the important factors to affect the lasing transverse modes. The schematic of the laser device structure is shown below in Fig. 2.5. The bright region displays the spontaneous emission to clearly distinguish the area of square boundary and the edge length of the square oxide aperture is approximately 40 μm .

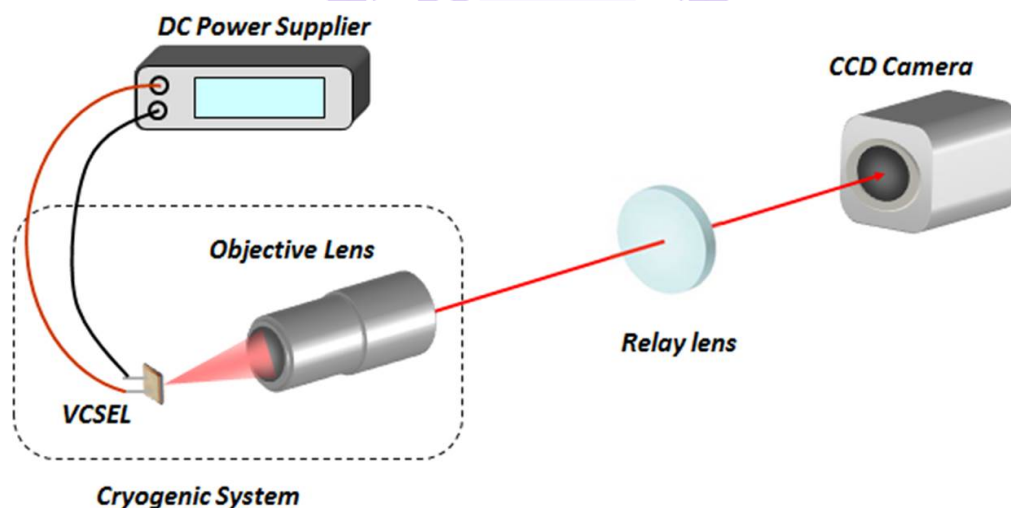


Fig. 2.4 The schematic experimental setup for observing the near, far field, and the free space propagation of VCSELs.

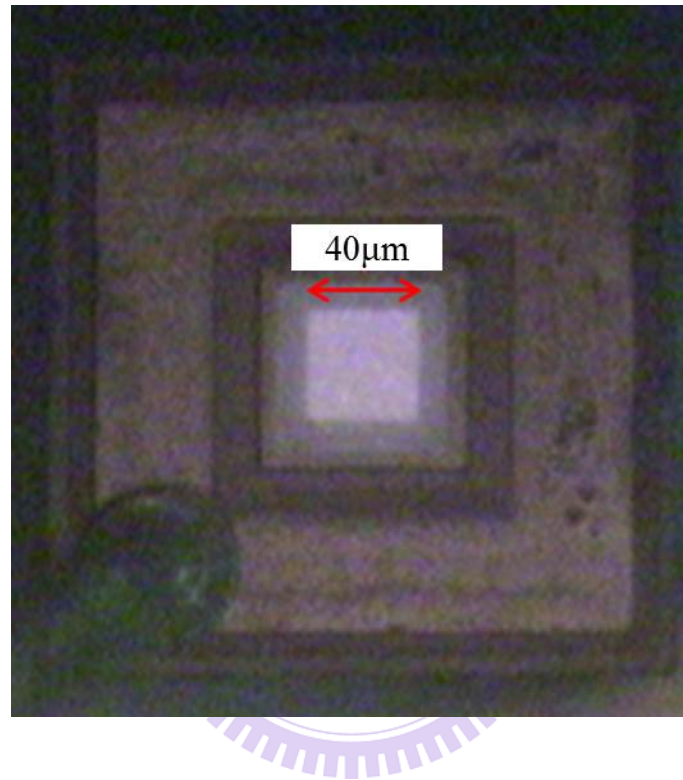


Fig. 2.5 Schematic of the large-aperture square VCSELs device structure.

2.1.3 Results and discussion

At temperature 275K, the lasing mode is shown in Fig. 2.6(a), generally, we call it the bouncing-ball mode. In numerical part, it can be roughly seem an eigenstate of square shape infinity potential well with very high order in horizontal quantum number and slightly deform. The eigenstate $\psi_{n_1, n_2}(x, y)$ of square shape infinity potential well mentioned in section 2.1.1 is shown below,

$$\psi_{n_1, n_2}(x, y) = \frac{2}{a} \sin\left(\frac{n_1 \pi x}{a}\right) \sin\left(\frac{n_2 \pi y}{a}\right) \quad (2.2)$$

According to the work by Chien-Cheng Chen in 2009 [6], the experimental bouncing-ball mode can be reconstructed by a linear combination of two eigenstates:

$$\psi_{40,11}(x, y) \sin(0.35\pi) + \psi_{39,14}(x, y) \sin(0.35\pi) \quad (2.4)$$

The numerical simulation of the bouncing-ball mode is showed in Fig. 2.7(a).

When the operating temperature is decreased to 260K, the near-field of the VCSEL dramatically changes to a diamond-like pattern. About the discussion of numerical research in section 2.1.1, the superscars localized on the perodic orbits can be implemented by the coherent states as shown below [4].

$$\begin{aligned} \Psi_{N,M}^{p,q,\phi}(x, y) &= \frac{1}{\sqrt{2^M}} \sum_{K=0}^{M-1} \sqrt{C_K^M} e^{iK\phi} \psi_{qN+pK, pN+q(M-1-K)}(x, y) \\ &= \frac{2}{a\sqrt{2^M}} \sum_{K=0}^{M-1} \sqrt{C_K^M} e^{iK\phi} \sin\left[\frac{(qN+pK)\pi x}{a}\right] \sin\left[\frac{(pN+q(M-1-K))\pi y}{a}\right] \end{aligned} \quad (2.3)$$

The Equation (2.3) is the form of traveling wave and the standing wave for experimental fitting is expressed as

$$C_{N,M}^{(C)}(x, y; p, q, \phi) = \frac{2}{a\sqrt{2^M}} \sum_{K=0}^{M-1} \sqrt{C_K^M} \cos(K\phi) \sin\left[\frac{(qN + pK)\pi x}{a}\right] \sin\left[\frac{(pN + q(M-1-K))\pi y}{a}\right] \quad (2.5)$$

, and the diamond-like superscar mode shown in Fig. 2.6(b) can be interpreted by

$$C_{36,10}^{(C)}(x, y; 1, 1, 0.57\pi) \quad (\text{Fig. 2.7(b)}). \quad (2.6)$$

As we can see, the near fields of the experiments are reconstructed very well by the model of quantume billiard.

Next, the experimental far fields of the two lasing modes in Figs. 2.6(a) and (b) are observed and shown in Figs. 2.6(a') and (b'), respectively. The two far-field patterns are similar to each other. The far field from the superscar near-field pattern is a square with four points on the corners of the square. Because the far field is related to the momentum distribution of the direction emission of the near field [7,8], we can see that the directions of the four points are parallel to the trajectory of the periodic orbit in near field. Base on the result of the far field of superscar mode, the far field of Fig. 2.6(a') shows that the near field in Fig. 2.6(a) is not completely only a horizontal bouncing-ball mode. These results show that the far field could provide some information for determining the near field. In theoretical part, the far-field pattern is simulated by the method of Fraunhofer diffraction [7], as derived in Appendix A. The results are shown in Figs. 2.7(a') and (b') for the bouncing-ball near-field pattern (eq. (2.4)) and the diamond-like superscar (eq. (2.6)), respectively. There are great agreements between the experimental and numerical results both in the near-field and the far-field patterns.

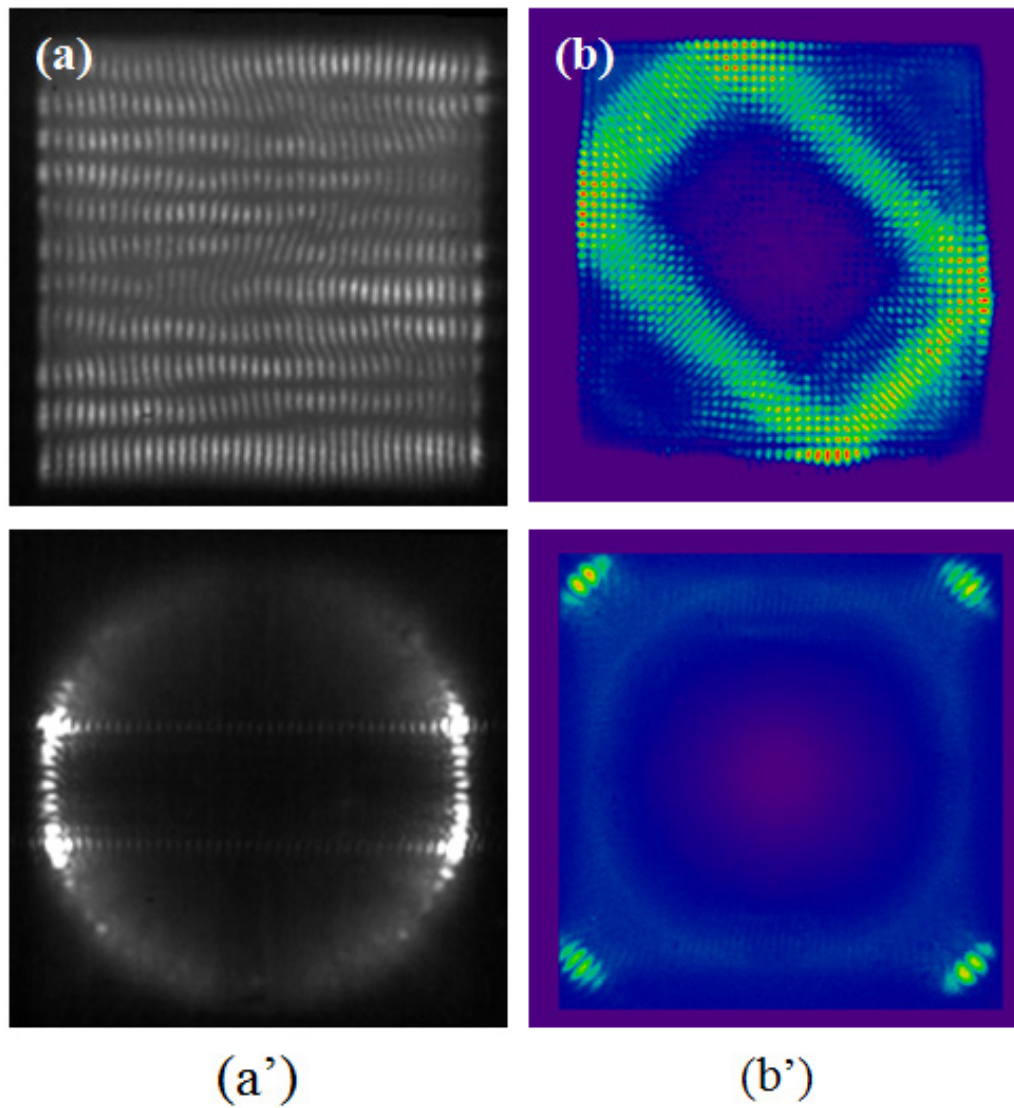


Fig. 2.6 (a) The Bouncing-ball lasing mode at temperature 275K; (b) superscar lasing mode (1,1) at temperature 260K. The far-field patterns (a'), and (b') correspond to (a), and (b), respectively.

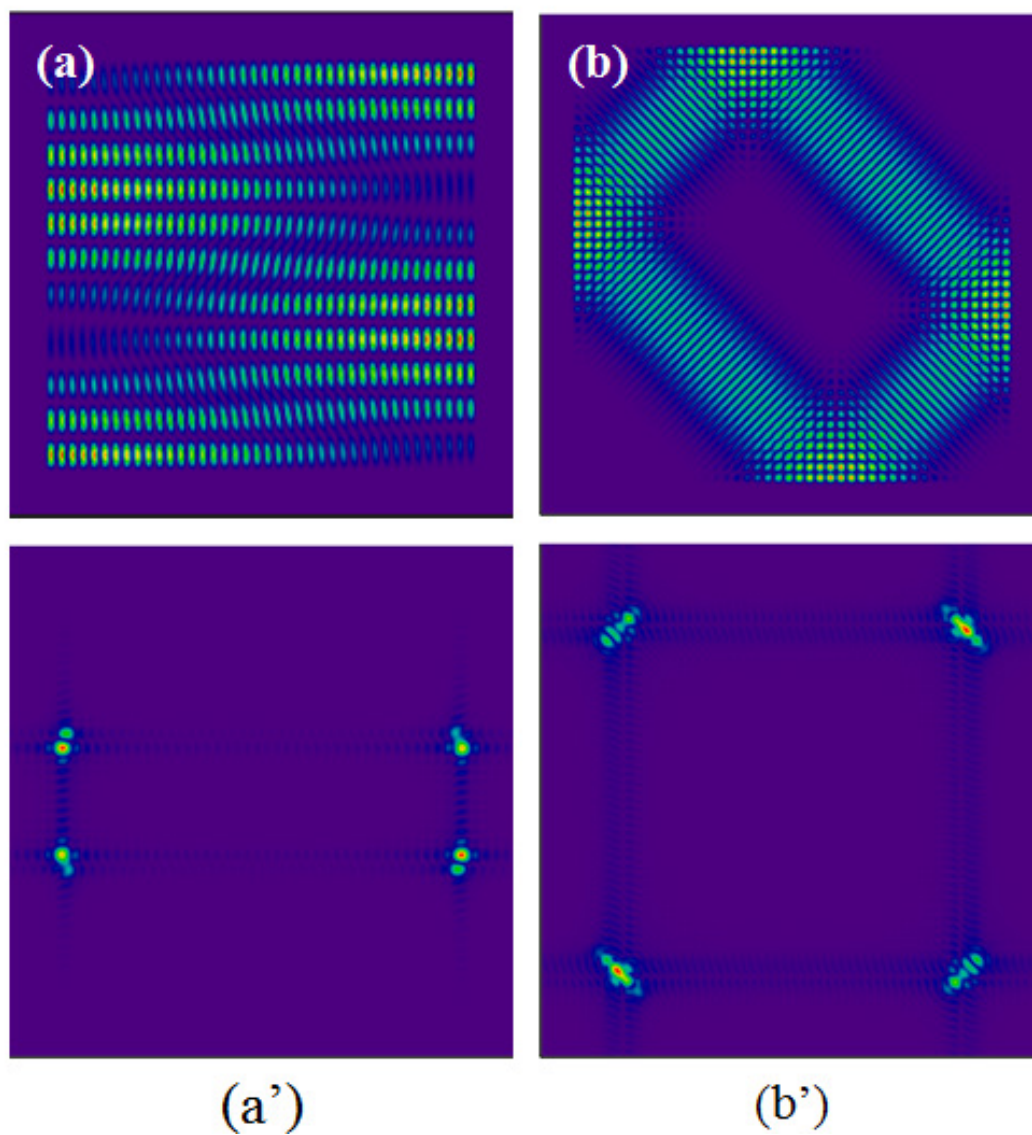


Fig. 2.7 (a) The theoretical Bouncing-ball mode; (b) superscar mode (1,1). The far-field patterns (a'), and (b') correspond to (a), and (b), respectively.

Based on the plenteous morphologies on the near-field and far-field patterns, we further explore the free space propagation from the near field to the far field and use the Fresnel diffraction derived in Appendix A to analyze the experimental results. In Fig. 2.8, the graph in monochrome is the experimental measurement, and the theoretical results are shown under each experimental result. The evolutions of the patterns are horizontal propagation and roughly follow the directions of the interference stripes of near-field patterns. According to the theoretical study, the standing wave is linearly combined by two opposite directional traveling waves. As a result, the interference stripes of near-field pattern will separate to two diffraction patterns in opposite directions as shown in the measurements and the theoretical results.

Compared to the free-space propagation of the bouncing-ball mode, the diamond-like superscar mode shows slight copious morphologies and apparent directions on the propagation of diffraction patterns, as shown in Fig. 2.9. Despite the direction of propagation parallel to the trajectory of the periodic orbit in near field, there are other directions which are not exist in the classical limit. This result is explained by the nature of interference of waves as follows. On the edge of square aperture, the two interference stripes overlap to each other and create another direction of interference pattern. This new interference pattern is parallel to the wall of square and will propagate parallel the boundary of the square, as shown in the sequence pictures (b) to (d) in Fig. 2.9.

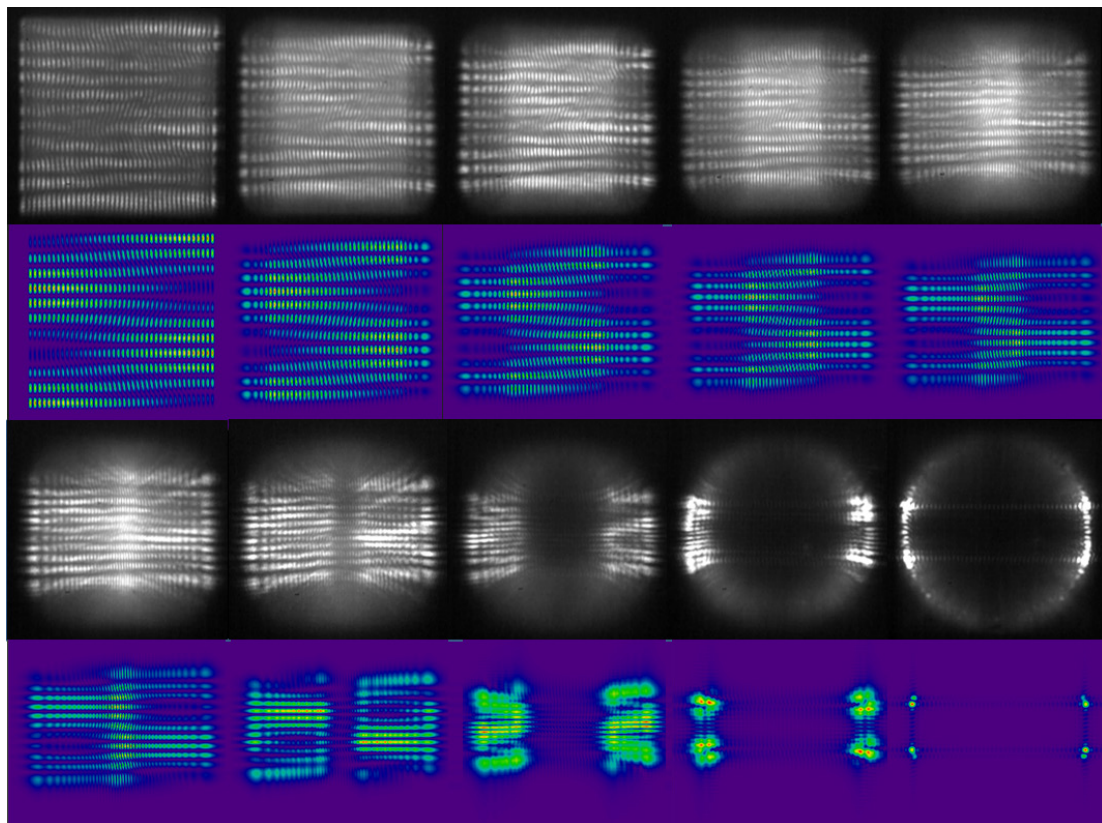


Fig. 2.8 The free-space propagation of a bouncing-ball near field. The experimental results are shown in first and third rows and the theoretical results are shown in the second and forth rows.

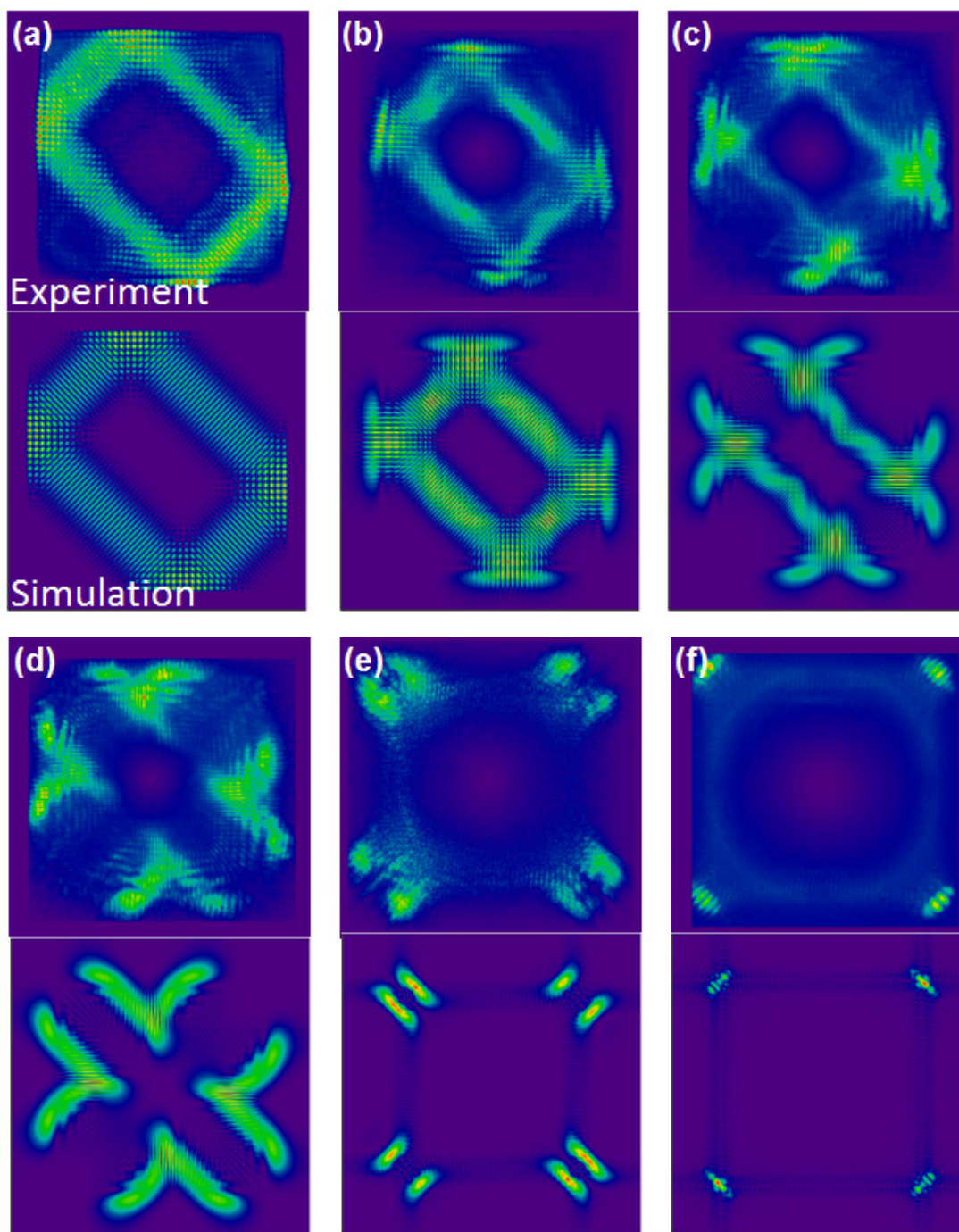


Fig. 2.9 The free-space propagation of a diamond-like superscar near field.

2.2 Large-aperture equilateral-triangular VCSEL

2.2.1 Theoretical analysis

Compared to the square shape infinity potential well, the shape in equilateral-triangular is classically integrable but non-seperable system. Let three vertices of an equilateral-triangular to be set at $(0, 0)$, $(a/2, \sqrt{3}a/2)$, and $(-a/2, \sqrt{3}a/2)$. The eigenstates in an equilateral-triangular infinity potential wall have been derived by several groups [9-11] and the wave functions of the two degenerate stationary states can be expressed as

$$\Phi_{m,n}^{(C)}(x, y) = \sqrt{\frac{16}{a^2 3\sqrt{3}}} \left\{ \cos \left[(m+n) \frac{2\pi}{3a} x \right] \sin \left[(m-n) \frac{2\pi}{\sqrt{3}a} y \right] \right. \\ \left. + \cos \left[(2m-n) \frac{2\pi}{3a} x \right] \sin \left[n \frac{2\pi}{\sqrt{3}a} y \right] \right. \\ \left. - \cos \left[(2n-m) \frac{2\pi}{3a} x \right] \sin \left[m \frac{2\pi}{\sqrt{3}a} y \right] \right\} \quad (2.7)$$

and

$$\Phi_{m,n}^{(S)}(x, y) = \sqrt{\frac{16}{a^2 3\sqrt{3}}} \left\{ -\sin \left[(m+n) \frac{2\pi}{3a} x \right] \sin \left[(m-n) \frac{2\pi}{\sqrt{3}a} y \right] \right. \\ \left. + \sin \left[(2m-n) \frac{2\pi}{3a} x \right] \sin \left[n \frac{2\pi}{\sqrt{3}a} y \right] \right. \\ \left. - \sin \left[(2n-m) \frac{2\pi}{3a} x \right] \sin \left[m \frac{2\pi}{\sqrt{3}a} y \right] \right\} \quad (2.8)$$

$\Phi_{m,n}^{(C)}(x, y)$ and $\Phi_{m,n}^{(S)}(x, y)$ have the following characteristics:

$$\Phi_{m,m}^{(C)}(x, y) = 0, \quad \Phi_{m,m}^{(S)}(x, y) = 0, \quad \Phi_{m,n}^{(C)}(x, y) = -\Phi_{n,m}^{(C)}(x, y), \quad \Phi_{m,n}^{(S)}(x, y) = -\Phi_{n,m}^{(S)}(x, y), \\ \Phi_{m,m-n}^{(C)}(x, y) = \Phi_{m,n}^{(C)}(x, y), \quad \text{and} \quad \Phi_{m,m-n}^{(S)}(x, y) = -\Phi_{m,n}^{(S)}(x, y). \quad (2.9)$$

Hence, the condition of $m \geq 2n$ is required to keep all eigenstates to be linearly independent to each other. Figures 2.10(a) and 2.10(b) show some of the $\Phi_{m,n}^{(C)}(x, y)$ and $\Phi_{m,n}^{(S)}(x, y)$ with their quantum number labeled below each picture. As similar to the wave function in square shape potential well, the eigenstates do not manifest the localization on periodic orbits even if the quantum number approaches to infinity.

For the stationary coherent states in equilateral-triangular infinity potential well, first, the traveling wave states are represented from linear combination of eigenstates:

$$\begin{aligned} \Phi_{m,n}^{\pm}(x, y) &= \Phi_{m,n}^{(C)}(x, y) \pm i\Phi_{m,n}^{(S)}(x, y) \\ &= \sqrt{\frac{16}{a^2 3\sqrt{3}}} \left\{ \exp\left[\pm i(m+n)\frac{2\pi}{3a}x\right] \sin\left[(m-n)\frac{2\pi}{\sqrt{3}a}y\right] \right. \\ &\quad + \exp\left[\mp i(2m-n)\frac{2\pi}{3a}x\right] \sin\left[n\frac{2\pi}{\sqrt{3}a}y\right] \\ &\quad \left. - \exp\left[\mp i(2n-m)\frac{2\pi}{3a}x\right] \sin\left[m\frac{2\pi}{\sqrt{3}a}y\right] \right\} \end{aligned} \quad (2.10)$$

Next, the stationary coherent states associated with periodic orbits denoted by (p, q, ϕ) in equilateral-triangular infinity potential well can be expressed as below [12,13].

$$\Psi_{M,N}^{\pm}(x, y; p, q, \phi) = \frac{1}{2^{N/2}} \sum_{K=0}^{M-1} C_K^M e^{\pm iK\phi} \Phi_{p(K+1), N+q(M-K)}^{\pm}(x, y) \quad (2.11)$$

A typical coherent states with $(p, q) = (1, 0)$ are showed in Fig. 2.11 in which the pattern with $\phi = \frac{\pi}{4}$ looks like an inverse cane.

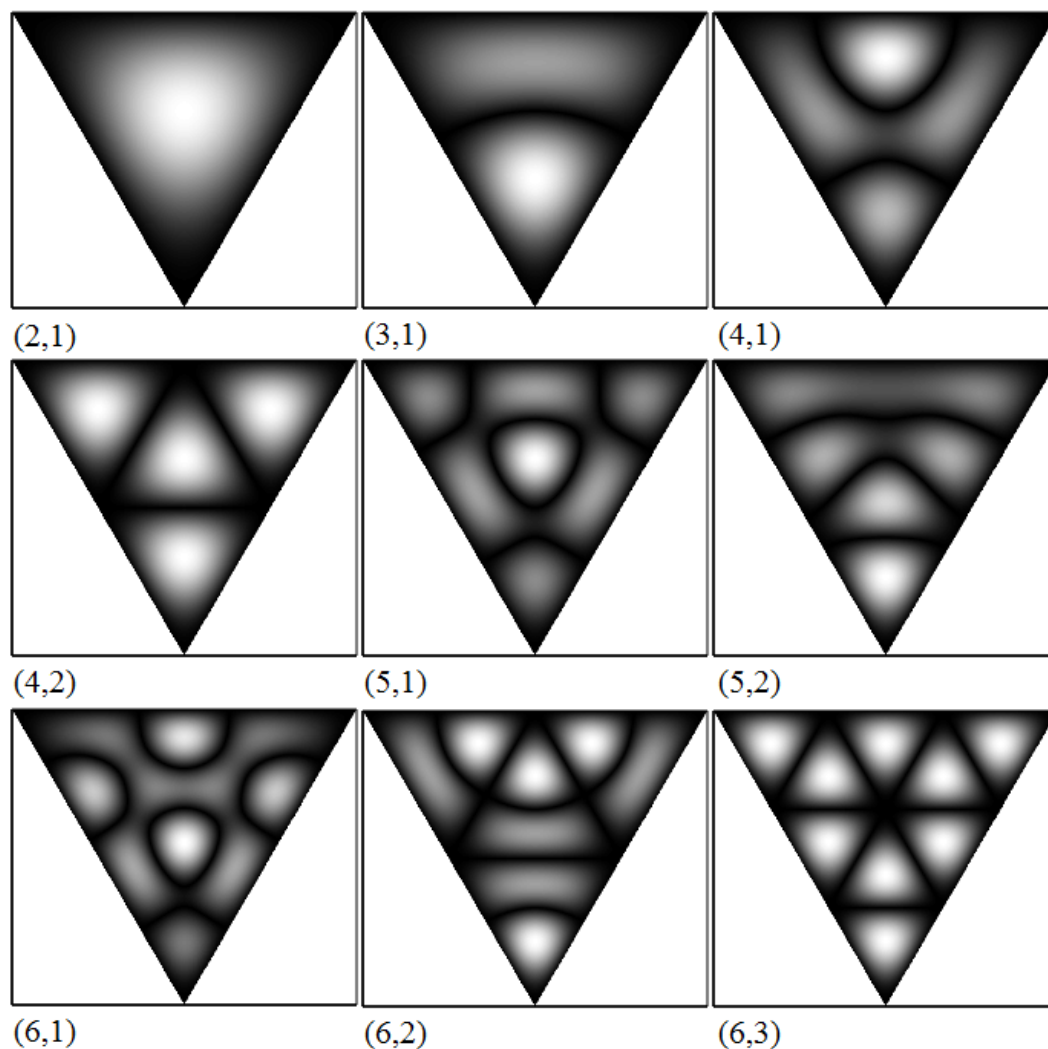


Fig. 2.10 (a) Some eigenstates of equilateral-triangular 2D infinity potential well

$$|\Phi_{m,n}^{(C)}(x,y)|.$$

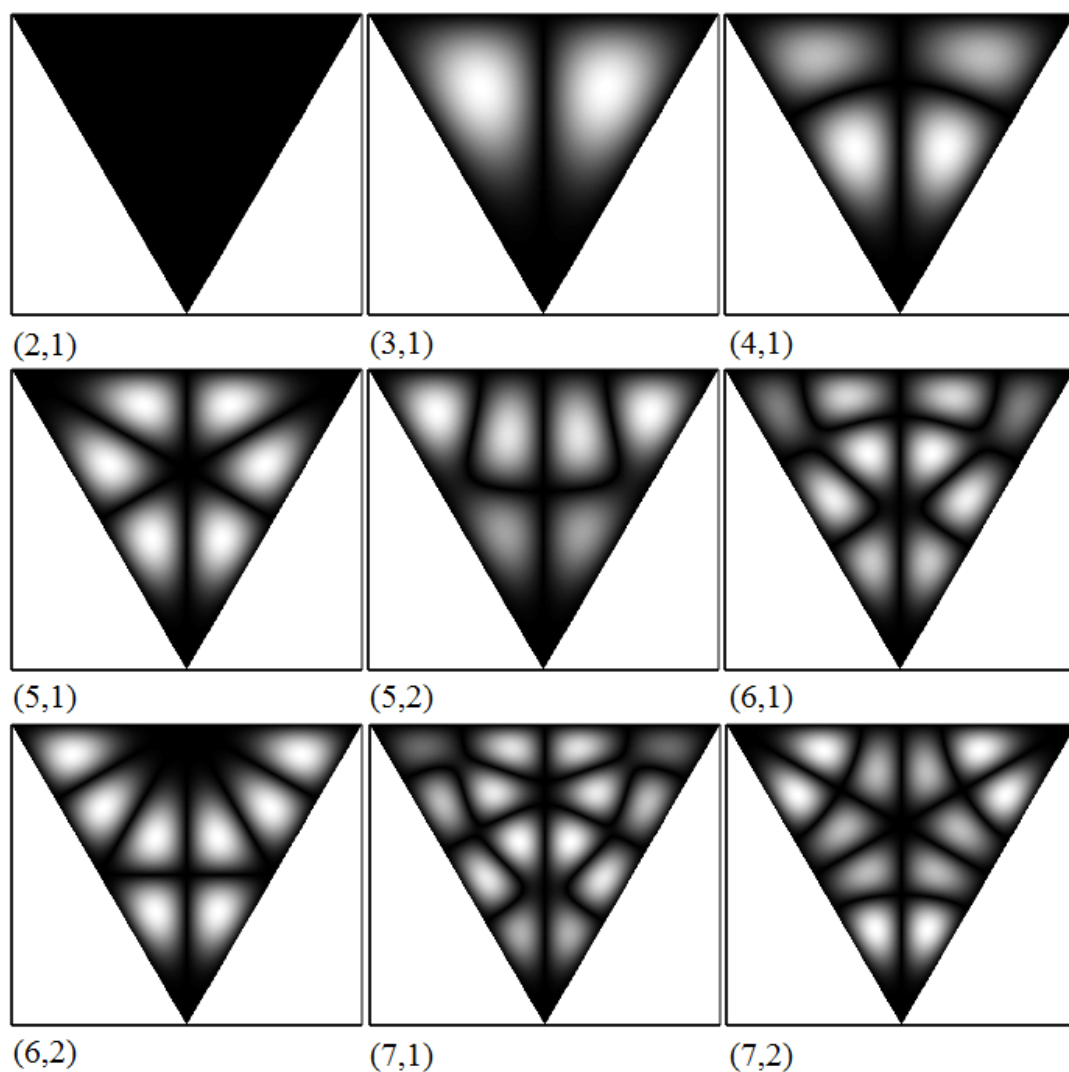


Fig. 2.10 (b) Some eigenstates of equilateral-triangular 2D infinity potential well

$|\Phi_{m,n}^{(S)}(x,y)|$. When $m=2n$, $\Phi_{m,n}^{(S)}(x,y) = 0$.

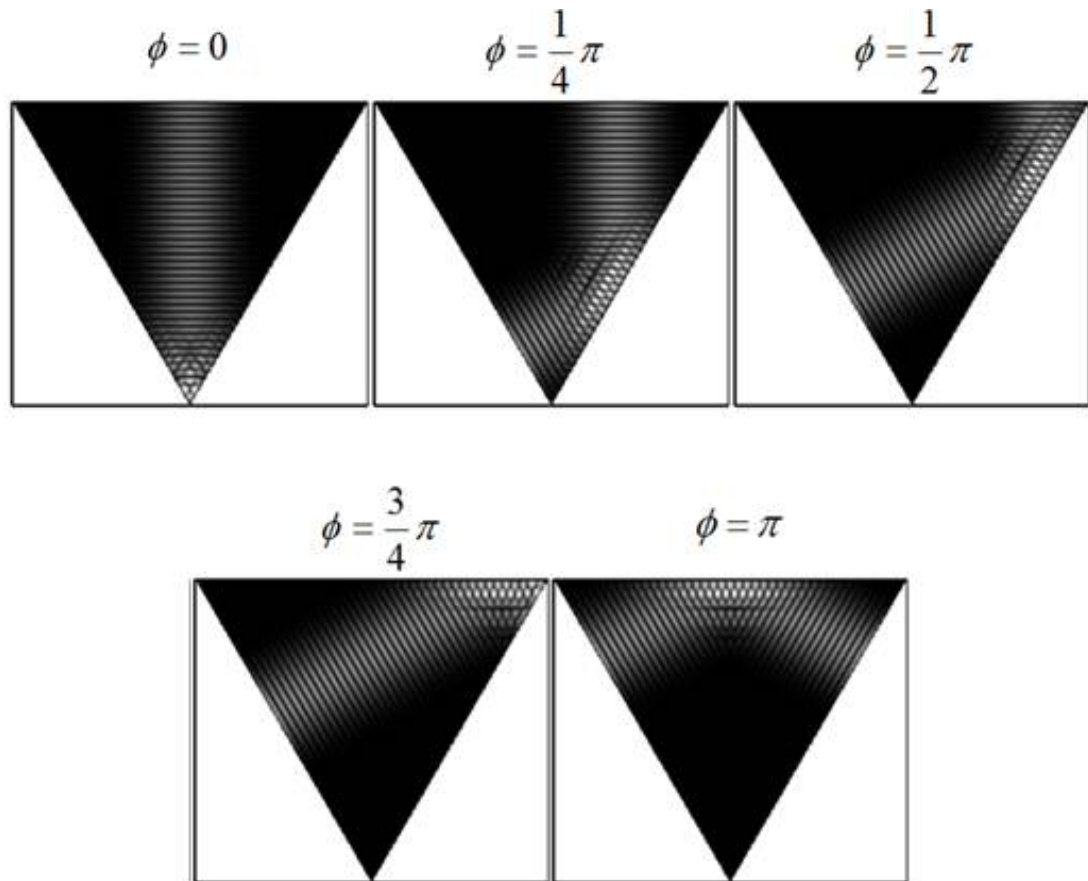


Fig. 2.11 Stationary coherent states of $|\Psi_{42,20}^+(x, y; 1, 0, \phi)\rangle$ with different ϕ .

2.2.2 Experimental setup

The experimental setup is the same as shown in Fig. 2.4. The VCSEL device was placed in a cryogenic system with a temperature stability of 0.01 K in the range of 80–300 K. A DC power supplier (KEITHLEY 2400) with a precision of 0.005 mA is used to drive the VCSEL device. The near-field patterns were reimaged into a charge-coupled device (CCD) camera (Coherent, Beam Code) with an objective lens (Mitsutoyo, NA of 0.9). The far-field patterns are measured with a CCD placed behind a screen.

The schematic of the laser device structure with equilateral-triangular shape is shown in Fig. 2.12. The edge length of the oxide aperture is approximate $66.8 \mu\text{m}$.

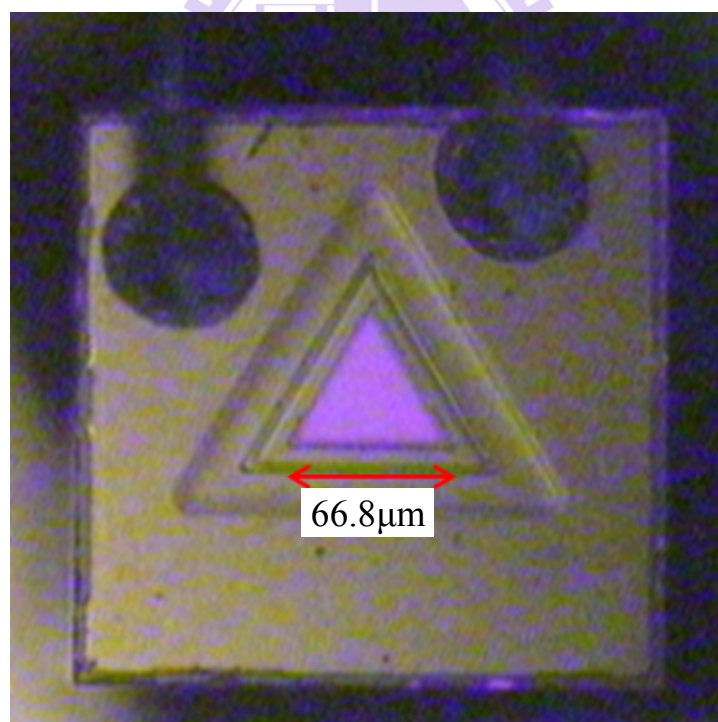


Fig. 2.12 Schematic of the large-aperture equilateral-triangular laser device structure.

2.2.3 Results and discussion

The experimental near-field morphologies are shown in Figs. 2.13(a)–(c) with different temperatures as labeled in each figure. Additionally, the corresponding far-field patterns for the honeycomb eigenmode, the cane-like superscar mode, and the superscar mode with $(p, q) = (1, 1)$ [14] are shown in Figs. 2.13(a')–(c'). We can see that the near-field patterns for the honeycomb eigenmode and the superscar mode with $(p, q) = (1, 1)$ are conspicuously different to each other. However, their far-field patterns display fairly similar directional emission. The directional emission for a superscar mode can be easily traced from its localization in the near-field feature, as shown in section 2.1.3. Conversely, it is demanding to find the directional emission of a honeycomb lasing mode.

As described in section 2.2.1, the eigenstates for the standing waves are given by $\Phi_{m,n}^{(C)}(x, y)$ and $\Phi_{m,n}^{(S)}(x, y)$ as shown below:

$$\begin{aligned} \Phi_{m,n}^{(C)}(x, y) = \sqrt{\frac{16}{a^2 3\sqrt{3}}} \left\{ \cos \left[(m+n) \frac{2\pi}{3a} x \right] \sin \left[(m-n) \frac{2\pi}{\sqrt{3}a} y \right] \right. \\ + \cos \left[(2m-n) \frac{2\pi}{3a} x \right] \sin \left[n \frac{2\pi}{\sqrt{3}a} y \right] \\ \left. - \cos \left[(2n-m) \frac{2\pi}{3a} x \right] \sin \left[m \frac{2\pi}{\sqrt{3}a} y \right] \right\} \end{aligned} \quad (2.7)$$

and

$$\begin{aligned} \Phi_{m,n}^{(S)}(x, y) = \sqrt{\frac{16}{a^2 3\sqrt{3}}} \left\{ -\sin \left[(m+n) \frac{2\pi}{3a} x \right] \sin \left[(m-n) \frac{2\pi}{\sqrt{3}a} y \right] \right. \\ + \sin \left[(2m-n) \frac{2\pi}{3a} x \right] \sin \left[n \frac{2\pi}{\sqrt{3}a} y \right] \\ \left. - \sin \left[(2n-m) \frac{2\pi}{3a} x \right] \sin \left[m \frac{2\pi}{\sqrt{3}a} y \right] \right\} \end{aligned} \quad (2.8)$$

In terms of $\Phi_{m,n}^{(S)}(x, y)$, the experimental honeycomb pattern can be well reconstructed with $n=60$ and $m=6$, as depicted in Fig. 2.14(a). On the other hand, the Superscar modes associated with classical periodic orbits can be analytically expressed with the coherent states.

$$\Psi_{M,N}^{\pm}(x, y; p, q, \phi) = \frac{1}{2^{N/2}} \sum_{K=0}^{M-1} C_k^M e^{\pm iK\phi} \Phi_{p(K+1), N+q(M-K)}^{\pm}(x, y) \quad (2.11)$$

And the standing wave $C_{N,M}^{\pm}(x, y; p, q, \phi)$ is represented:

$$C_{N,M}^{\pm}(x, y; p, q, \phi) = \Psi_{N,M}^{+}(x, y; p, q, \phi) \pm \Psi_{N,M}^{-}(x, y; p, q, \phi) \quad (2.12)$$

The experimental superscar pattern in Fig. 2.13(b) can be well reconstructed by $|C_{N,M}^{+}(x, y; p, q, \phi)|^2$ with $N=36$, $M=9$, and $(p, q, \phi) = (1, 0, 0.23\pi)$, as depicted in Fig. 2.14(b). In the same way, the experimental superscar pattern in Fig. 2.13(c) is related to the theoretical solution $|C_{N,M}^{+}(x, y; p, q, \phi)|^2$ with $N=22$, $M=6$, and $(p, q, \phi) = (1, 1, 0.3\pi)$, as depicted in Fig. 2.14(c). The theoretical analysis of the far field can be implemented by combining the numerical near-field pattern and the equation of Fraunhofer diffraction. The calculation results of far field are shown in Fig. 2.14(a') for honeycomb eigenmode, Fig. 2.14(b') for superscar (1,0) mode, and Fig. 2.14(c') for superscar (1,1) mode. The excellent agreements between the experimental and numerical patterns again confirm that the model of quantum system in infinity potential well is great important to analogically simulate the transverse lasing modes of the VCSELs, and this work was proposed in Ref. [15].

The experimental and theoretical results show that the near-field patterns for the honeycomb eigenmode and the superscar mode (Figs. 2.13(a) and (c) and Figs. 2.14(a) and (c)) are apparently different to each other. One spreads over the triangular space while the other one is localized on the periodic orbit with trajectory parallel to the three edges of the triangle. However, their far-field patterns display fairly similar directional emission with the angles at integral multipliers of 60° . As a consequence, we confirm that the far-field directional emission is just a necessary not sufficient condition for the emergence of a superscar mode [15].

For detailed exploring the far fields of the honeycomb eigenmode and the superscar mode, the experimental results are redraw in Fig. 2.15 and the numerical patterns are calibrated by changing the index of square in $|C_{N,M}^+(x, y; p, q, \phi)|^2$ to $|C_{N,M}^+(x, y; p, q, \phi)|^{0.8}$ for diminishing the contrast of the image and emphasizing the delicate morphology. There are two apparent differences between the far-fields in Fig. 2.15: the structures of the six points in each directional emission and the lines connected between the six points. Interestingly, these lines form two triangles with a shape in hexagram which is the well-known Magen David (Star of David).

In the far field of honeycomb eigenmode, there are two dots in each six directions of directional emission. As a result, there are total 12 dots in the far field. These dots can be explained by dividing the eigenstate $\Phi_{m,n}^{(S)}(x, y)$ into three parts, each part is familiar to the eigenstates of a rectangle-shape infinity potential well. The three parts are as listed:

$$\sin\left[\left(m+n\right)\frac{2\pi}{3a}x\right]\sin\left[\left(m-n\right)\frac{2\pi}{\sqrt{3}a}y\right], \quad \sin\left[\left(2m-n\right)\frac{2\pi}{3a}x\right]\sin\left[n\frac{2\pi}{\sqrt{3}a}y\right], \quad \text{and} \\ \sin\left[\left(2n-m\right)\frac{2\pi}{3a}x\right]\sin\left[m\frac{2\pi}{\sqrt{3}a}y\right].$$

As shown in the section 2.1.3, the far field emitted from a rectangle-shape aperture VCSEL has 4 points on each directional emission. Based on this result, the 12 dots and its locations in the far field of a honeycomb near-field pattern are apparently reasonable.

Despite the 12 dots, the lines in Magen David can not get well explain from the results of the far fields emitted from a rectangle-shape aperture VCSEL. Actually, the lines are not real line but the interference patterns, and amazingly, the lines used to connect the six dots form one of the triangular in Magen David with a close loop (one touch drawing), as shown in Fig. 2.16. The detailed formation about this line is related to the superposition of the wave function for constructing the near-field transverse modes. For example, a summation of a group of sin waves to create a sinc function, because the number of the sin waves in the group is finite, there will exist some fluctuations between the peaks of sinc function. As a result, in the far field of VCSELs, it usually exist some interference-line patterns connected between each dots [6,7,16].

Based on the explanation of the Magen David emitted from honeycomb near-field pattern, the Magen David in the far field of a superscar mode (1,1) is explained as follows. The locations of the 12 dots are related to the quantum numbers of the eigenstates as confirmed by the far field of a rectangle-shape aperture VCSEL. When a group of eigenstates with different eigenvalues is combined to generate a coherent state $|C_{N,M}^+(x, y; p, q, \phi)\rangle^2$, several groups of 12 dots will overlap to form six elliptical dots on each directional emission and the lines in Magen David will be plaited to a ribbon, as shown in Fig. 2.15.

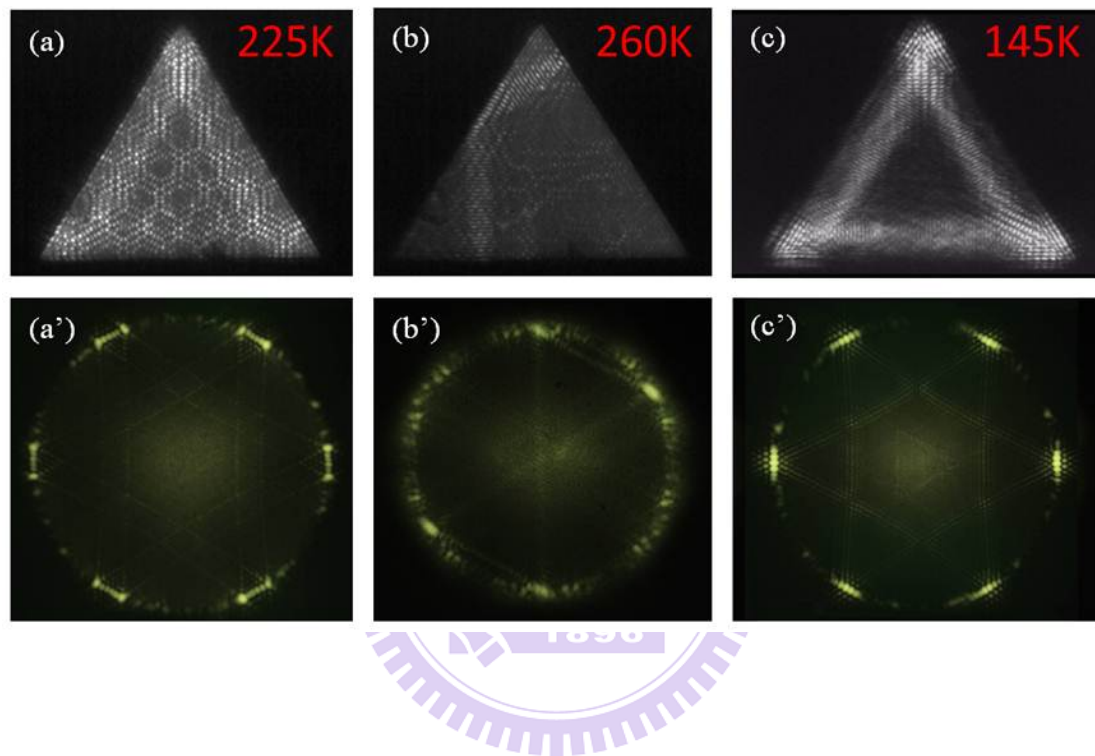


Fig. 2.13 Experimental near-field morphologies: (a) honeycomb eigenmode, (b) cane-like superscar (1,0) mode, (c) superscar (1,1) mode. The far-field patterns (a'), (b'), and (c') correspond to (a), (b), and (c), respectively.

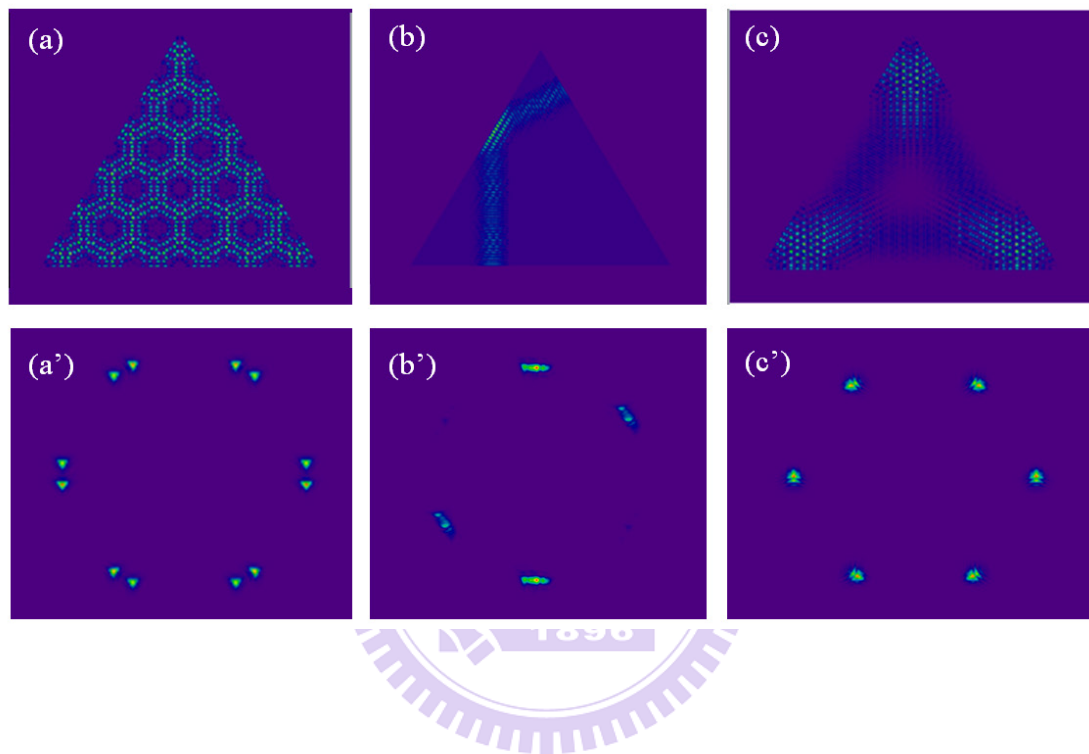


Fig. 2.14 Theoretical near-field morphologies: (a) honeycomb eigenmode, (b) cane-like superscar (1,0) mode, (c) superscar (1,1) mode. The far-field patterns (a'), (b'), and (c') correspond to (a), (b), and (c), respectively.

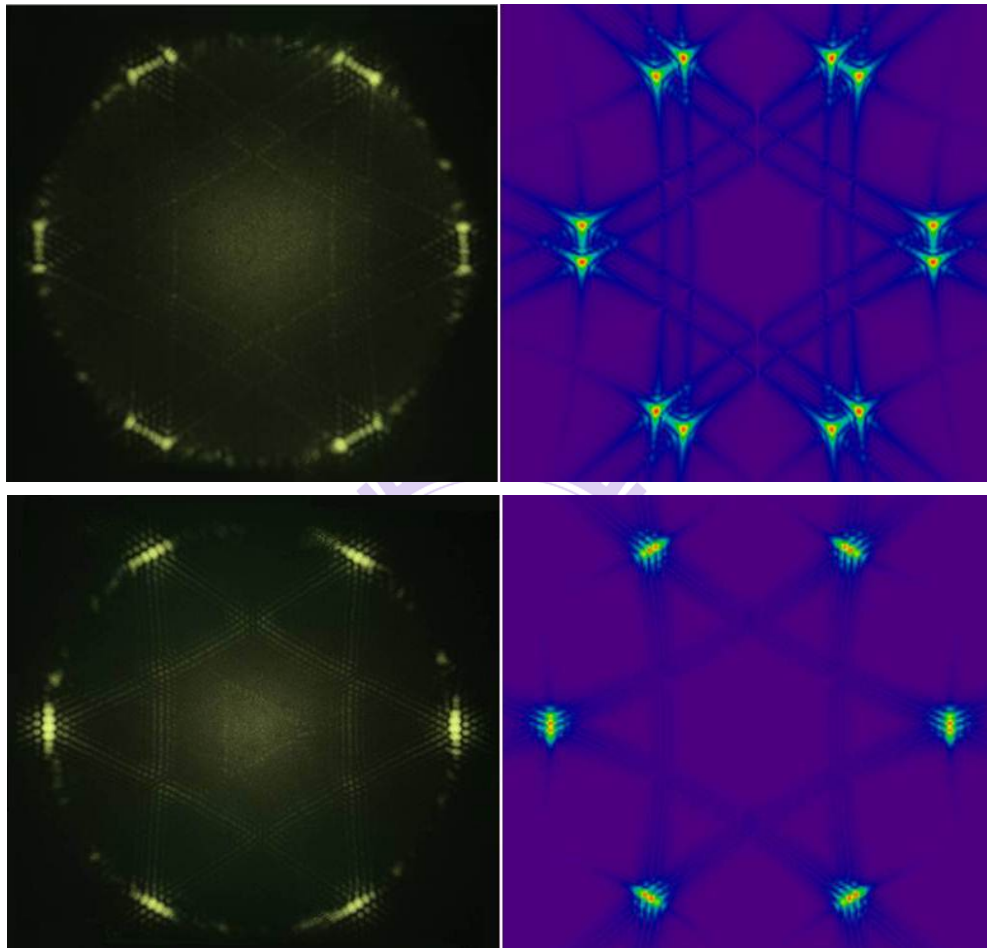


Fig. 2.15 The experimental and Theoretical far-field patterns from honeycomb pattern (above) and superscar (1,1) mode (bottom) in near field. The morphology of the numerical patterns is enhanced.

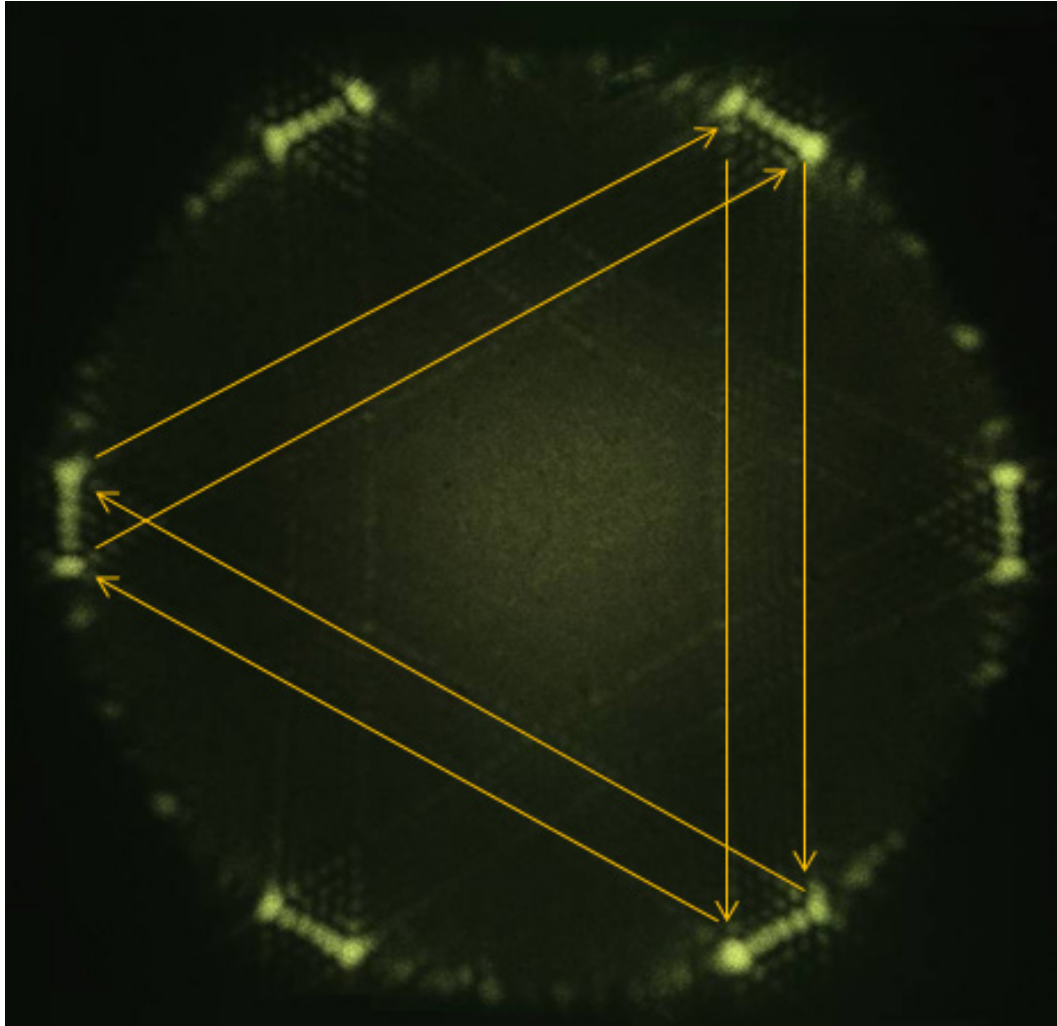


Fig. 2.16 Six points on one of the triangular of Magen David is connected with only one touch.

Furthermore, we explore the free space propagations of the transverse modes emitted from VCSELs for understanding the directional emissions from some typical lasing modes in equilateral-triangular VCSEL. The light evolution emitted from VCSEL with a honeycomb lasing mode is shown in Fig. 2.17. The results are conspicuously different to the eigenmodes of square boundary in Fig. 2.8. The honeycomb lasing mode analogously splits into three honeycomb patterns and each pattern propagate out from the three edges of triangular boundary with direction vertical to each edge. During the evolution, an inverse triangular window is gradually opening on the center of the diffraction pattern. This window cuts the three divided honeycomb patterns to six dots with interference structure.

The free-space propagations of the superscar $(1,0)$ and $(1,1)$ modes are shown in Figs. 2.18 and 2.19, respectively. The second and fourth rows in the Figs. 2.18 and 2.19 depict the numerical patterns calculated from combining the theoretical near-field patterns and the Fresnel diffraction integral (eq. A.9). In Fig. 2.18, the characteristic of the diffraction patterns show a distorted trajectory followed the direction parallel to the left bevel edge as same as the diamond-like superscar mode in square-aperture VCSEL. For the diffraction of superscar $(1,1)$ mode, there are another six points in the diffraction patterns (six lines in diffraction space) and such six points are explained in Fig 2.20. There are three short dash lines in the three corners which are hardly observed in the experimental measurement (Fig. 2.19), and these short dash lines will form the six points.

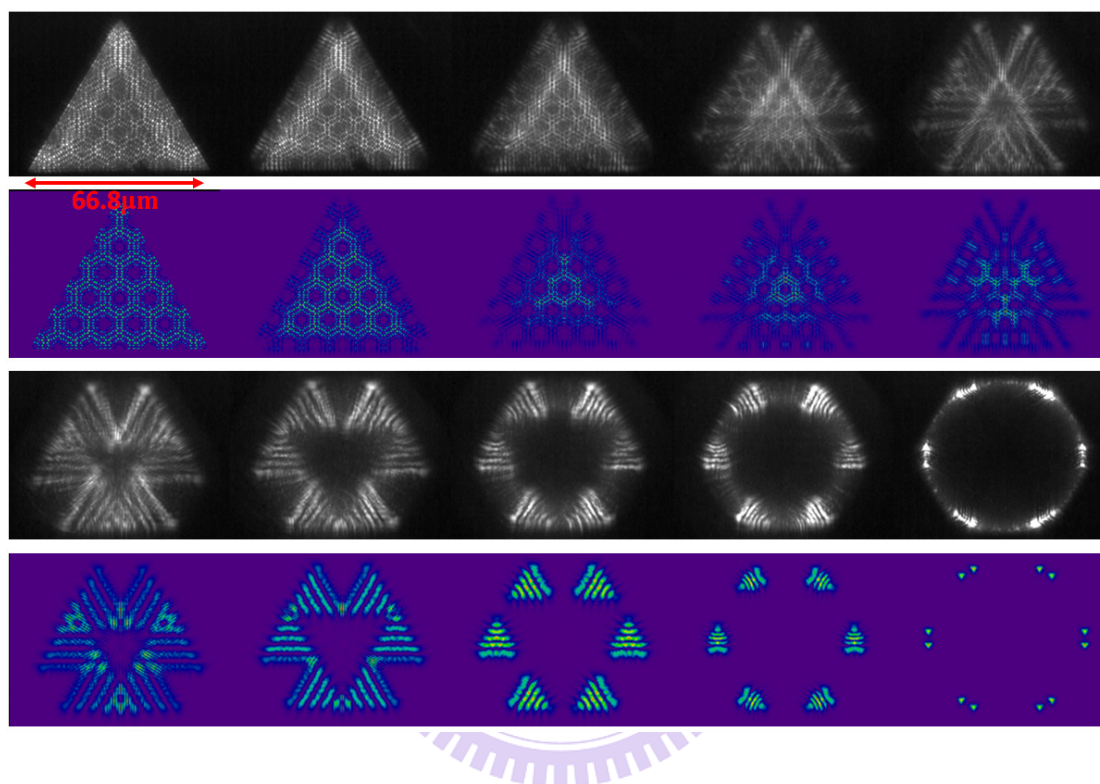


Fig. 2.17 Experimental and theoretical results of free-space propagation of the honeycomb eigenmode. The experimental results are shown in first and third rows and the theoretical results are shown in the second and forth rows.

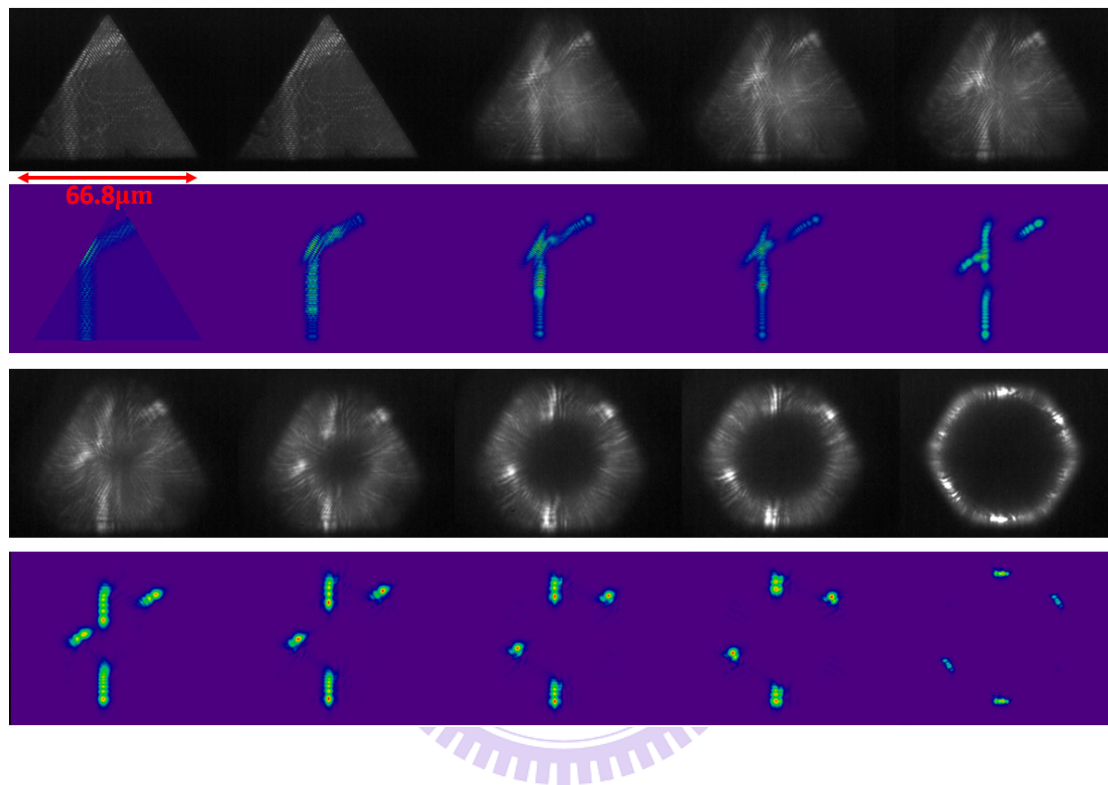


Fig. 2.18 Experimental and theoretical results of free-space propagation of the cane-like superscar $(1,0)$ mode. The experimental results are shown in first and third rows and the theoretical results are shown in the second and forth rows.

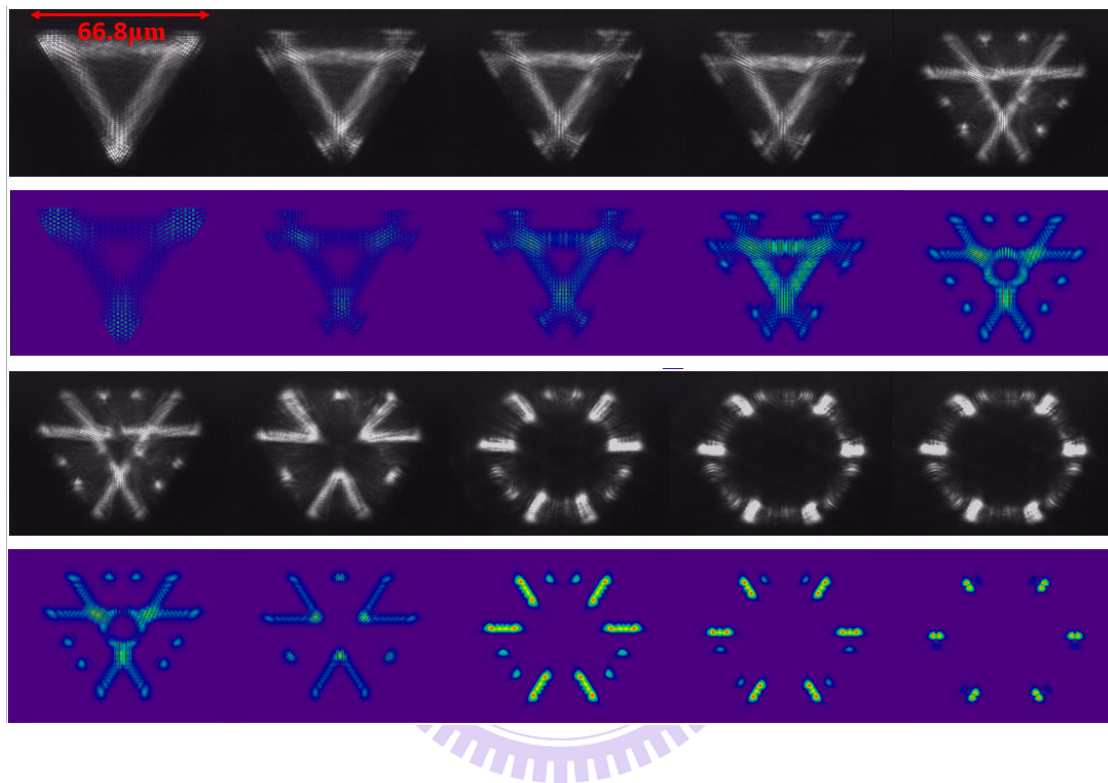


Fig. 2.19 Experimental and theoretical results of free-space propagation of the superscar (1,1) mode. The experimental results are shown in first and third rows and the theoretical results are shown in the second and forth rows.

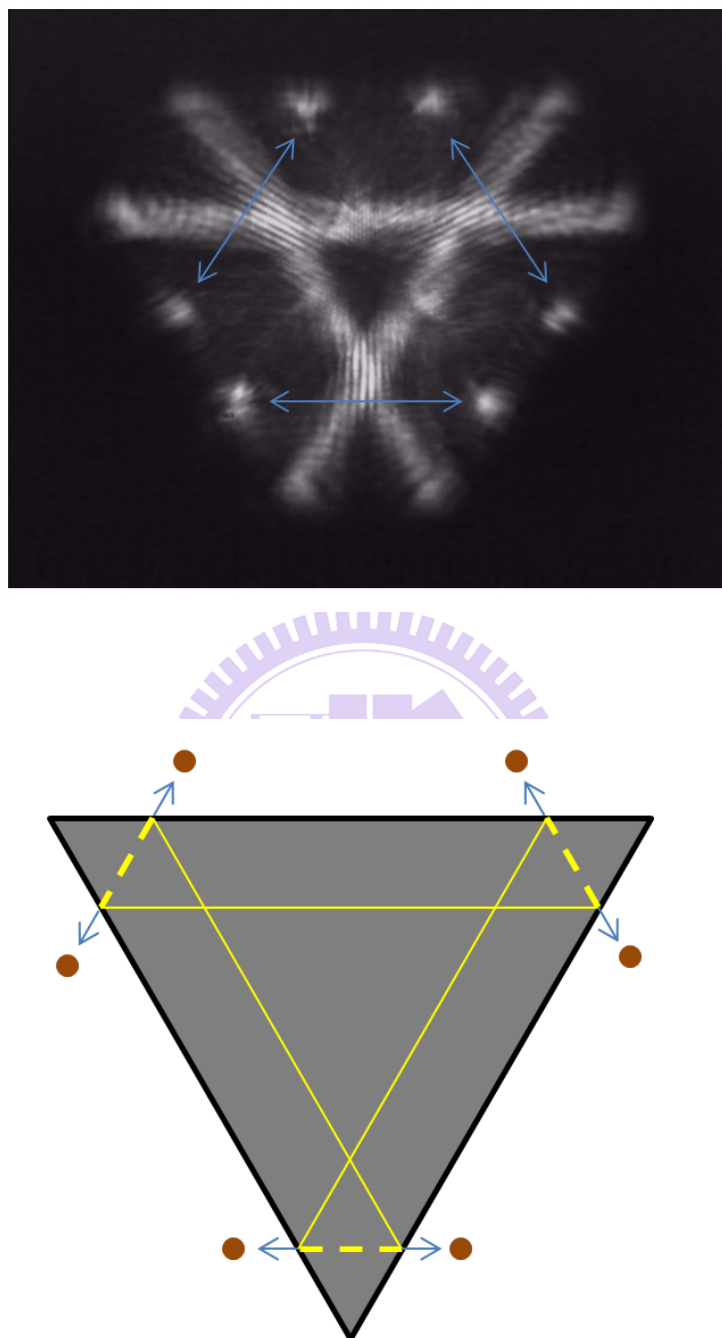


Fig. 2.20 The formation about six points in the diffraction pattern of the experimental results. The schematic picture about these propagations of six points is also shown.

Reference

- [1] J. J. Sakurai, *Modern Quantum Mechanics* (Addison Wesley, 1993).
- [2] R. Shankar, *Principles of Quantum Mechanics, 2nd Edition* (Plenum Press, 2nd, 1994).
- [3] E. Schrödinger, *Collected papers on wave mechanics*, New York, Chelsea. **41** (1978).
- [4] Y. F. Chen, K. F. Huang, and Y. P. Lan “Quantum manifestations of classical periodic orbits in a square billiard: Formation of vortex lattices,” *Phys. Rev. E* **66**, 066210 (2002).
- [5] R. W. Robinett, “Visualizing classical periodic orbits from the quantum energy spectrum via the Fourier transform: Simple infinite well examples,” *Am. J. Phys.* **65**, 1167 (1997).
- [6] C. C. Chen, “Analogous investigation on the transverse modes of broad-area vertical-cavity surface-emitting laser by mesoscopic wave function of quantum billiard,” Ph. D. thesis, National Chiao Tung University of Taiwan (2009).
- [7] C. C. Chen, Y. T. Yu, Ross C. C. Chen, Y. J. Huang, K. W. Su, Y. F. Chen, and K. F. Huang, “Transient Dynamics of Coherent Waves Released from Quantum Billiards and Analogous Observation from Free-Space Propagation of Laser Modes,” *Phys. Rev. Lett.* **101**, 044101 (2009).
- [8] A. Backer and R. Schubert, “Chaotic eigenfunctions in momentum space,” *J. Phys. A: Math. Gen.* **32**, 4795 (1999).
- [9] G. B. Shaw, “Degeneracy in the Particle-in-a-Box Problem,” *J. Phys. A* **7**, 1537 (1974).
- [10] R. J. Richens and M. V. Berry, “Pseudointegrable Systems in Classical and Quantum Mechanics,” *Physica D* **2**, 495-512 (1981).

- [11] W. K. Li and S. M. Blinder, "Solution of the Schrödinger Equation for a Particle in an Equilateral Triangle," *J. Math. Phys.* **26**, 2784-2786 (1985).
- [12] Y. F. Chen and K. F. Huang, "Vortex Formation of Coherent Waves in Nonseparable Mesoscopic Billiards," *Phys. Rev. E* **68**, 066207 (2003).
- [13] C. C. Chen, K. W. Su, Y. F. Chen, and K. F. Huang "Various high-order modes in vertical-cavity surface-emitting lasers with equilateral triangular lateral confinement," *Opt. Lett.* **33**, 509-511 (2008).
- [14] H. C. Chang, G. Kioseoglou, E. H. Lee, J. Haetty, M. H. Na, Y. Xuan, H. Luo, and A. Petrou, "Lasing modes in equilateral-triangular laser cavities," *Phys. Rev. A.* **62**, 013816 (2000).
- [15] Ross C. C. Chen, Y. T. Yu, Y. J. Huang, C. C. Chen, Y. F. Chen, and K. F. Huang, "Exploring the origin of the directional emission from a microcavity with a large-aperture surface-emitting laser," *Opt. Lett.* **34**(12), 1810-1812 (2009).
- [16] Y. T. Yu, Y. J. Huang, P. Y. Chiang, Y. C. Lin, K. F. Huang, and Y. F. Chen "Non-paraxial contributions to the far-field pattern of surface-emitting lasers: a manifestation of the momentum-space wavefunctions of quantum billiards," *J. Opt.* **13**, 075705 (2011).

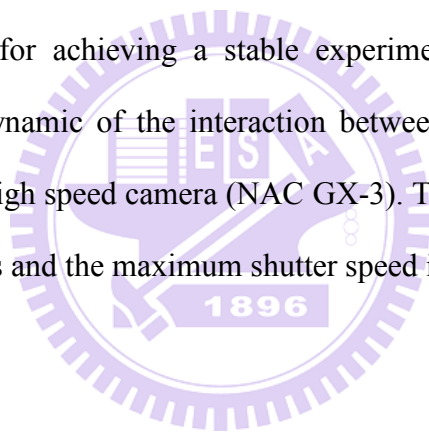
Chapter 3. Laser-induced breakdown beneath a flat water surface – Vertical focusing

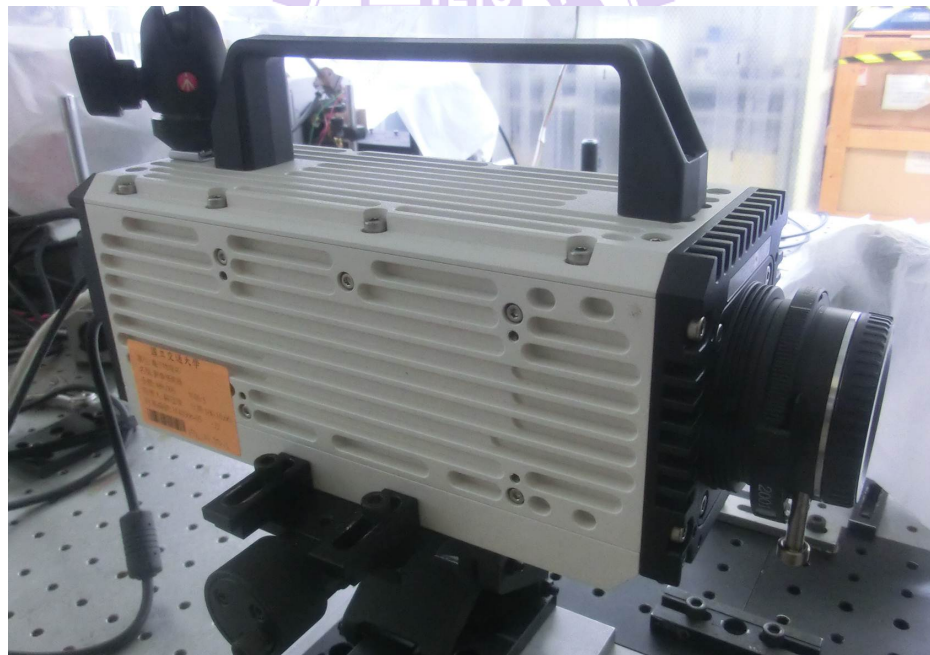
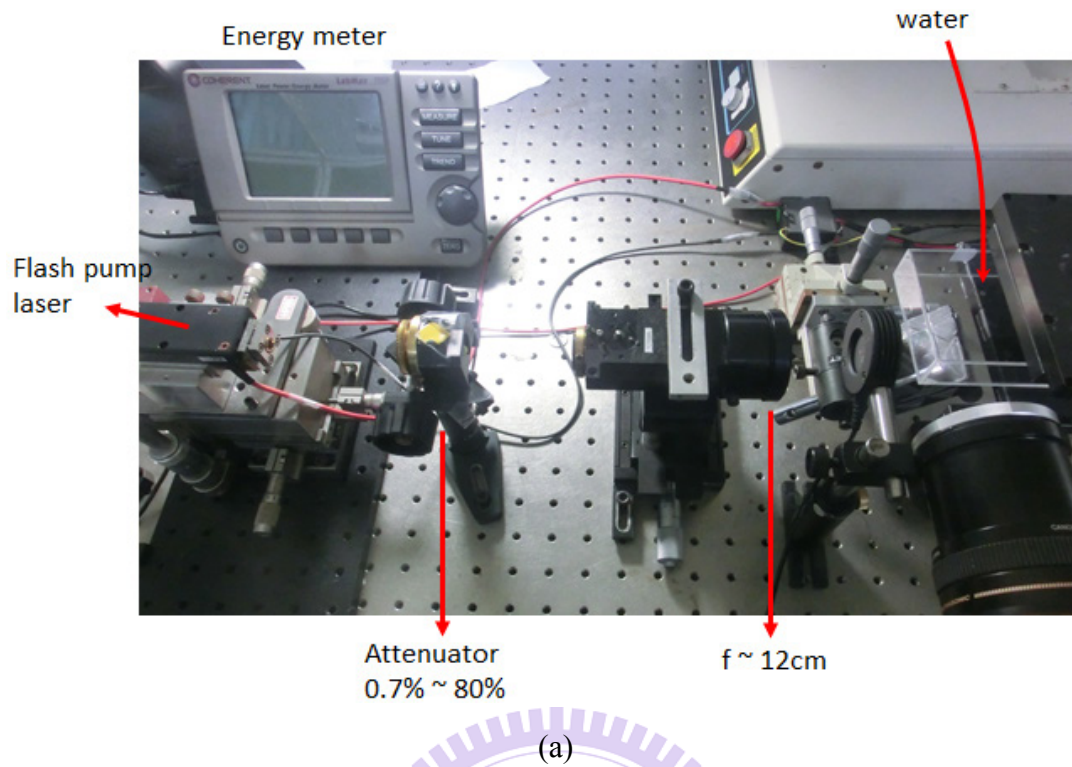
The most significant parameter affecting the dynamical properties of the liquid jet is the parameter γ of initial bubble depth over maximum bubble radius [1-3]. This γ is also a feasible technological parameter in several applications such as quality optimization in film-free LIFT [4, p.101]. Therefore, in this chapter, we characterize the liquid jet as a function of γ and investigate its morphology and generation. Experimentally, a nanosecond pulsed laser with wavelength 1064 nm is used to induce water breakdown, and a bubble with millimeter size is generated beneath a flat free surface. The overall behavior of interaction between the bubble and the free surface is recorded by a high speed camera. Furthermore, we systematically explore the morphological changes in the temporal evolution of the water jet.

3.1 Experimental setup

A schematic diagram of the experimental arrangement is shown in Fig. 3.1. A bubble is generated beneath a free surface by focusing a flash-pump pulsed laser (Nd:YAG, $\lambda = 1064$ nm) with a pulse width 6 ns from below a water tank vertically into tap water at a room temperature 297 K under atmospheric pressure. The dimension of the tank is $100 \times 70 \times 20$ mm³ and the depth of water is 13 mm for alleviating the influence on the bubble from the bottom wall of the tank. The output

beam of the laser with beam waist 1.5 mm is enlarged 10 times its original size by employing a lens array with one biconcave lens and two convex lenses. Then, a lens with a focal length of 12 cm in air and a mirror with high-reflection coated at 1064 nm are used to focus the enlarged beam vertically beneath the free surface to form a point plasma followed by a cavitation bubble. The output energy of the laser is around 22 mJ beam and is attenuated by an attenuator. As a result, the energy after the mirror can be controlled from about 0.15 mJ to 18 mJ. The initial bubble shape with different laser energy is shown in Fig. 3.2 and the maximum bubble diameter is shown in Fig. 3.3. In this work, the energy of laser is set to 18 mJ because the maximum bubble diameter is gradually saturated as shown in Fig 3.3, and the fluctuation of the bubble size will be minimized for achieving a stable experimental measurement on the bubble dynamics. The dynamic of the interaction between the bubble and the free surface is recorded by a high speed camera (NAC GX-3). The maximum frame rate of NAC GX-3 is 198,000 fps and the maximum shutter speed is 1 μ s.





(a)

(b)

Fig. 3.1 (a) The Experimental setup. (b) The high speed camera of GX-3 which is setup at the right down corner of Fig. 3.1(a).

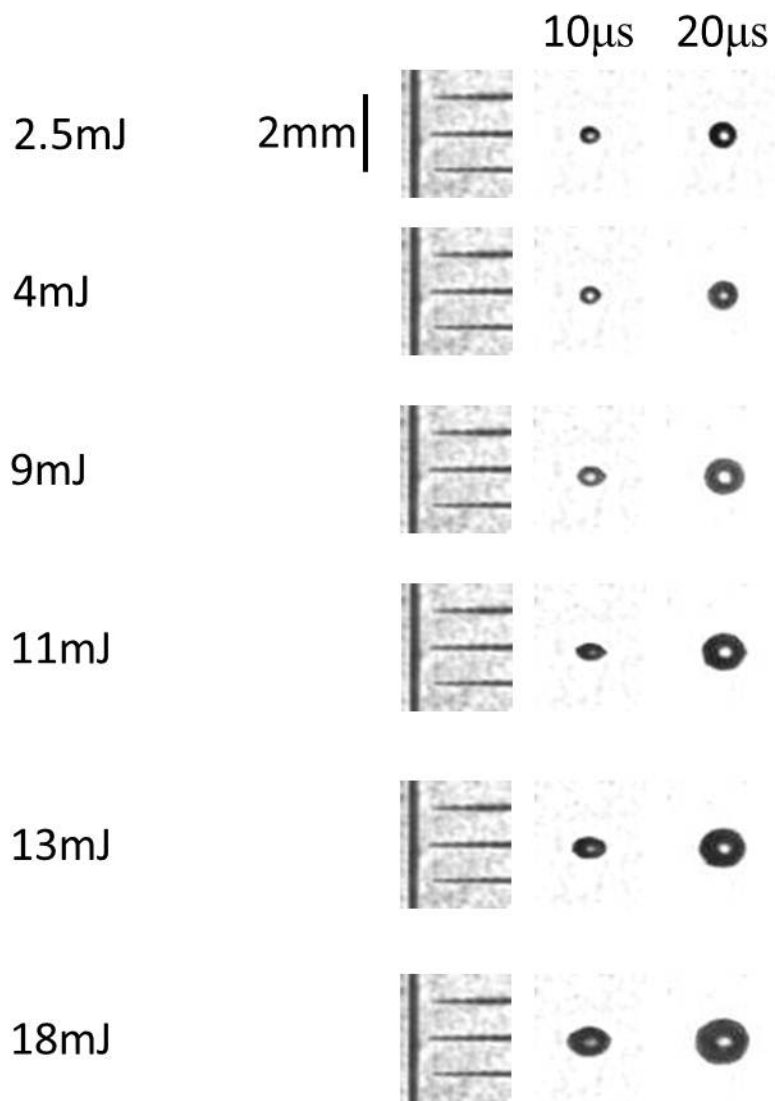


Fig. 3.2 The initial bubble shape with different laser energy. The frame rate is 10,000 fps and the time of each frame is labeled on the top.

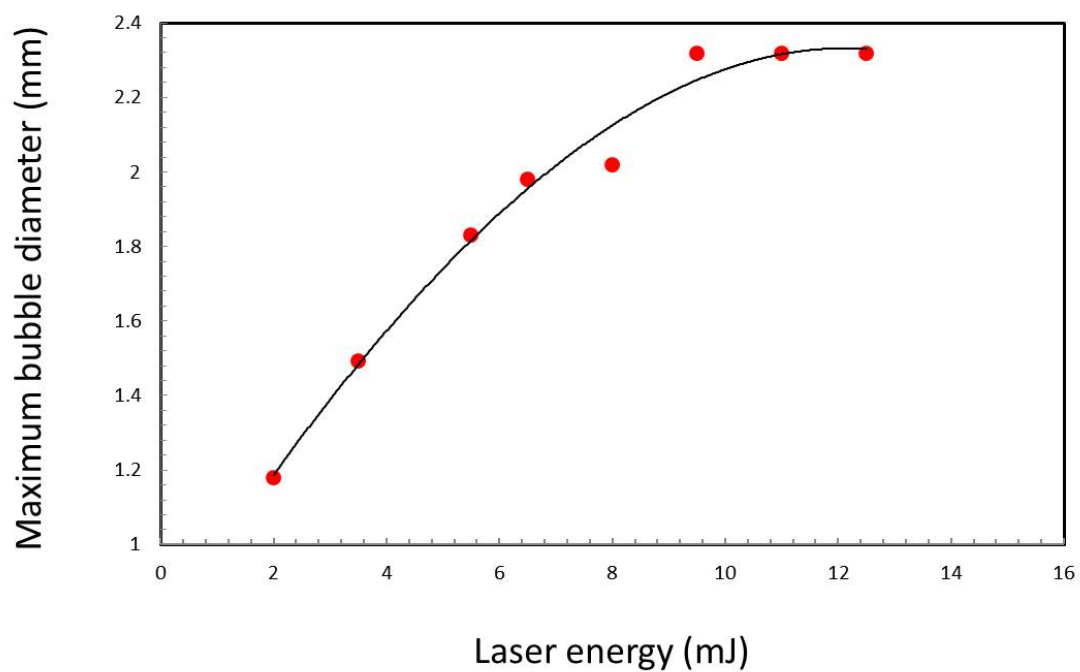


Fig. 3.3 The maximum bubble diameter with different laser energy. The solid line is a guide for the eye.

3.2 Results and discussion

In this section, we observe the water jet on the free surface with different bubble depth. The water jet shows a rich structure and various feature when the bubble depth is changed. The mechanism of each part of the water jet is also discussed in detail.

3.2.1 Thin jet, thick jet, and crown formation

Figure 3.4 clearly shows a typical dynamic of a shallow underwater oscillating bubble and a water jet with complete structure and morphology on the free surface. The depth of the bubble from the free surface is 0.8 defined in stand-off parameter γ (h / R_{\max} , h is initial distance between the center of the bubble and the free surface, R_{\max} is maximum bubble radius). As shown, the bubble extrudes a thin jet during its period of first expansion, as similar as described in recent works [1-3], and the thin jet continues to rise after the first expansion. At the end of the first expansion, the bubble starts to collapse due to the pressure decrease inside the bubble and moves downward, leading to the sinking around the surface on the bottom of the thin jet. This sinking surface was previously referred as surface depression [5]. When the sinking surface reaches its maximum depth, the surrounding water will flow toward the crater of the sinking surface, resulting in moving upward of the maximum depth point and the formation of the thick jet under the thin jet on the free surface [5]. Eruption of liquid jets from collapsing depressions has been observed in other circumstances, like standing Faraday-waves [6] and free-fall of a drop [7] on a liquid surface, and granular jets [8].

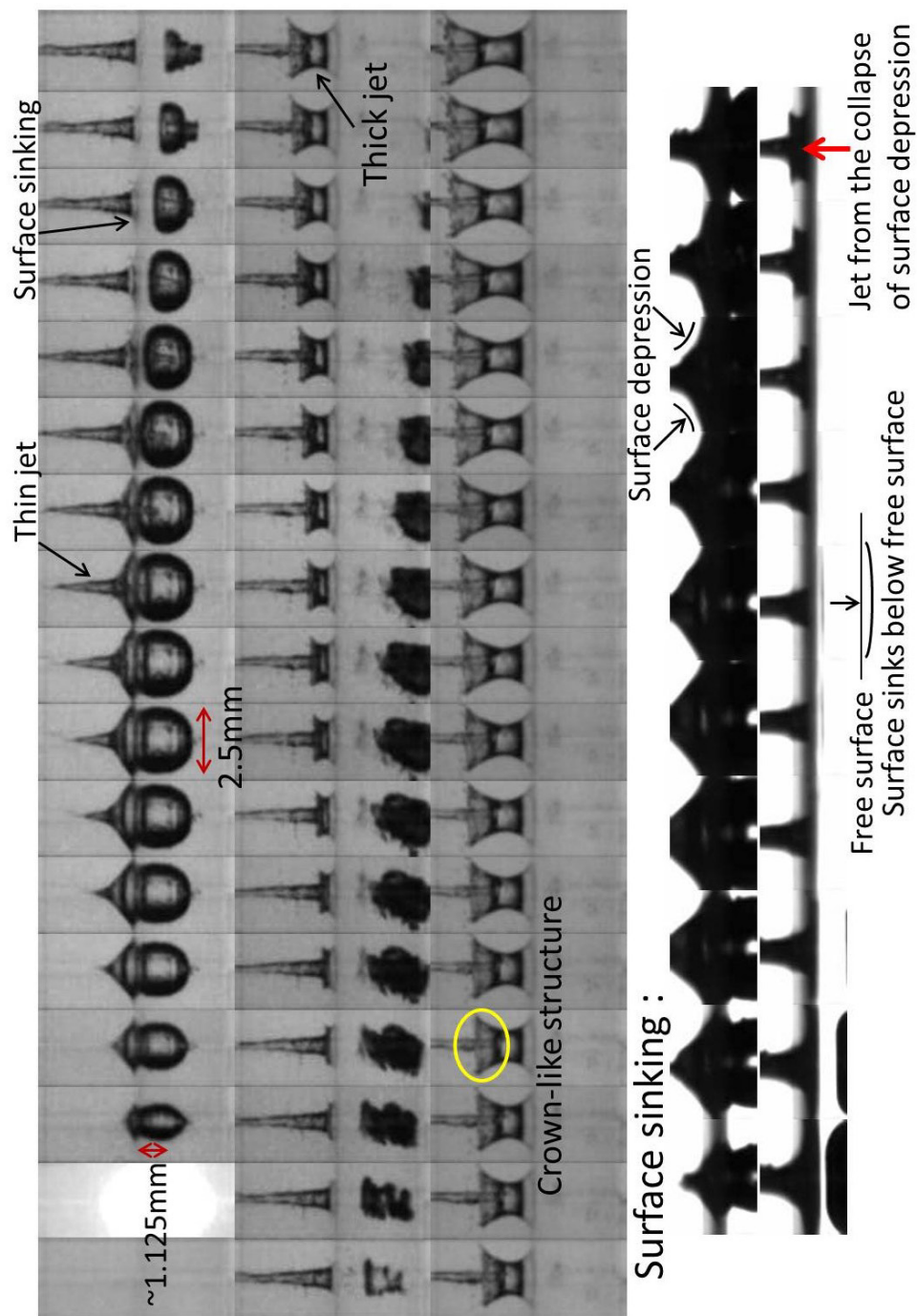


Fig. 3.4 A complete water jet is generated on a flat free surface with $\gamma = 0.8$. The frame rate is 80,000 fps. In the pictures of surface sinking, the exposure time is set to 1 μ s.

It should be noted that, before the formation of the thick jet, the thin jet has already formed on the sinking surface. This is in contrast to the general cases of surface depression in which only a crater (without the thin jet) appears on the free surface by inserting an external force [6-8] or a burst cavity just below the surface [9]. To help see the detailed surface curvature of the surface depression with a thin jet, we have applied the boundary integral method assuming a pressure $p = p_c + p_0(V_0/V)^{1.4}$ for a bubble in an inviscid, incompressible, and irrotational fluid domain, where p_c is a constant vapor pressure, V is the volume of bubble, and 1.4 the ratio of specific heats. Detailed numerical procedures of boundary integral method can be obtained from Appendix B and Refs. 2 and 3. Figure 3.5 shows the simulated dynamics of the bubble and free surface, along with the detailed schematic curvature of the surface depression with the thin jet. In fluid systems, a surface depression usually causes a singularity or near singularity of certain physical observables such as the divergences of velocity, surface curvatures, or pressure gradients at the minimum depth or pinch-off point [6]. The collapse of a surface singularity or near singularity leads to a jet formation. As shown in Fig. 3.5, the cross-sectional schematic image shows three singularities or near singularities as denoted by three solid dots. The central dot, obtained by linearly extrapolating the symmetric curves of the free surface without the thin jet, results in a thick jet as previously observed in collapsing depression [5]. The surface connected from the crater to the thin jet contributes to a curvature change which can induce two off-axis jets during the collapse of surface depression as indicated by the two arrows in Fig. 3.5. From the top view of the surface depression, this curvature change encircles around the thin jet, as shown in Fig. 3.6, and is called circular ring-shaped crater in the following discussions. It is the radially outward motion of the collapsing circular ring-shaped crater that results in the crown-like structure in Fig. 3.4.

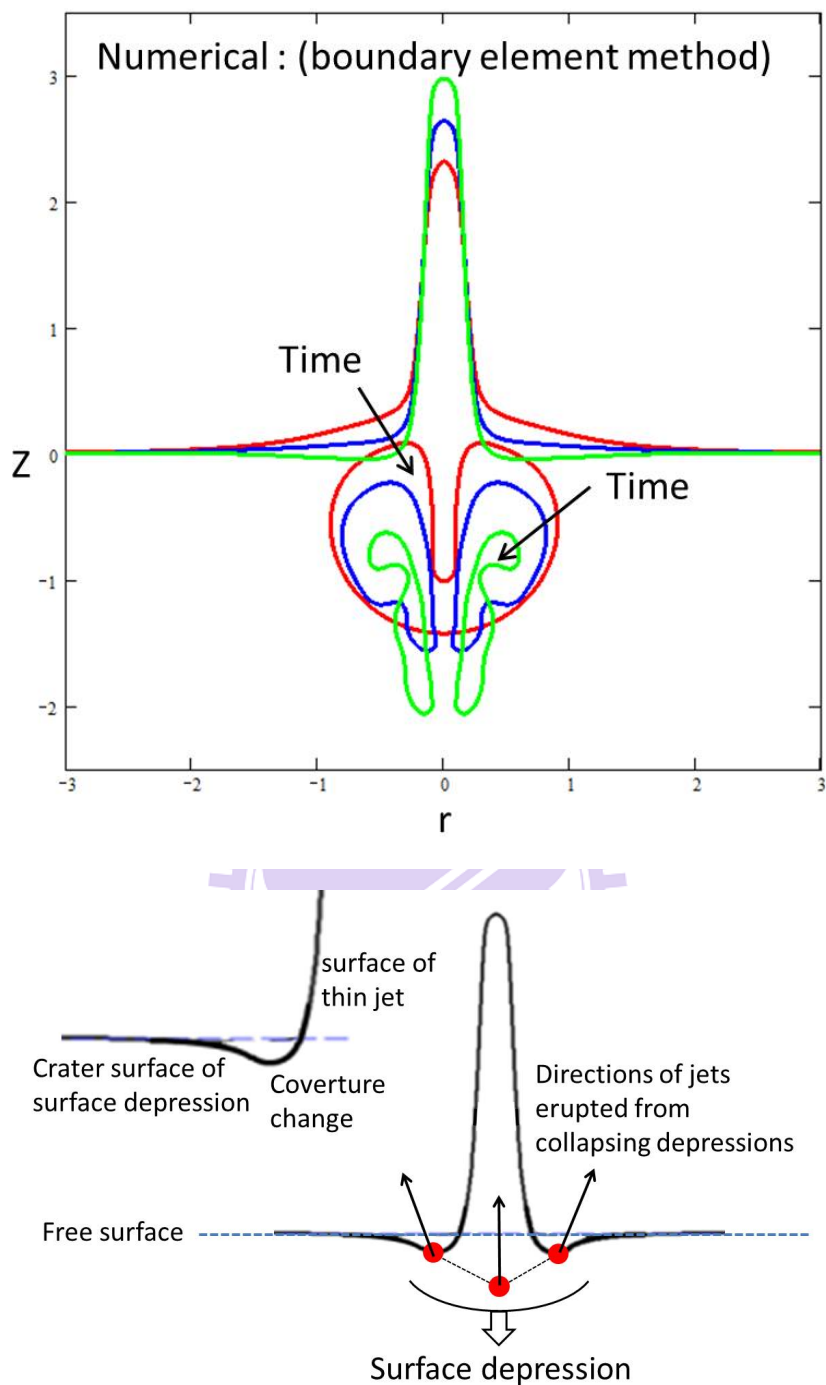


Fig. 3.5 The numerical simulation and curvature schematic of the surface depression are shown. The z and r of cylindrical coordinate are normalized to the R_{\max} of the bubble.

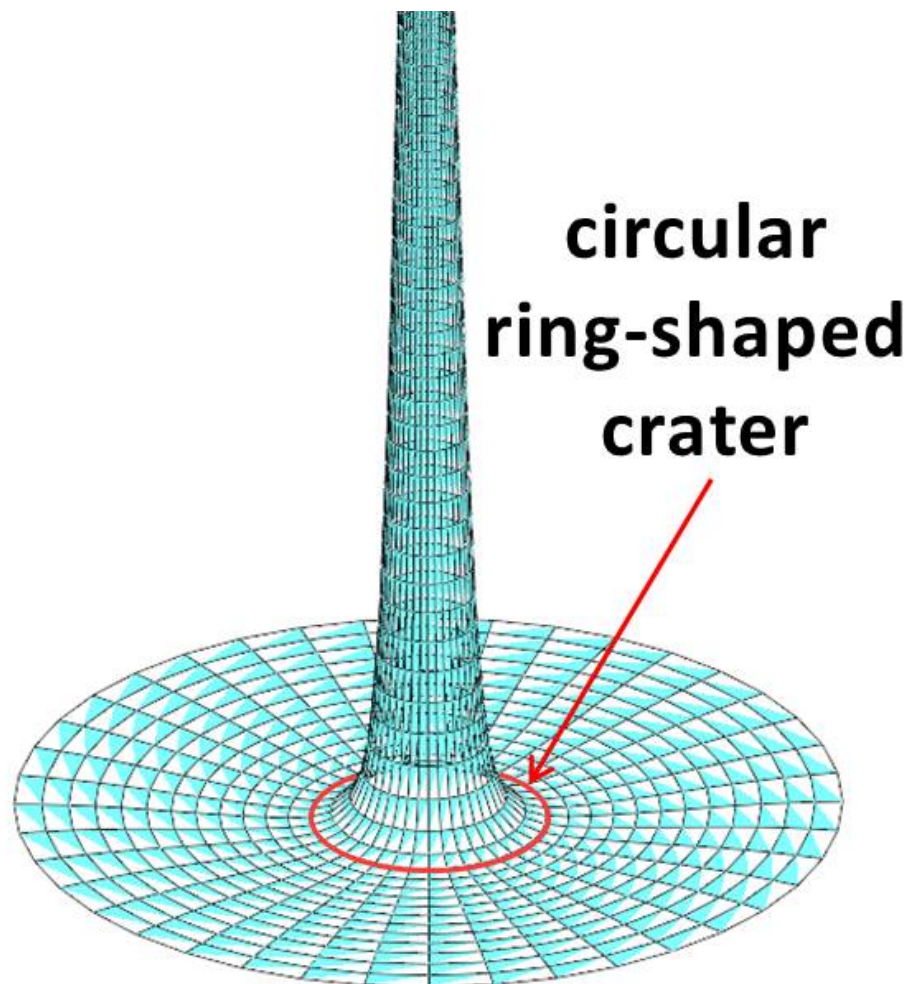
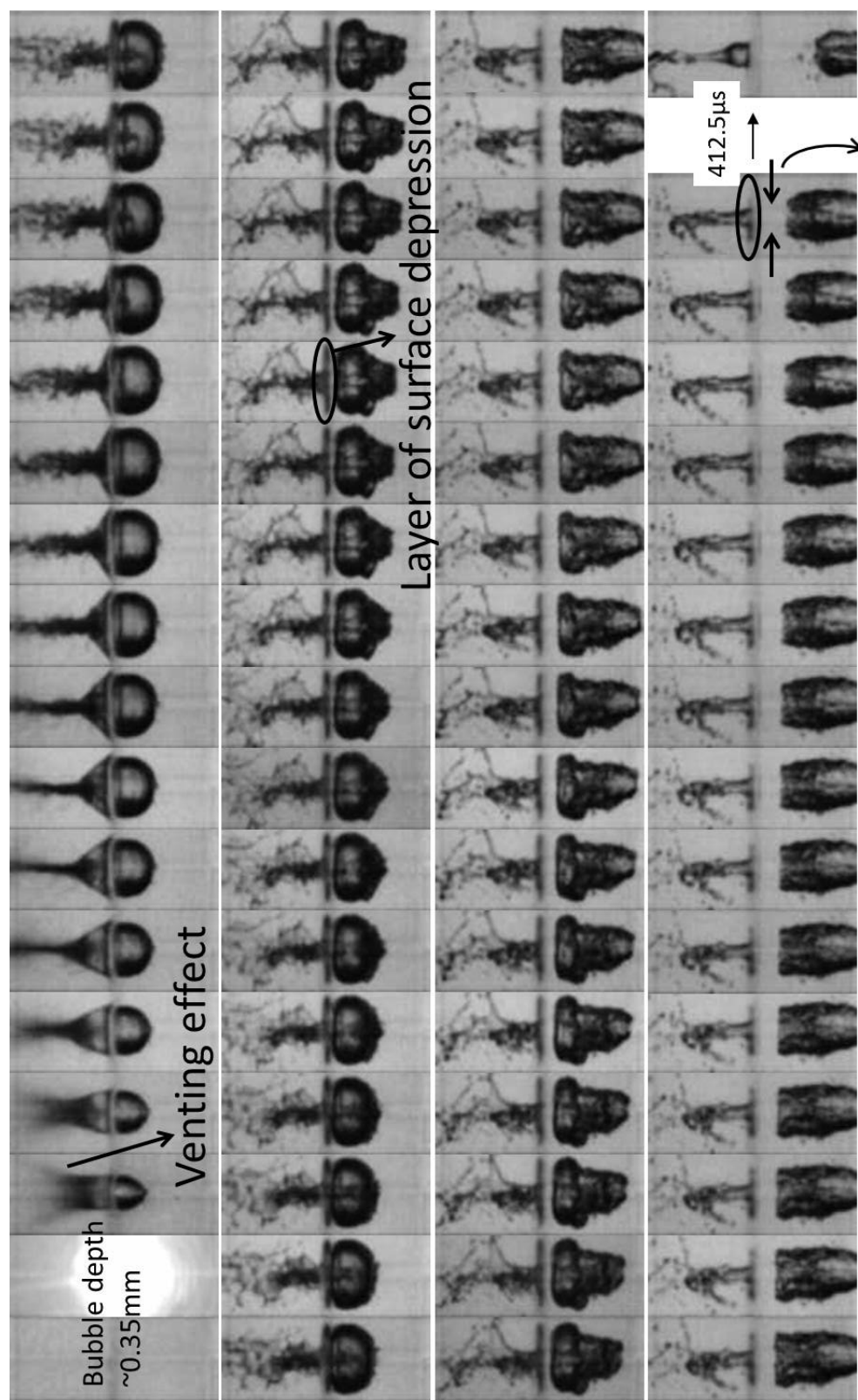
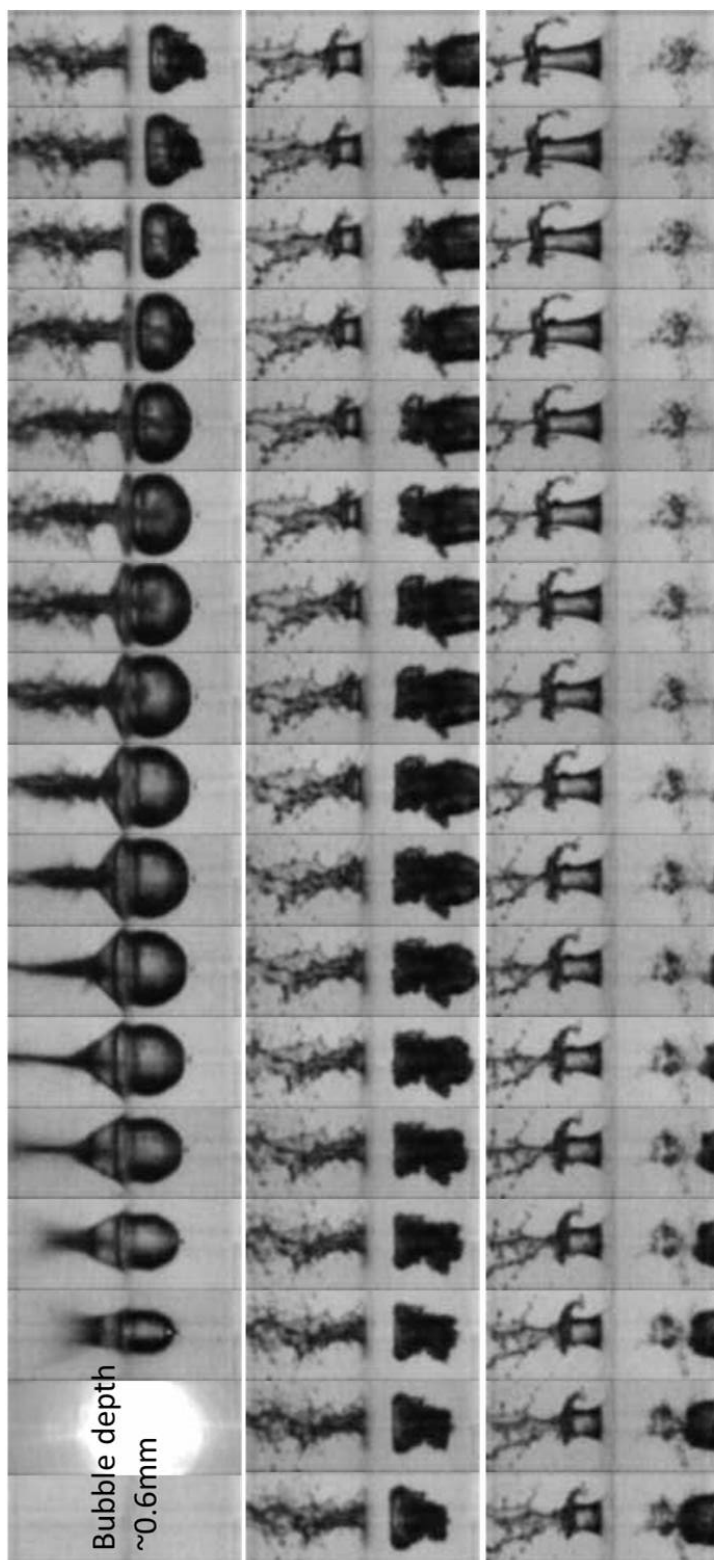


Fig. 3.6 A surface schematic of the circular ring-shaped crater is shown, which is generated around the thin jet during the surface depression induced by the downward collapse bubble.

When the bubble is very near the free surface for $\gamma = 0.28$, as shown in Fig. 3.7(a), the surface depression can be clearly seen with a segment of black line (layer of surface depression) generated on the horizontal free surface after the sinking around the bottom of the thin jet. The black line symmetrically shrinks toward the center axis from its opposite ends, and finally a thick jet forms under the thin jet, as depicted in the last picture in Fig. 3.7(a). The slow depression and collapse of the surface sinking are due to the extremely slow collapse of the bubble. The strong interaction between the upper boundary of the bubble and the free surface during the first expansion phase leads to some energy loss from the bubble similar as a venting effect mentioned in Ref. 10. Such an evolution about this venting effect was described more detail in the studies of laser ablation on a surface [11,12]. This venting effect could explain the unusual slowdown of the collapse of the bubble. Besides the slow collapse, the upper boundary of the bubble is so close to the free surface that it obstructs the downward depression of the surface sinking. Thus, the depression of the surface is not strong enough for the crown-like formation despite the appearance of the thin and thick jets. When $\gamma = 0.48$, the venting effect is diminished and the strength of the surface depression is restored to a level as the case of $\gamma = 0.8$ (near velocity of the thick jet). However, the thin jet experiences a violent disruption when going through the breach of the free surface by the expansion of the bubble at an initial time. The scraggly surface on the thin jet will disrupt the circular ring-shaped crater, and the crown-like structure is weak and unstable, as shown in Fig. 3.7(b). When $\gamma > 1.1$, the weak interaction between the free surface and the bubble leads to a diminished thin jet shaped like a small hill and weak surface depression. Such a surface depression is not large enough to cause the circular ring-shaped crater to reach the threshold of surface topology change [6] to induce the crown-like formation.



For caption see p. 67.



(b) $\gamma = 0.48$

For caption see p. 67.

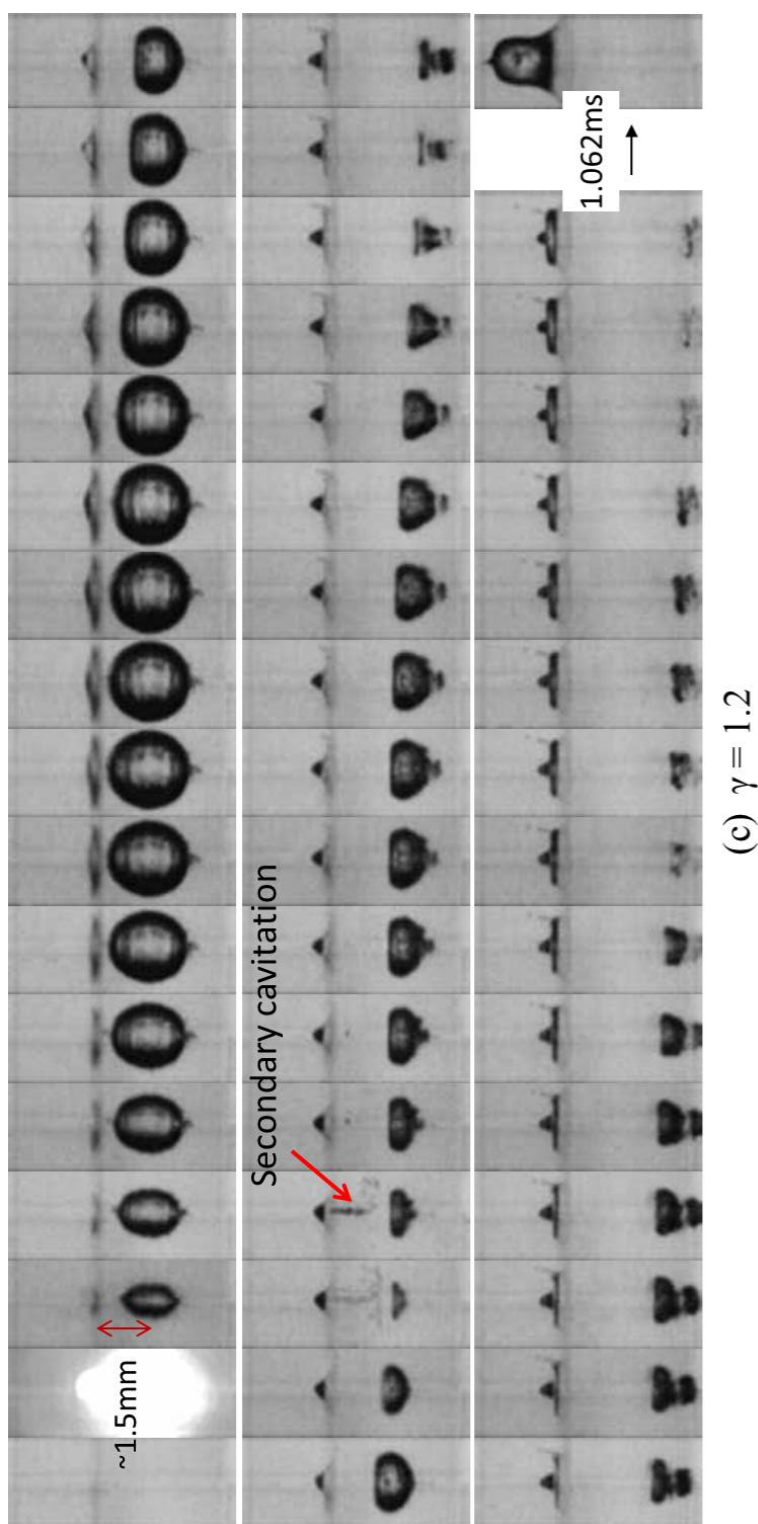
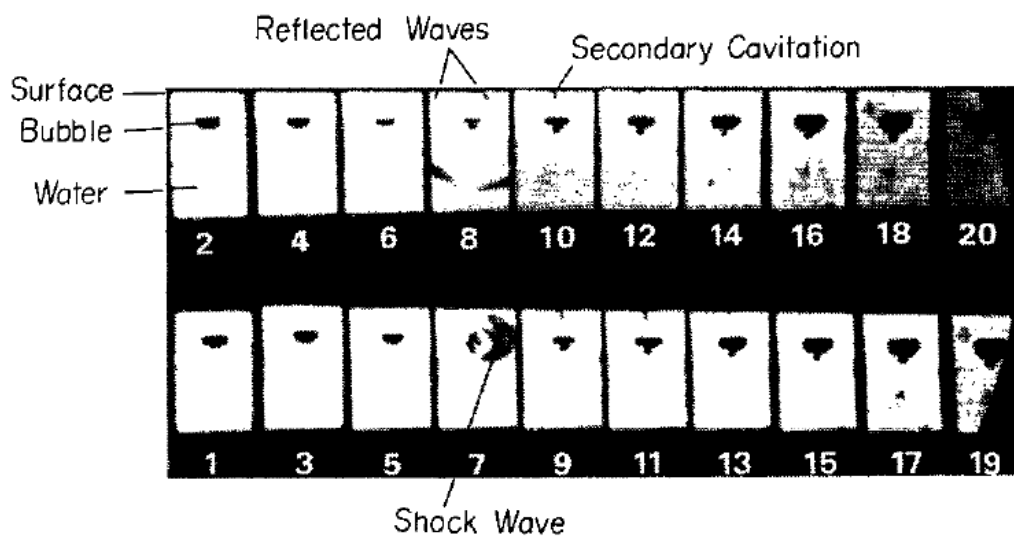
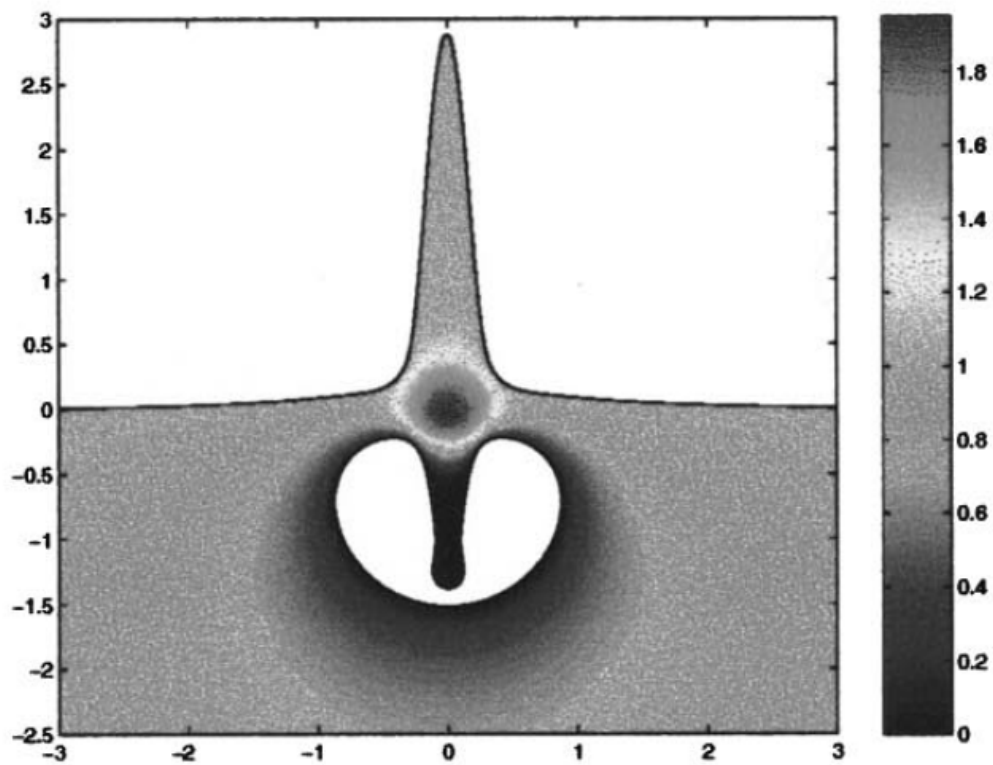


Fig. 3.7. The frame rate is 80,000 fps as same as Fig. 3.4. Figures 3.7(a) and (c) illustrate the non-crown formation when γ -value is smaller than 1.1, respectively. Figure 3.7(b) shows another structure of the crown formation as compared to Fig. 3.4. This crown is denoted as unstable crown formation.

In the second row of Fig. 3.7(c), we can see a vertical filament generated between the small hill on the free surface and the bubble, which is called secondary cavitation. This mechanism is discussed in the work by Tomita *et al.* [13] as follows. When the bubble collapse to a very small volume, the pressure inside the bubble is increased, which can be several MPa depended on the minimum volume of the bubble at the collapse points. Due to the ultrahigh pressure, the bubble will release a shock wave, and this shock wave will be reflected by the free surface which is similar to a concave mirror, as shown in Fig. 3.8(a) (the Fig. 5 of the Ref [13]). Then, the reflected shock wave will focus on the central axis below the free surface, resulting a negative pressure which can induce a water cavitation for generating the vertical filament. An important study about the region with negative pressure was pointed by Blake *et al.* [14] and Robinson *et al.* [3] from the theoretical simulation which shows a zero pressure region is formed during the first collapse of the bubble below the free surface, as shown in Fig. 3.8(b) (the Fig. 4(g) of the Ref [3]). Because the bubble is also generated by laser-induced “cavitation”, the cavitation generated by the reflected shock wave is called secondary cavitation. Additionally, in our experimental results, this secondary cavitation usually occurs when the bubble depth $\gamma > 1$. We consider that this reason is due to the minimum volume of the bubble at the first collapse. Figure 3.7 shows that the volume of the bubble at the first collapse is smaller when the bubble depth is increased. As a result, the shock wave emitted from the bubble is increased when the bubble depth is increased for inducing the secondary cavitation.



(a)



(b)

Fig. 3.8 (a) The Schlieren photograph about the interaction between the shock wave emitted from the bubble and the free surface [13, Fig. 5]. (b) A zero pressure region is formed between the bubble and the bottom of the thin jet [3, Fig. 4(g)].

To see the evolution of bubble depth, Figs. 3.4 and 3.7 illustrate the morphologies of water jet for each γ -value of the above-mentioned four γ ranges. Detailed correlation between the thin jet and crown-like structure is shown in Fig. 3.9 with increasing γ from 0.5 to 1.02. For $\gamma = 0.5$, the morphologies show the splash of water from the breached surface into multiple droplets. It is difficult to distinguish the shape of the thin jet from the upward splash. This defective structure of the thin jet results in an unstable crown, similarly as shown in Fig. 3.7(b). Increasing γ can reduce the influence of the water splash on the thin jet which begins to show a continuous line structure, as implied in the fourth frame of Fig. 3.9 for $\gamma = 0.58$. The crown-like jet is still unstable, and thus the circular ring-shaped crater resulted from the surface depression should be still defective. When $\gamma \geq 0.6$, the splash is depressed and the crown structure becomes clear. When $\gamma = 0.7$, breached surface is absent and a pronounced growth of crown-like structure can be seen. The velocities of both the thin and thick jets decrease with increasing γ from 0.7 to 1.02 due to the depression of the surface interaction, and the height of the crown wall thus gradually decreases, and eventually disappears, as shown in Fig. 3.7(c). Figure 3.9 reveals that crown-like structure is always accompanied with a thin jet and becomes mature in structure when the thin jet is stabilized.

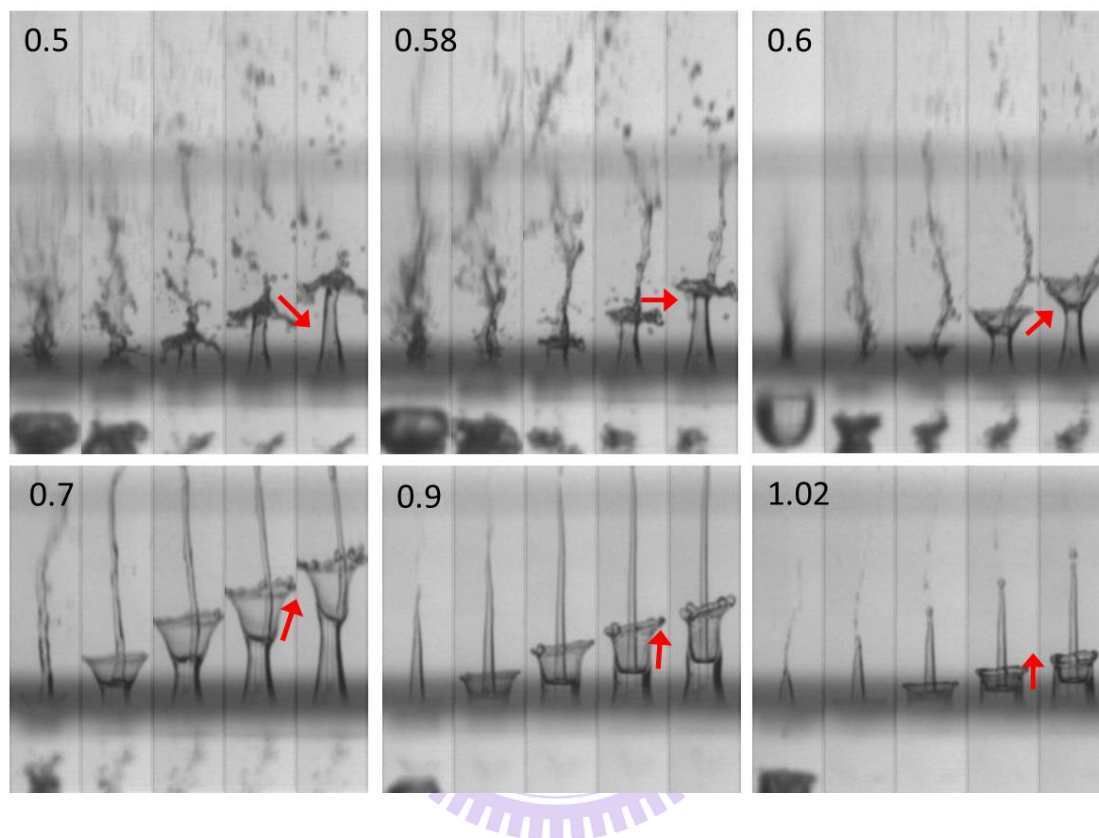


Fig. 3.9 The structures of the thin jets and crowns with different γ -values which are labeled on the left top of each image. The frame rate is 30,000 fps but the time interval between each frame is 0.166 ms. The arrow shows the orientation of the crown wall, which rotates counterclockwise to vertical direction when γ is increased from 0.5 to 1.02.

We have shown by Fig. 3.4 that the crown-like structure forms around the thick jet, which suggests a correlation between the crown formation and the origin of the thick jet. This correlation can be further confirmed by Fig. 3.9 in which, despite different orientations (defined by the arrows in Fig. 3.9) of the crown wall, the bottom of the crown-like structure always sits on the head of the thick jet. The orientation of the crown wall can be seen to gradually turn counterclockwise to vertical when γ is gradually increased from 0.5 to 1.02. The transition to a complete crown wall occurs when the arrow turns from downward ($\gamma = 0.5$) across the horizontal line ($\gamma = 0.58$) to upward (γ from 0.6 to 1.02). This feature shows a high regularity and correlation between the orientation of the crown wall and the depth of the bubble. For comparison, let us refer to Fig. 3.5 which shows the relation between the deformed surface depression (with the thin jet) and arrowed directions of the collapse of the circular ring-shaped crater. Based on Fig. 3.5, it is reasonable to infer that the directions of the circular ring-shaped crater should have a similar trend of rotation when the bubble depth is increased to change the surface depression. This comparability further suggests the crown-like formation is correlated to the surface depression with the thin jet (to induce the circular ring-shaped crater). From the continuous change of the orientation of the crown with increasing γ , the layer of water on top of the thick jet for $0.5 \leq \gamma \leq 0.6$ should be considered as a crown-like structure similar to that for $\gamma \geq 0.6$, and thus was denoted as “unstable crown formation” in the above discussions. Finally, as shown in Fig. 3.9, the top rim of the crown wall is nearly flat for $0.6 \leq \gamma \leq 1.02$, which is significantly different to the two-arm splash on the crown wall induced by spark discharge [10]. This difference is probably related to the unavoidable mechanical influence due to the electrodes in spark discharge.

3.2.2 Temporal evolution of laser-induced water jet

The time evolution of a water jet generated by a nanosecond laser induced water breakdown is presented with different depths beneath a flat free surface. Figure 3.10 shows a typical experimental result for the morphological variations in the temporal evolution of the water jet generated by laser-induced breakdown at a depth of $\gamma = 0.9$. The crown-shaped structure can be seen to be a nearly circular cup. This cylindrical symmetry is quite different from the structure of two-arm splash induced by a spark bubble [10]. The cylindrical symmetry leads to the net force on the wall of the crown-shaped water jet to be uniform in the radial direction. The surface tension of the crown-shaped water jet tends to decrease the surface area by shrinking the diameter of the crown structure. As seen in the fourth row of Fig. 3.10, the crown-shaped water jet is getting closed by over time and forms an air bubble to surround the prior thin jet. The closing motion of the crown-shaped water jet can be analogously imaged as the process of a flower closing the petals. Note that the flat free surface is important for generating the cylindrically crown-shaped water jet with closing motion because the curvature of free surface critically determines the structure of the water jet. In the earlier investigations, it has been found that a cylindrical free surface generally leads to the structure of the two-arm splash with only opening motion [15,16], whereas a spherical surface usually cannot results in the generation of the cup-shaped splash [15]. Just after the closing motion, the top rim of the cup-shaped jet pinches the prior thin jet into two segments to form an air bubble with a vertically elongated toroidal shape. In other words, the circular wall of the crown-shaped jet turns into the boundary of the air bubble and the enclosing segment of the prior thin jet develops into the central pillar of the toroidal air bubble. Followed closely by, the elongated shape of the toroidal air bubble starts to become a near

spherical shape owing to the surface tension to shrink the surface area. During the shrinking of the air bubble, the central pillar of the toroidal air bubble breaks into multiple water drops inside the air bubble, as shown in the last row of Fig. 3.10. The breakup into smaller packets from a stream of fluid, referred to as Plateau–Rayleigh instability [17,18], is rich with varieties of phenomena and applications [19]. A well-known example related to Plateau–Rayleigh instability is the formation of small droplets when water is dripping from a faucet. The last row of Fig. 3.10 also depicts that the enclosed drops oscillate, collide and recombine to each other; finally only a drop of water with a diameter about 0.33 mm survives in the spherical air bubble. Interestingly, the final water drop keeps moving upward and bounces between the top and bottom walls of the air bubble. Eventually, the water drop stays on the bottom wall of the air bubble and is stably dragged up by the air bubble, as shown in the last picture of Fig. 3.10. The comprehensive evolution of the water jet can be seen from the Supplemental Material [20] for the movie corresponding to Fig. 3.10.

The morphological variations of the water jet in the temporal evolution are significantly dependent on the depth of the cavitation bubble. The scenario shown in Fig. 3.10 for displaying an air bubble enclosing a water drop generally occurs for the depth in the range of $0.8 \leq \gamma \leq 1.03$. There are another two types of morphological changes of the water jets generated in the depths of $0.6 < \gamma < 0.8$ and $1.03 < \gamma < 1.1$, respectively. Figure 3.11 shows a typical result for the morphological variations in the temporal evolution of the water jet generated at a depth of $\gamma = 0.7$. In the early stages, the volume of the crown-shaped water jet can be seen to grow considerably. One might naturally expect that a stretched air bubble could enclose the prior thin jet to display a similar phenomenon of the formation shown in Fig. 3.10. However, the thin

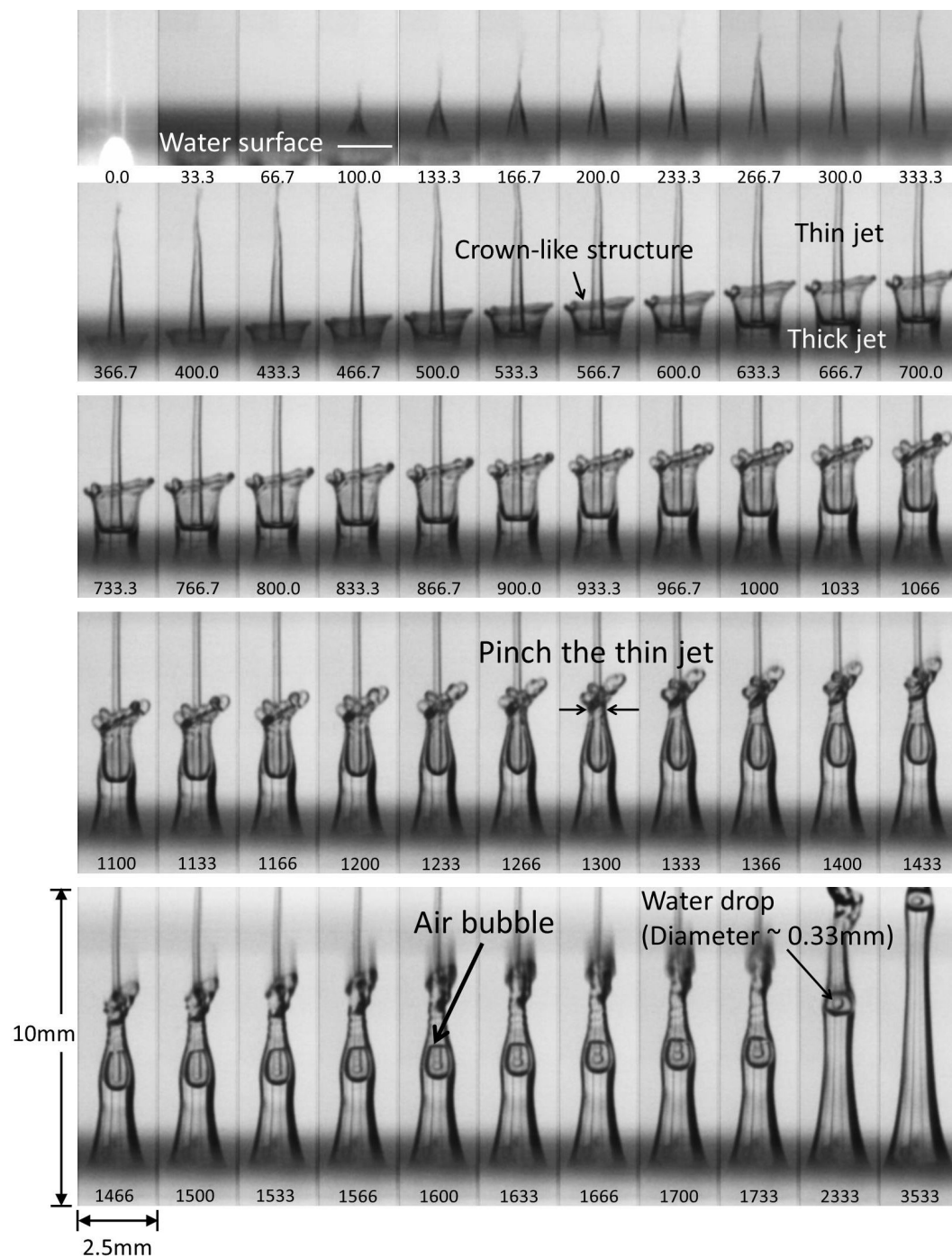


Fig. 3.10 A typical result for the experimental result for the morphological variations in the temporal evolution of the water jet generated by laser-induced breakdown at a depth of $\gamma = 0.9$. The time (in μs) is indicated at the bottom of each frame.

jet is usually bending owing to the strong interaction between the cavitation bubble and the free flat surface. The bent thin jet generally inclines to the sidewall of the crown-shaped jet. As a consequence, only an air bubble without any water drop can be formed in the final stages. The comprehensive evolution can be seen from the Supplemental Material [21] for the movie corresponding to Fig. 3.11. On the other hand, for the depth in the range of $1.03 < \gamma < 1.1$, the wall of the crown-shaped water jet is not high enough to enclose the thin jet with sufficient volume to form a water drop inside the air bubble. Figure 3.12 shows a typical result for the morphological variations of the water jet generated by the laser-induced water breakdown at a depth of $\gamma = 1.04$. The comprehensive evolution can be seen from the Supplemental Material [22] for the movie corresponding to Fig. 3.12.

Based on thorough experimental observations, the dependence of the pinched altitude H of the crown-shaped water jet on the depth parameter γ in the range of 0.6-1.1 is shown in Fig. 3.13. Note that there is no crown-shaped water jet to be generated for $\gamma < 0.6$ or $\gamma > 1.1$. It can be seen that the highest pinched altitude occurs near the region of $\gamma = 0.8$ and its value is approximately 2.3 mm. The decrease of the pinched altitude H for the depth in the range of $0.8 < \gamma < 1.1$ arises from the reduction of the interaction between the cavitation bubble and the free flat surface. The scopes for the three types of morphological variations of the water jet in the temporal evolution are depicted in Fig. 3.13. In brief, the condition for the formation of an air bubble enclosing a water drop is a straight thin jet with a sufficient pinched altitude for the crown-shaped water jet.

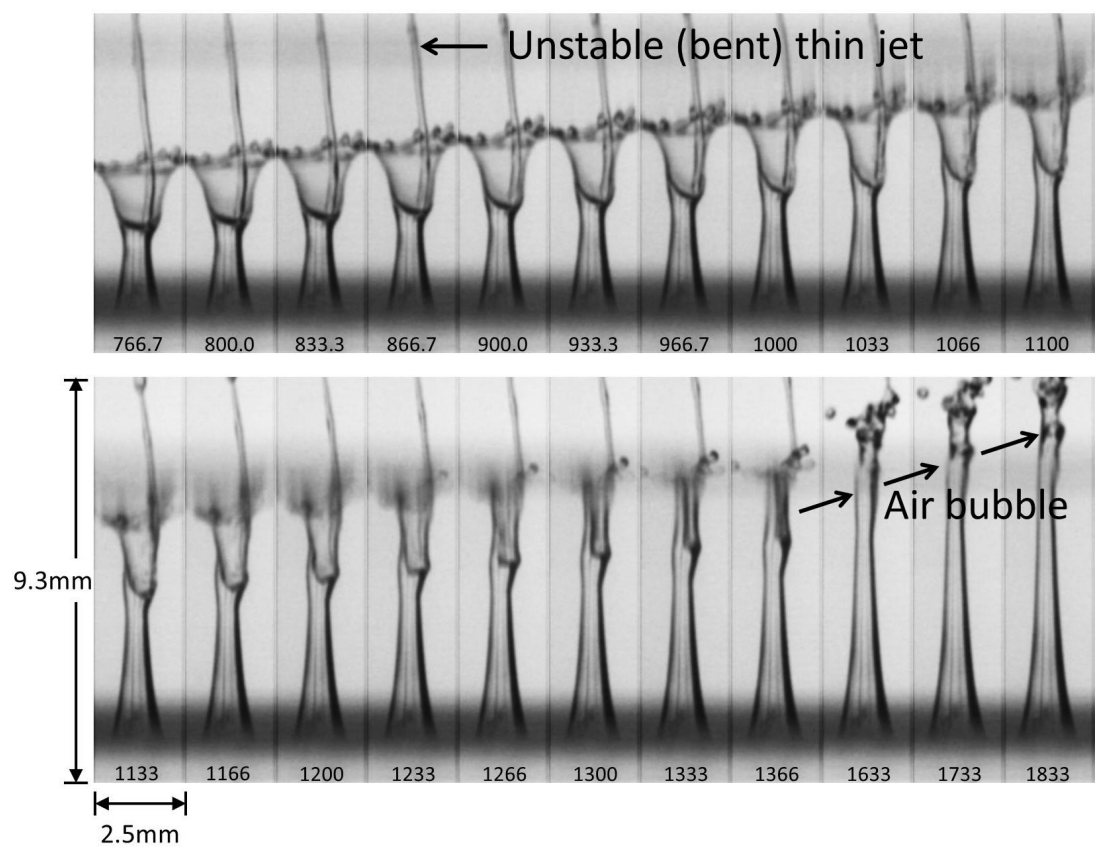


Fig. 3.11 A typical result for the morphological variations in the temporal evolution of the water jet generated at a depth of $\gamma = 0.7$. The time (in μs) is indicated at the bottom of each frame.

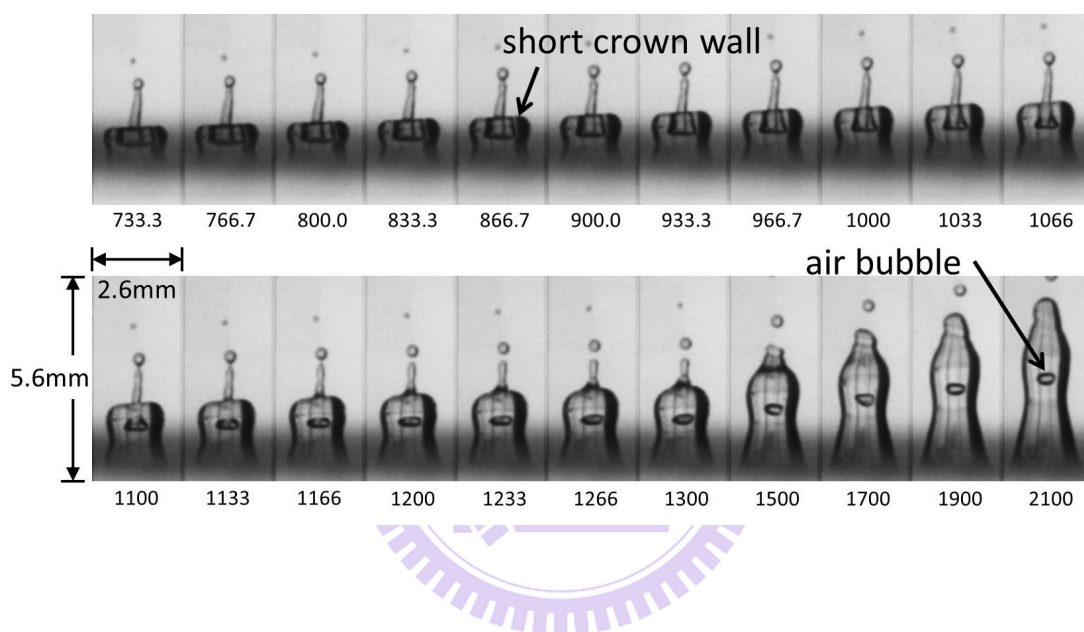


Fig. 3.12 A typical result for the morphological variations in the temporal evolution of the water jet generated at a depth of $\gamma = 1.04$. The time (in μs) is indicated at the bottom of each frame.

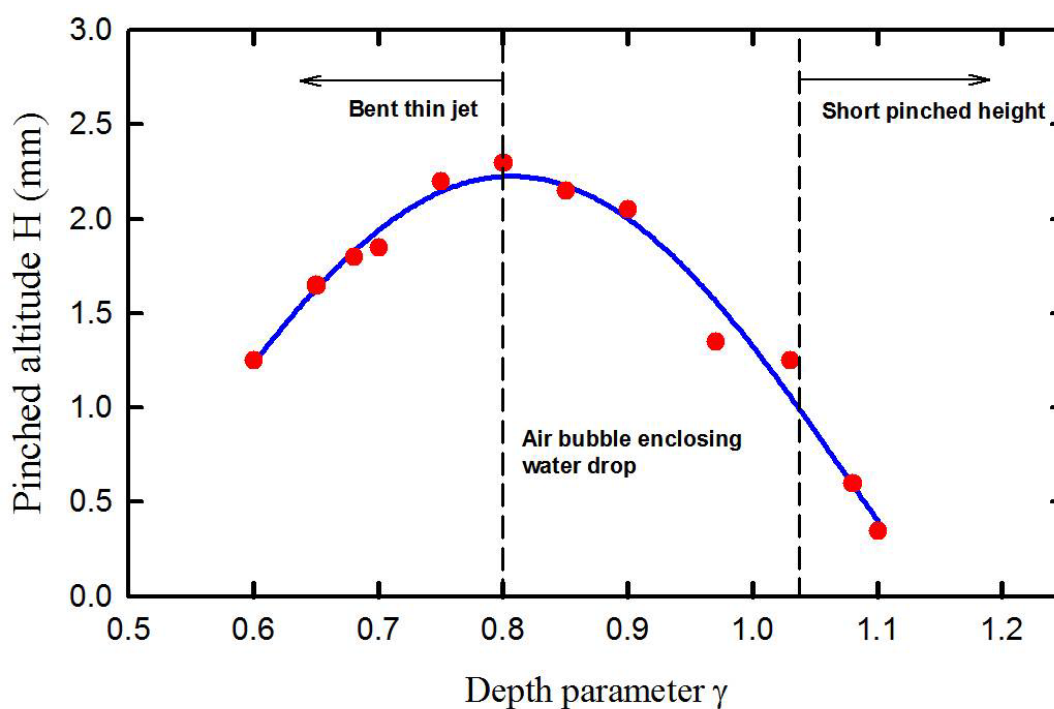


Fig. 3.13 Dependence of the pinched altitude H of the crown-shaped water jet on the depth parameter γ in the range of 0.6-1.1.

Reference

- [1] G. L. Chahine, “Interaction between an oscillating bubble and a free Surface,” *J. Fluids Eng.* **99**(4), 709–716 (1977).
- [2] A. Pearson, E. Cox, J. R. Blake, and S. R. Otto, “Bubble interactions near a free surface,” *Eng. Anal. Bound. Elem.* **28**(4), 295–313 (2004).
- [3] P. B. Robinson, J. R. Blake, T. Kodama, A. Shima, and Y. Tomita, “Interaction of cavitation bubbles with a free surface,” *J. Appl. Phys.* **89**(12), 8225–8237 (2001).
- [4] B. R. Ringeisen, B. J. Spargo, and P. K. Wu, *Cell and Organ Printing* (Springer, 2010).
- [5] M. Duocastella, A. Patrascioiu, J. M. Fernández-Pradas, J. L. Morenza, and P. Serra, “Film-free laser forward printing of transparent and weakly absorbing liquids,” *Opt. Express* **18**(21), 21815–21825 (2010).
- [6] B. W. Zeff, B. Kleber, J. Fineberg, and D. P. Lathrop, “Singularity dynamics in curvature collapse and jet eruption on a fluid surface,” *Nature* **403**(6768), 401–404 (2000).
- [7] A. M. Worthington and R. S. Cole, “Impact with a liquid surface, studied by the aid of instantaneous photography,” *Phil. Trans. Roy. Soc.* **189**, 137–148 (1897).
- [8] S. T. Thoroddsen and A. Q. Shen, “Granular jets,” *Phys. Fluids* **13**(1), 4–6 (2001).
- [9] J. M. Boulton-Stone and J. R. Blake, “Gas Bubble bursting at a free surface,” *J. Fluid Mech.* **254**(-1), 437–466 (1993).
- [10] A. Pain, B. H. T. Goh, E. Klaseboer, S. W. Ohl, and B. C. Khoo, “Jets in quiescent bubbles caused by a nearby oscillating bubble,” *J. Appl. Phys.* **111**(5), 054912 (2012).
- [11] I. Aplitz and A. Vogel, “Material ejection in nanosecond Er:YAG laser ablation of

- water, liver, and skin,” Appl. Phys., A Mater. Sci. Process. **81**(2), 329–338 (2005).
- [12] S. T. Thoroddsen, K. Takehara, T. G. Etoh, and C. D. Ohl, “Spray and microjets produced by focusing a laser pulse into a hemispherical drop,” Phys. Fluids **21**(11), 112101 (2009).
- [13] Y. Tomita, T. Kodama, and A. Shima, “Secondary cavitation due to interaction of a collapsing bubble with a rising free surface,” Appl. Phys. Lett. **59**, 274-276 (1991).
- [14] J. R. Blake, B. B. Taib, and G. Doherty, “Transient cavities near boundaries Part 2. Free surface,” J. Fluid Mech. **181**, 197-212 (1987).
- [15] D. Obreschkow, P. Kobel, N. Dorsaz, A. de Bosset, C. Nicollier, and M. Farhat, “Cavitation Bubble Dynamics inside Liquid Drops in Microgravity,” Phys. Rev. Lett. **97**, 094502 (2006).
- [16] E. Robert, J. Lettry, M. Farhat, P. A. Monkewitz, and F. Avellan, “Cavitation bubble behavior inside a liquid jet,” Phys. Fluids **19**, 067106 (2007).
- [17] J. A. F. Plateau, *Statique expérimentale et théorique des liquides soumis aux seules forces moléculaires* (Gauthier-Villard, Paris, 1873).
- [18] L. Rayleigh, “On the Capillary Phenomena of Jets,” Proc. R. Soc. London **29**, 71-97 (1879).
- [19] J. Eggers and E. Villermaux, “Physics of liquid jets,” Rep. Prog. Phys. **71**, 036601 (2008).
- [20] <http://dpss.servehttp.com/> → Publications → Graduation Thesis: the movie 1 of the attachment of this graduation thesis corresponding to the results shown in Fig. 3.10.
- [21] <http://dpss.servehttp.com/> → Publications → Graduation Thesis: the movie 2 of

the attachment of this graduation thesis corresponding to the results shown in Fig. 3.11.

[22] <http://dpss.servehttp.com/> → Publications → Graduation Thesis: the movie 3 of the attachment of this graduation thesis corresponding to the results shown in Fig. 3.12.



Chapter 4. Laser-induced breakdown beneath a flat water surface – Parallel focusing

In Liquid jet formation, several structures of liquid jet were discussed for the mechanisms of formation and breakup such as sheets, jets, and sprays [1]. Compared to a cylinder jet and a spray, sheet liquid jet can be implemented by two liquid jets in a head-to-head coaxial impact or at certain angle. Such collision results in a circular plate or thin leaf-shaped of liquid in the plane bisecting the angle between the two jets with droplet breakup around the rim of the sheet. In 2012, Badarinath Karri *et al.* [2] showed a sheet jet formation when a cavitation bubble generated beneath a hole in a plate placed at an air-water interface. The expansion and collapse of the bubble induce a primary slow jet and following high speed jet, respectively. Then, the faster jet catches up with the primary one and coaxially impacts with the primary one, resulting in the sheet plane of liquid perpendicular to their axis. In this section, we show a sheet water jet induced by a nanosecond laser in which the formation and feature of the sheet structure is unlike the general sheet jet such as an impact of a jet on a solid surface [3] or collision between two liquid jets [4].

4.1 Laser-induced elongated bubble in infinite surrounding

Based on the experimental setup in Chapter 3, in infinity surrounding, Fig. 4.1 shows the oscillation of an elongated bubble of about 1.4 mm in length induced by a nanosecond laser with 18 mJ. The frame interval is 10 μ s with 1 μ s exposure time. The major axis of the elongated bubble is on the horizontal line or the incident optical path because the laser-induced plasma expands mainly on the optical path. We can see the oscillations of the bubble on major and minor axes are similar during the first period of expansion, which leads to a nearly spherical shape with diameter about 2.5 mm at its maximum size. Additionally, because the elongated bubble is cylindrical symmetry, the expansions of the bubble on the directions normal to the major axis are equal to each other. As a result, the elongated bubble shows a near sphere at its maximum size during the first expansion in an infinite surrounding despite that this bubble is not initially spherical symmetry in shape and velocity. In Fig. 4.1, upon the first collapse point, the bubble uniquely rebounds to a dumbbell due to the significant expansion on the major axis. Following the dumbbell, the bubble converts to elliptic and reaches the second collapse point. After the second collapse point, the bubble vibrates and decays in roughly spherical shape. The experimental result of Fig. 4.1 is conspicuously different to the bubble oscillation induced by a femtosecond laser as shown in the Fig. 33 of Ref [5].

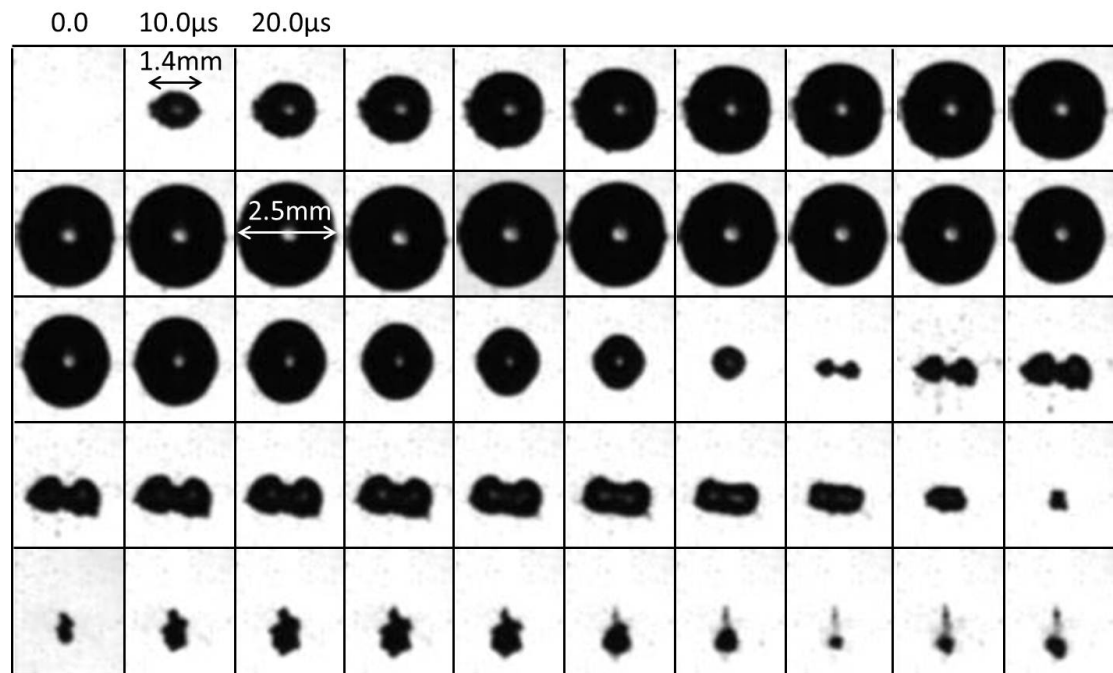


Fig. 4.1 The oscillation of an elongated bubble in infinite surrounding. The frame rate is 100,000 and the exposure time is 1 μ s.

4.2 Experimental setup

A bubble is generated beneath a free surface by focusing a flash-pump pulsed laser (Nd:YAG, $\lambda=1064$ nm) with a pulse width 6 ns. The beam waist of the laser is 1.5 mm and is enlarged 10 times to 15 mm by employing a beam expander (Fig. 4.2). Then, a lens with a focal length of 4.5 cm in air is used to focus the enlarged beam horizontally into a tap water at a room temperature 297K under atmospheric pressure. The dimension of the water tank is $100 \times 70 \times 20$ mm³ and the depth of water is 15 mm for alleviating the influence on the bubble from the bottom wall of the tank. The dynamic of the interaction between the bubble and the free surface is reproducible and is recorded by a high speed camera (NAC GX-3) which has maximum frame rate at 198,000 fps.

The plasma expansion in the early stage of a laser-induced breakdown is intimately correlated to the laser energy, and the plasma expands toward the incident laser beam due to the energy distribution on the incident optical path [6]. The higher the incident energy, the farther the initial plasma moves away from the focal point, which results a longer cavitation bubble. Furthermore, because the maximum size of the bubble gradually saturates when the laser energy is increased, the optimal stability in bubble size can be achieved at lager laser energy. As a result, for observing a stable water jet induced by an elongated bubble, the laser energy is set to 18 mJ which is the maximum laser energy measured just after the focusing lens with $f=4.5$ cm.

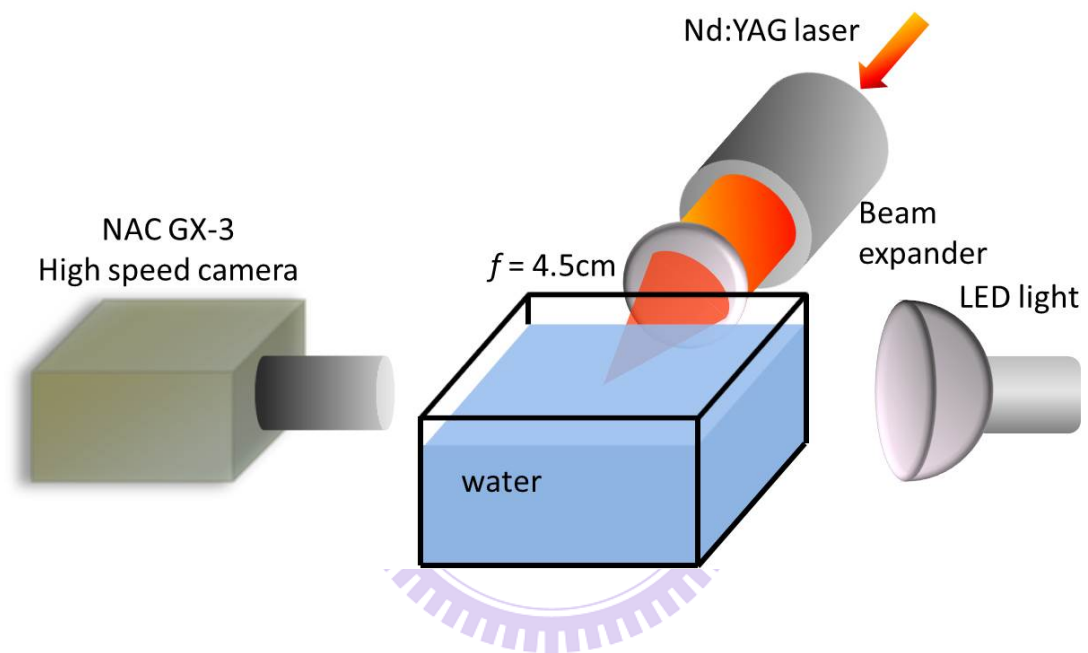


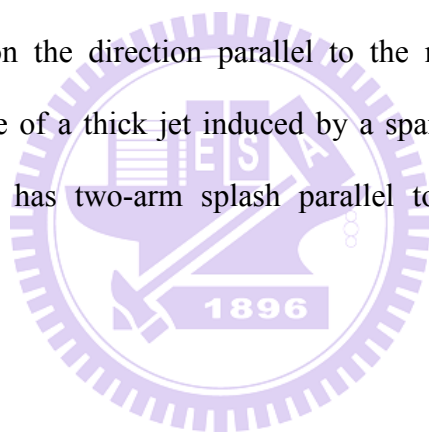
Fig. 4.2 The schematic experimental setup for observing the water jet on the free surface. Laser is horizontally focused into the water.

4.3 Results and discussion

The water jet shows a sheet feature and this sheet structure gradually appears on each part of the water jet when the bubble depth is decreasing. In this section, we follow the sequence of the appearing of each part of the water jet with decreasing bubble depth.

Figures 4.3 and 4.4 show the behavior of a water jet on a flat water surface with 30,000 frame rate and 10 μ s exposure time, which is induced by an elongated bubble with $\gamma = 1.18$ and 0.76. This water jet is divided into a thin jet and a thick jet as depicted in Fig. 4.3 for discussing the feature of the water jet. The bubble depth is defined in stand-off parameter $\gamma = D/R_{\max}$, where D is the depth beneath the free surface and R_{\max} is the maximum bubble radius. Because the vertical expansion of the bubble is significantly influenced by the free surface, the maximum bubble radius is measured by the width of bubble in the picture and is around 0.9 mm to 0.99 mm for bubble depth between 0.5 mm and 1.5 mm. As a result, the maximum bubble radius is defined in 0.95 mm. The direction of the laser beam goes horizontally from left to right, and the major axis of the elongated bubble is parallel to the water surface plane. In other words, the morphology of the water jet is not cylindrical symmetry. When the bubble gradually approaches to the water surface, this asymmetrical effect from the bubble first apparently appears on the top of the thick jet which has a pair of ear, as shown in the Fig. 4.3 with $\gamma = 1.18$. It should be noticed, this ear is parallel to the major axis of the bubble. This formation of the ear will be discussed later because the experimental results about this mechanism are clearer when the interaction between the bubble and free surface is increased by decreasing the bubble depth.

These ears significantly grow into a structure similar as a pair of opposite arm when the bubble gradually approaches to the water surface, as shown in Fig. 4.4 with $\gamma = 0.76$. In addition to the significant water splashes of the two arms, there is a short cyclic splash shaped like a cup connected between the two arms and the top of the thick jet, as shown by the last few pictures of the second row in Fig. 4.4. Comparing this experimental result with the case when the expansion of the bubble on the direction parallel to the free surface is symmetrical, for example, vertically focusing the laser beam into a water as measured in our previous work in which the two arms are not exist and the edge of a cup is uniform [7]. As a result, we consider that the structure consisted of the arms and the cup is an asymmetry crown-shaped water jet which has great speed on the direction parallel to the major axis of the bubble. Additionally, the structure of a thick jet induced by a spark bubble is similar to the case of Fig. 4.4, which has two-arm splash parallel to the electrodes of spark discharge [8,9].



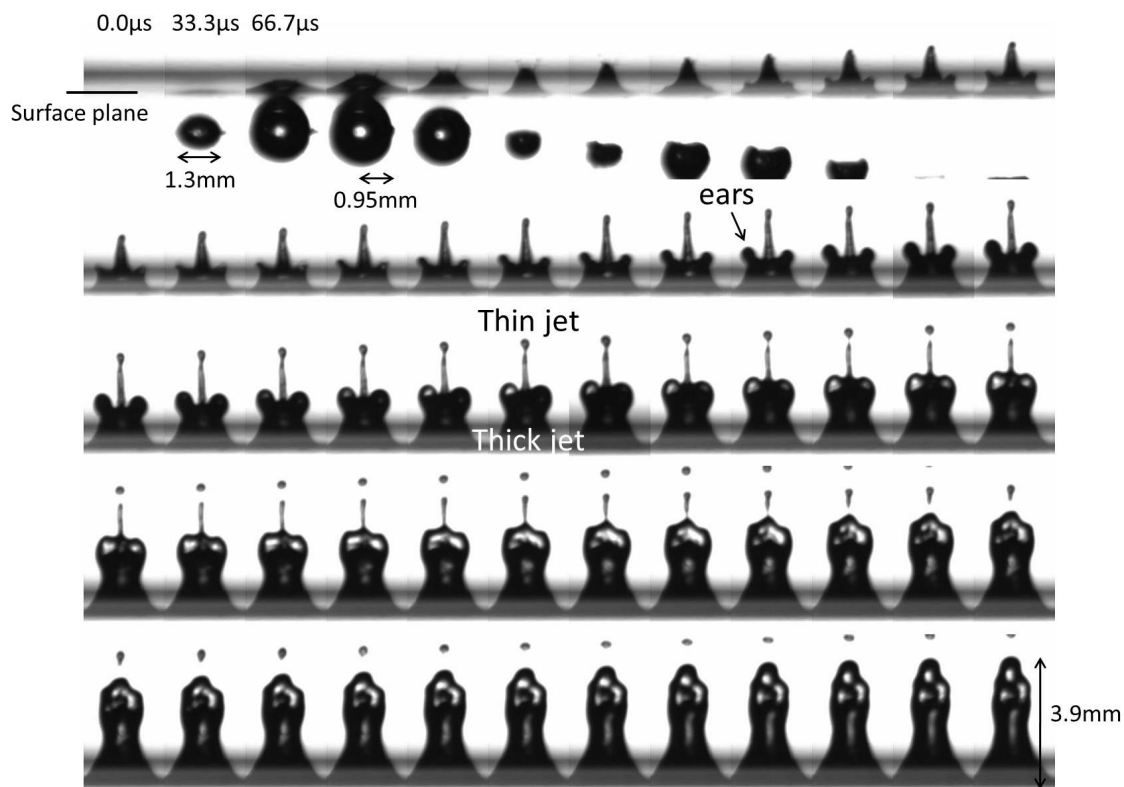


Fig. 4.3 The water jet for $\gamma = 1.18$. The major axis of the bubble is parallel to the water surface. The frame rate is 30,000 and the exposure time is 10 μ s.

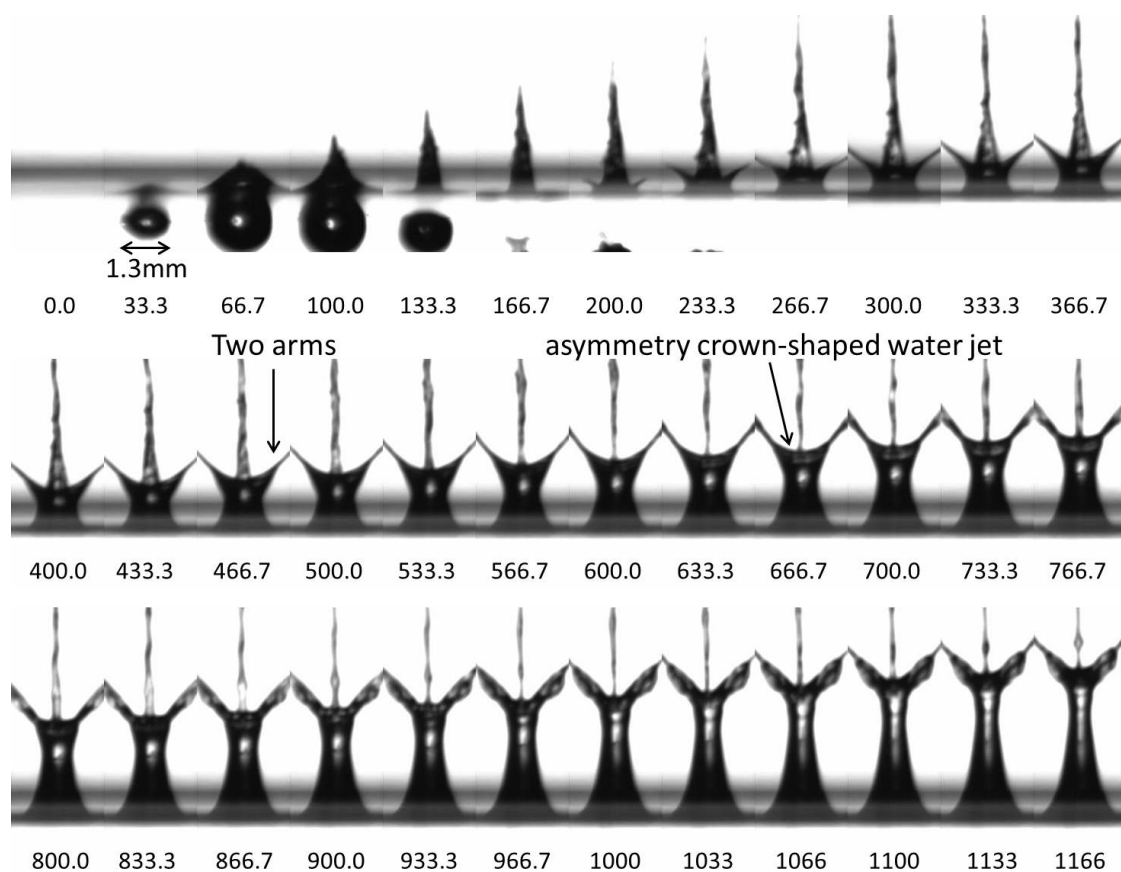


Fig. 4.4 The water jet for $\gamma = 0.76$. The time (in μs) is indicated at the bottom of each frame. The top of the thick jet shows an asymmetry crown-shape water jet.

Beside the growth of the ear to a two-arm splash, the thin jet appears an interesting feature which is analogously a rotating drill. As labeled by an arrow in Fig. 4.5(a) with $\gamma = 0.73$, the thin jet rotates in 180° with about 0.2 ms. Generally, a rotating jet could be generated artificially by a rotating pressurized chamber in which the jet is expelled tangentially [1]. However, in our experimental setup, there is no angular force for inducing the circular rotation from the bubble. Thus, we explain this rotating jet analogously by the mechanism of circular or elliptical polarization of an electromagnetic wave as followed. When a stream of fluid is generated, no matter how smooth the stream is, there always exists instability began from any tiny perturbation in the stream, referred to as Plateau-Rayleigh instability [10,11]. This instability causes a waving on the surface of the stream, and finally, this stream breaks into smaller droplets [1,10,11], as shown in Fig. 4.6. Figure 4.6 shows the thick part of the water jet induced by vertically focusing the laser beam into the water (the setup in Chapter 3). As we can see, the vibration on the surface of the thick jet is cylindrical symmetry and the thick jet gradually breaks up into server drops. Additionally, the breakup of thin part of the water jet in Fig. 4.6 has similar result which is not shown. However, when the laser is horizontally focused into the water, the waving on the thin jet with directions parallel to the major and minor axes of the bubble, as depicted in Fig. 4.7(a), will be different to each other due to the great energy distributions of the water breakdown and the bubble parallel to the optical path. This difference can be in phase or amplitude and is similar to the circular or elliptical polarization of an electromagnetic wave. A schematic picture of a circular polarization is shown in Fig. 4.7(b). As a result, the thin jet is rotating or twisting.

As mentioned above, the mechanism of the two arms is apparent when bubble depth is decreased. In Fig. 4.5(a), the frame at the time of $133.3\mu\text{s}$ clearly shows the feature of a surface depression about the formation of the two-arm splash. In Chapter

3, when a laser is focused vertically into the water, a thick jet shows a crown-like structure on its top. We discussed the process of such crown-like structure as followed. The pressure in the bubble is decreasing during its first expansion, and then the bubble start to collapse because its pressure can not counterbalance the external pressure. Such downward collapsing of bubble leads to a depression of the free surface upper the bubble [13,14]. Upon the surface depressing to its maximum depth, the surrounding water flows into the crater of the surface depression and a water jet rises on the free surface [7,13]. Compared to the general case which is only a crater formed during the surface depression [14-17], a thin jet extruded by the first expansion of the bubble causes that a ring-shaped crater is generated around the thin jet, as shown in Fig. 3.6. The collapse of this ring-shaped crater will generate the crown-like water jet. However, the cross image of the ring-shaped crater as shown in the Fig. 3.5 is difficult to observe in the experimental results, as shown in the Fig. 3.4. On the other hand, there are two arms significantly formed on the thick jet when the major axis of the elongated bubble is parallel to the surface plane, which leads to easily measure the off-axis craters located aside the thin jet. The zoom-in pictures around the surface depression of Fig. 4.5(a) is shown in Fig. 4.5(b). We can clearly see that the surface depression is not only a crater appeared on the free surface. The thin jet at the center of the surface depression causes a pair of off-axis crater, which has radially outward motion during its collapse, as indicated by the two outward arrows in Fig. 3.5.

When the bubble depth is further decreased to $\gamma = 0.63$, the bottom of the thin jet becomes a sheet of isosceles triangle with top angle about 24° , as shown in the first low of Fig. 4.8. This structure is confirmed in sheet because the back light can directly penetrate though a plane except the edge of the plane which reflects the back light and appears in dark. For this sheet formation, as mentioned above, the elongated bubble

firstly expands to a near spherical bubble in infinite surrounding and the thin jet is extruded during this first expansion when the bubble is beneath a free surface. Thus the thin jet should be initially in cylindrical symmetry. Next, as shown in the frames at $133\mu\text{s}$ to $166\mu\text{s}$ in Fig. 4.8, the bottom of the thin jet becomes “fat” after the rising of the thick jet. Furthermore, when the two arms are not symmetry to each other, the thin jet will not be an isosceles triangle, as shown in Fig. 4.9 in which the focus length of laser is altered to be 120mm. In the first frame in Fig. 4.9, the shape of the elongated bubble is twist compared to Fig. 4.4 due to the energy distribution around the focus volume induced by increasing the focus length, and then the two arms will not symmetry to each other. As a result, we consider that the thin jet could be pulled outward by the opposite arms and becomes a sheet in structure. The sheet part of the thin jet gradually shrinks and mixes with the upward moving thick jet, and finally, the thin jet converts back to a cylindrical shape, as shown in the second row of Fig. 4.8 which shows that the isosceles triangle analogously sinks into the thick jet. When bubble depth $\gamma = 0.55$, due to the raising of surface interaction between the bubble and free surface, the third row of Fig. 4.10 shows that the thick jet is also pulled into a plane structure. The surface tension of the thick jet tends to decrease the area of the plane by shrinking the thick jet back to a cylinder-like structure. Finally, for more shallow bubble depth, the two-arm splash has no definite structure and the thin jet rapidly breaks into multiple drops, as shown in the second row of Fig. 4.10.

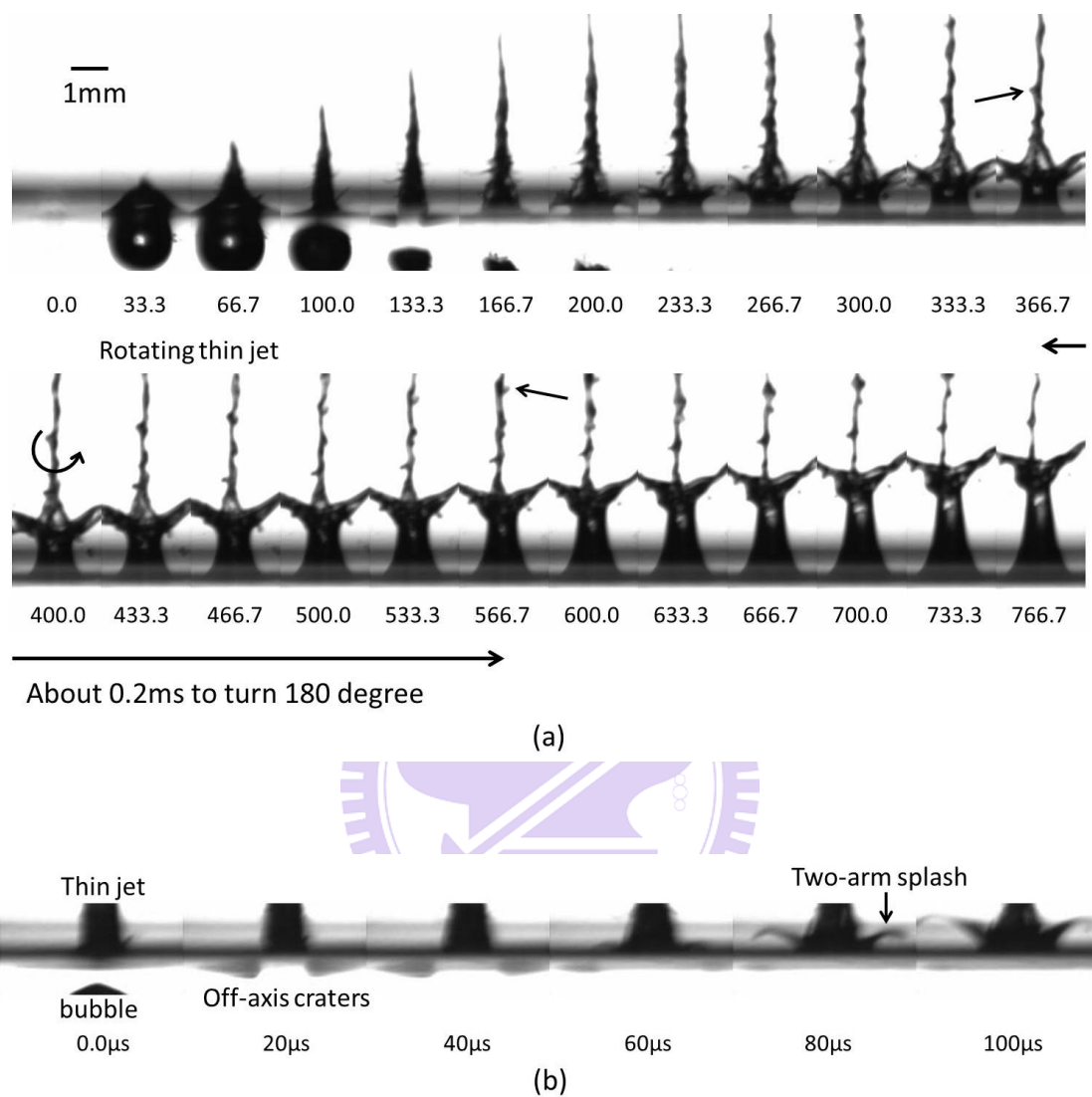


Fig. 4.5(a) The water jet for $\gamma = 0.73$. The exposure time is $10\mu\text{s}$ and the time (in μs) is indicated at the bottom of each frame. The thin jet analogously rotates like drill. (b) The zoom-in pictures around the surface depression. The frame rate is 50,000 and the shutter speed is $3\mu\text{s}$. The time (in μs) is indicated at the bottom of each frame.

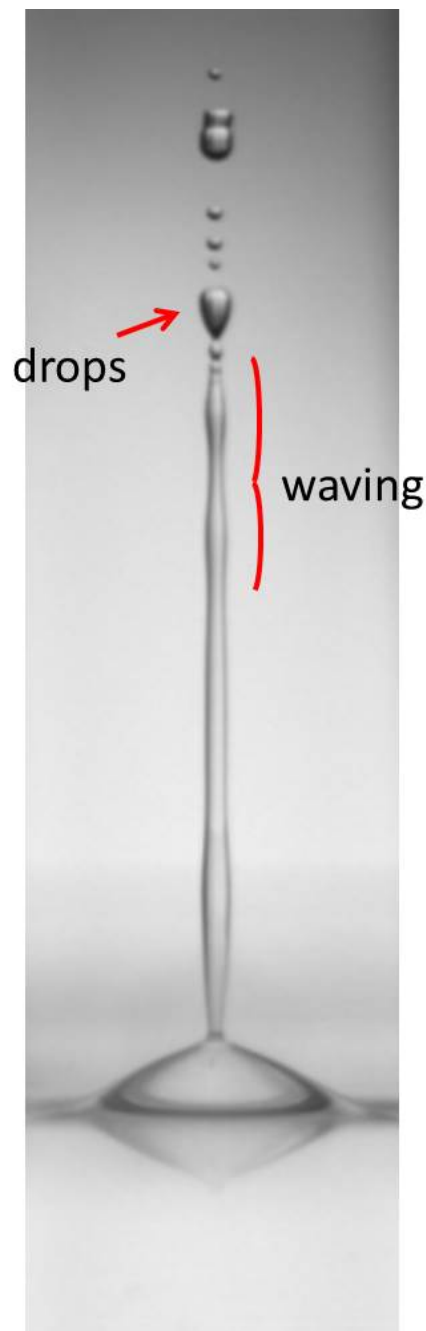


Fig. 4.6 The breakup of the thick part of the water jet induced by vertically focusing the laser beam beneath the free water surface. The waving on the thick jet is cylindrical symmetry and the thick jet gradually breaks up into several drops. Additionally, the breakup of the thin part of the water jet has similar result.

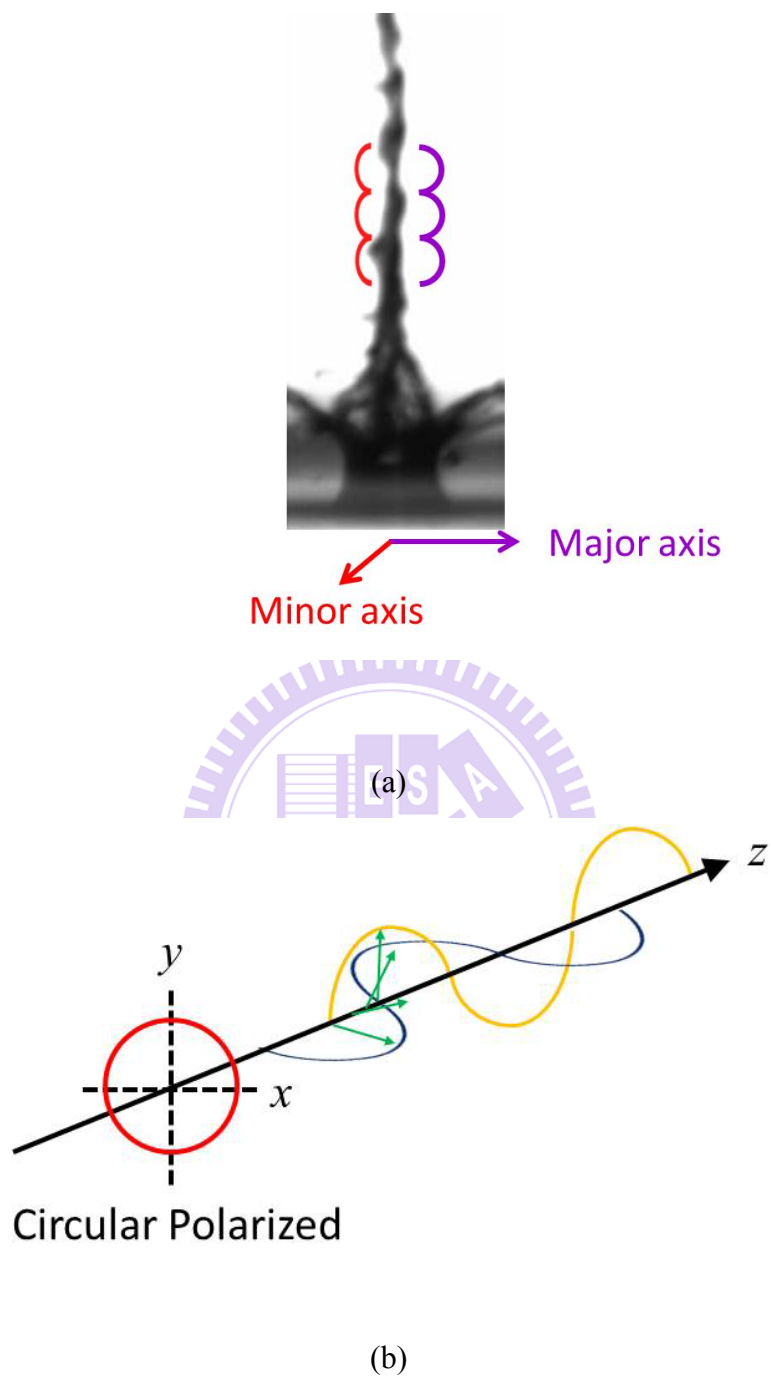


Fig. 4.7(a) The vibrations on the thin jet with directions on major and minor axes are unmatched to each other. (b) The schematic of the circular polarized of an electromagnetic wave.

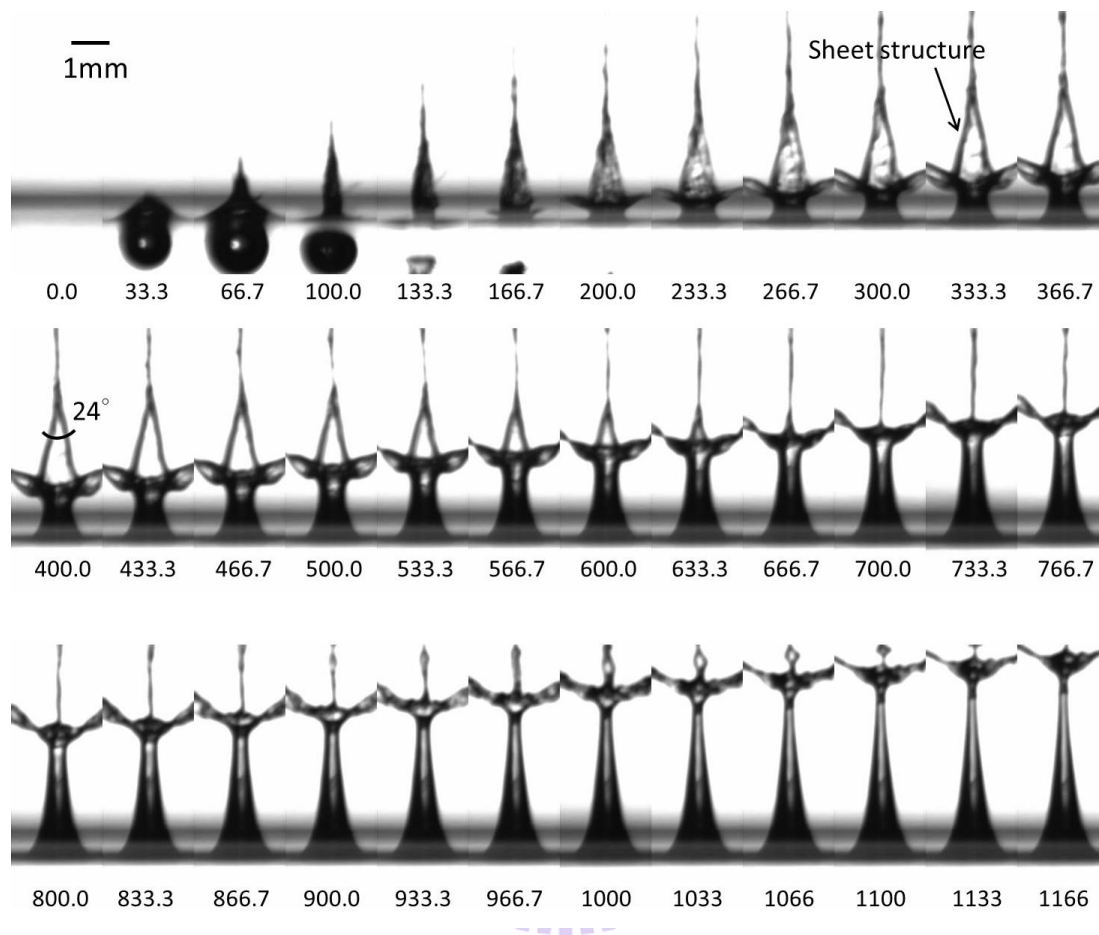


Fig. 4.8 The water jet for $\gamma = 0.63$. The exposure time is $10\mu\text{s}$ and the time (in μs) is indicated at the bottom of each frame. The thin jet is pulled outward by the two arms and forms a sheet structure.

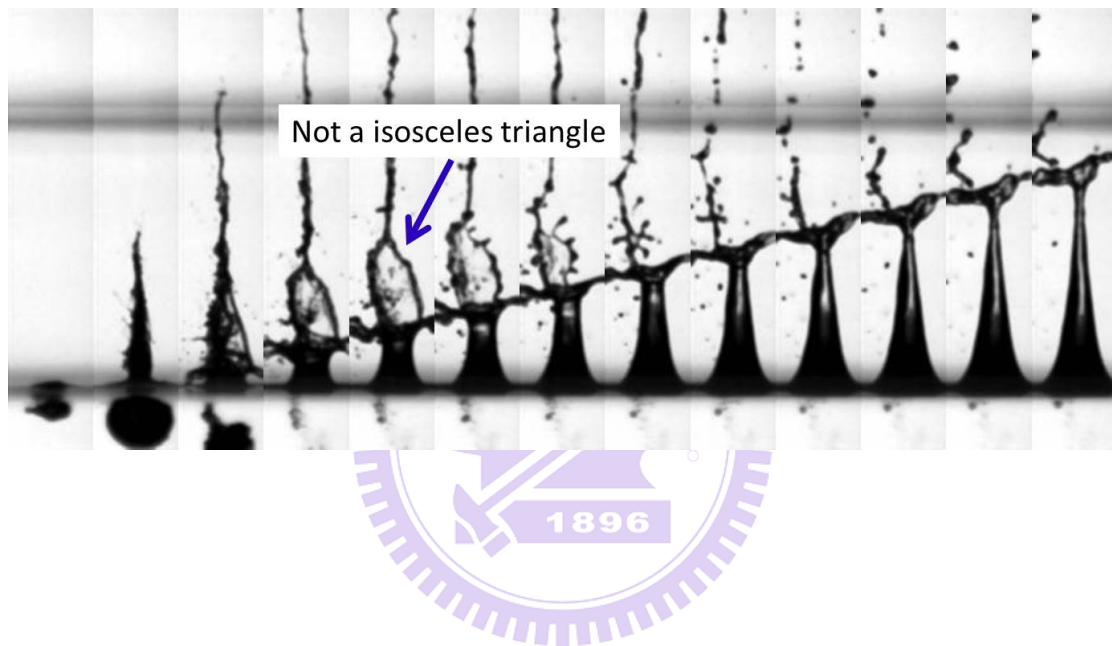


Fig. 4.9 A sheet thin jet with shape in non-isosceles triangle is generated when the laser is focused with focus length in 120mm. As we can see in the first frame, the shape of the elongated bubble is twist due to the energy distribution around the focus volume induced by increasing the focus length.

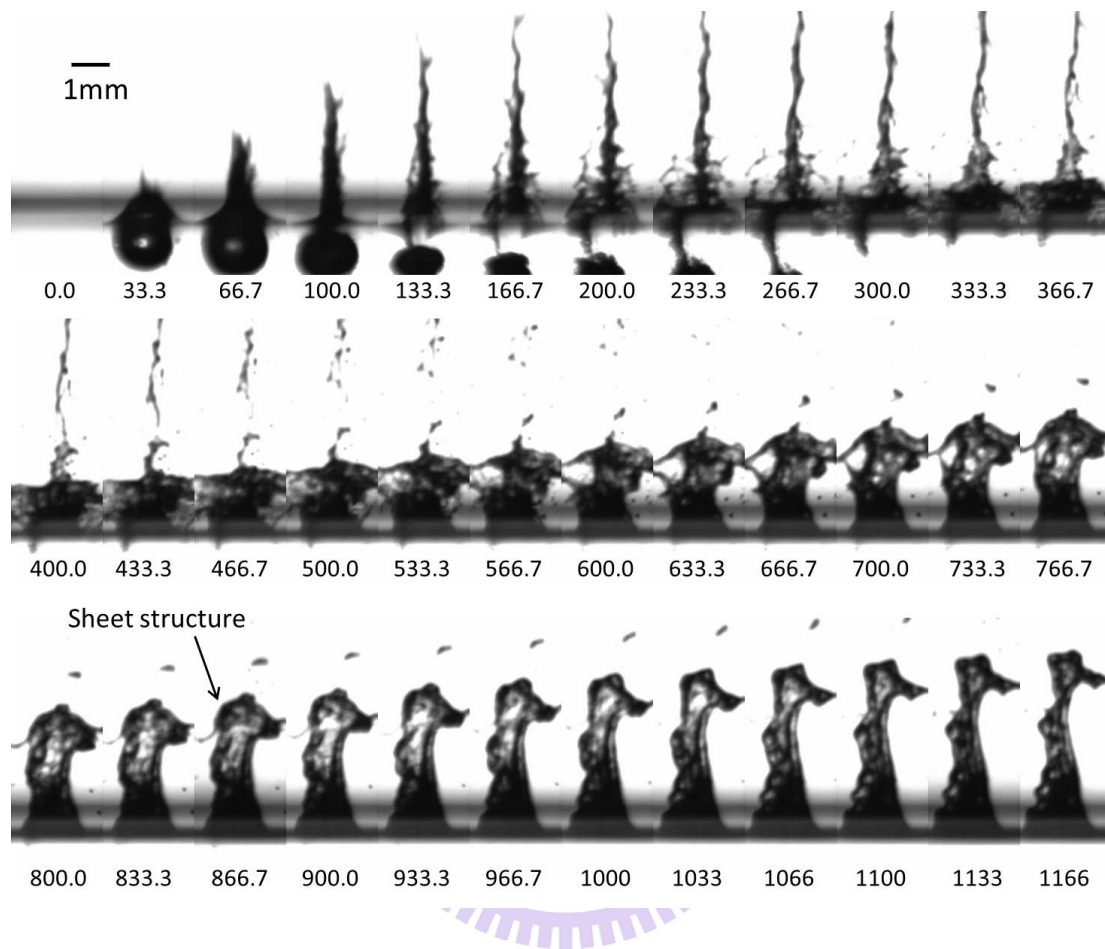


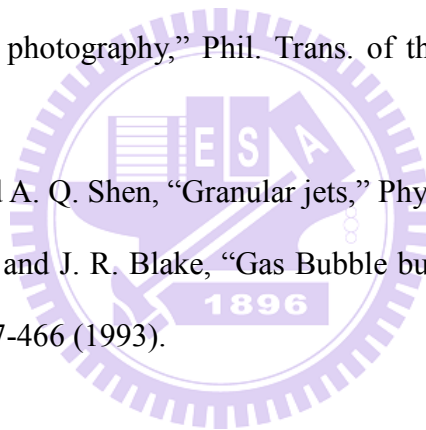
Fig. 4.10 The water jet for $\gamma = 0.55$. The exposure time is $10\mu\text{s}$ and the time (in μs) is indicated at the bottom of each frame. The thick jet shows a sheet structure and gradually shrinks back to a cylinder-like structure.

Reference

- [1] J. Eggers and E. Villermaux, Rep. Prog. Phys. **71**, 036601 (2008).
- [2] B. Karri, S. R. G. Avila, Y. C. Loke, S. J. O'Shea, E. Klaseboer, B. C. Khoo, and C. D. Ohl, "High-speed jetting and spray formation from bubble collapse," Phys. Rev. E **85**, 015303 (2012).
- [3] N. Bremond, C. Clanet, and E. Villermaux, "Atomization of undulating liquid sheets," J. Fluid Mech. **585**, 421–456 (2007).
- [4] N. Bremond and E. Villermaux, "Atomization by jet impact," J. Fluid Mech. **549**, 273–306 (2006).
- [5] W. Lauterborn and T. Kurz, "Physics of bubble oscillations." Rep. Prog. Phys. **73**, 106501 (2010).
- [6] Y. L. Chen, J. W. L. Lewis, and C. Parigger, "Spatial and temporal profiles of pulsed laser-induced air plasma emissions," J. Quant. Spectrosc. Ra. **67**, 91-103 (2000).
- [7] Ross C. C. Chen, Y. T. Yu, K. W. Su, J. F. Chen, and Y. F. Chen, "Exploration of water jet generated by Q-switched laser induced water breakdown with different depths beneath a flat free surface," Opt. Express, **21**, 445-453 (2013).
- [8] G. L. Chahine, "Interaction between an oscillating bubble and a free surface," Trans. ASME I: J. Fluids Eng. **99**, 709-715 (1977).
- [9] A. Pain, B. H. T. Goh, E. Klaseboer, S. W. Ohl, and B. C. Khoo, "Jets in quiescent bubbles caused by a nearby oscillating bubble," J. Appl. Phys. **111**, 054912 (2012).
- [10] J. A. F. Plateau, *Statique expérimentale et théorique des liquides soumis aux seules forces moléculaires* (Gauthier-Villard, Paris, 1873).
- [11] L. Rayleigh, "On the Capillary Phenomena of Jets," Proc. R. Soc. London **29**,

71-97 (1879).

- [12] D. F. Rutland and G. J. Jameson, “A non-linear effect in the capillary instability of liquid jets,” *J. Fluid Mech.* **46**, 267-271, (1971).
- [13] M. Duocastella, A. Patrascioiu, J. M. Fernández-Pradas, J. L. Morenza, and P. Serra, “Film-free laser forward printing of transparent and weakly absorbing liquids,” *Opt. Express* **18**(21), 21815-21825 (2010).
- [14] B. W. Zeff, B. Kleber, J. Fineberg, and D. P. Lathrop, “Singularity dynamics in curvature collapse and jet eruption on a fluid surface,” *Nature* **403**, 401-404 (2000).
- [15] A. M. Worthington and R. S. Cole, “Impact with a liquid surface, studied by the aid of instantaneous photography,” *Phil. Trans. of the Roy. Soc.* **189**, 137-148 (1897).
- [16] S. T. Thoroddsen and A. Q. Shen, “Granular jets,” *Phys. Fluids* **13**, 4-6 (2001).
- [17] J. M. Boulton-Stone and J. R. Blake, “Gas Bubble bursting at a free surface,” *J. Fluid Mech.* **254**, 437-466 (1993).



Chapter 5. Summary and Future works

The factors transverse-confinement structure of oxide-aperture and dominant longitudinal wave vector k_z of VCSEL are important to directly observe the near-field pattern for analogously studying a high-order wave pattern in quantum billiard. In this work, we use large-aperture square and equal triangular VCSELs to study the wave pattern of each shape of billiard system. Addition to the fundamental eigenmodes such as the Chessboard-like (bouncing ball) mode in square billiard and honeycomb mode in triangular billiard, when the temperature of VCSEL is decreased, the pumping current distribution of the VCSEL causes superscar modes which has interference pattern localized on classical periodic orbits such as diamond-like orbits in square billiard and (1,1) mode in triangular billiard. These measurements are theoretically reconstructed very well by the eigenfunctions of an infinite potential well and the superposition of coherent states. Furthermore, we study the characteristics of the directional emission in far field and the morphology of the evolution from near field to far field. The measurements of large-aperture equilateral-triangular VCSEL show the directional emission of far field from a honeycomb eigenmode is very similar to the superscar (1,1) mode, although the near fields are completely visually different to each other. As a result, the far-field directional emission from a microcavity is just a necessary not sufficient condition for the emergence of a superscar mode. This result is confirmed in experimental finding and numerical simulation, and has been published in Optics Letters, Volume 34, Number 12, 2009 [1]. Contrast to the classical limit, the free-space propagations of the superscars show an additional direction on the rebounding region parallel to the

boundary edge. Furthermore, the interference structures on the diffraction pattern result to the fascinating Star of David on the far field from large-aperture equilateral-triangular VCSEL.

In chapter 3 and 4, we study the water splash generated by laser-induced breakdown beneath a free surface. The water jet can be divided into a thin jet and a thick jet with crown-like structure on its top. The mechanisms and features of each part of the water jet with different bubble depths are studied in detail and have been published in *Optics Express*, Volume 21, Number 1, 2013 [2]. The crown-like structure becomes a pair of arm when the laser is horizontally focused beneath the free surface. Based on this morphology changing, we can clearly observe the formation of this crown-like structure and two-arm splash. Addition to the two-arm splash, the water jet shows a rotating thin jet and sheet thin jet when the laser is horizontally focused beneath the free surface.

A well control water jet induced by laser is necessary for several laser applications such as laser printing [3] and drug delivery [4]. Based on the knowledge of the mechanism of the water jet by this work, we can further explore the methods for controlling the water jet, for example, bubble shaping or implemented a transverse boundary beneath the free surface to change the structure of the water jet, as shown below in which the boundary is a equilateral triangular. As we can see, the crown-like structure forms three arms which are perpendicular to the three edges of the triangular boundary, respectively.

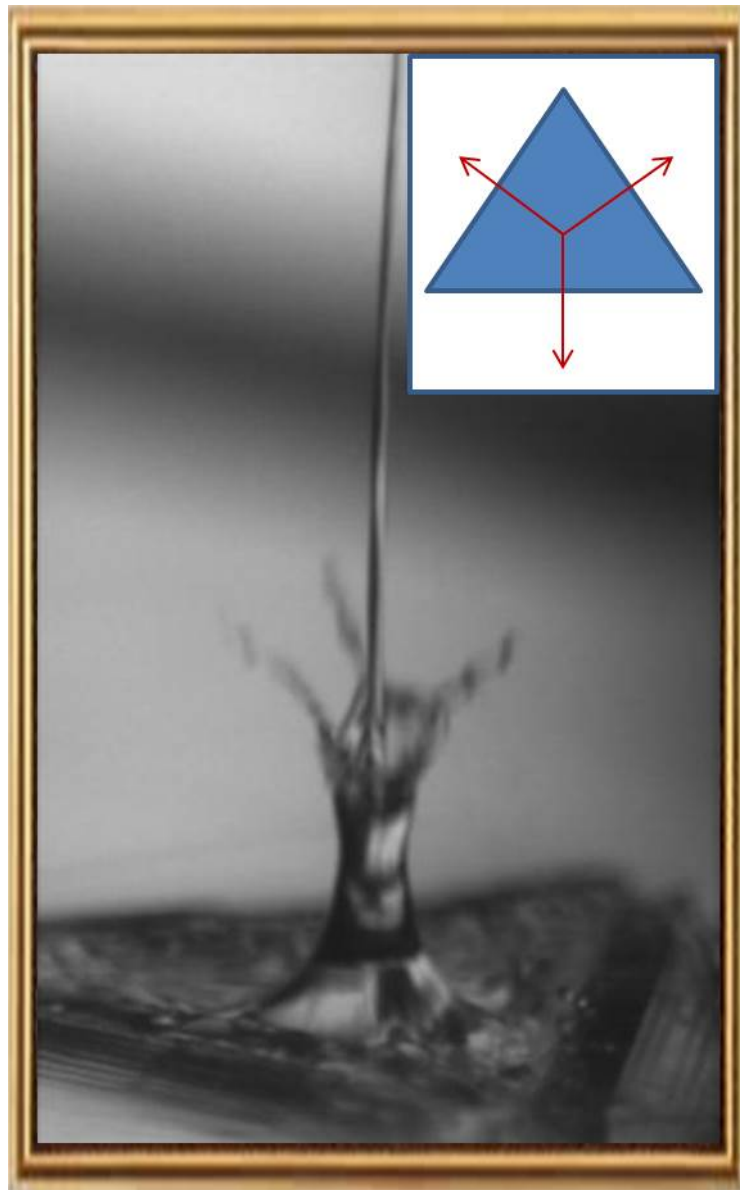


Fig. 5.1 A laser-induced water jet is generated by vertically focusing the laser beam beneath a free surface with a lateral equilateral triangular boundary inserted below the free surface. There are three arms forms on the crown, which are perpendicular to the three edges of the triangle, respectively.

Reference

- [1] Ross C. C. Chen, Y. T. Yu, Y. J. Huang, C. C. Chen, Y. F. Chen, and K. F. Huang, “Exploring the origin of the directional emission from a microcavity with a large-aperture surface-emitting laser,” *Opt. Lett.* **34**(12) (2009).
- [2] Ross C. C. Chen, Y. T. Yu, K. W. Su, J. F. Chen, and Y. F. Chen, “Exploration of water jet generated by Q-switched laser induced water breakdown with different depths beneath a flat free surface,” *Opt. Express*, **21**, 445-453 (2013).
- [3] M. Duocastella, A. Patrascioiu, J. M. Fernández-Pradas, J. L. Morenza, and P. Serra, “Film-free laser forward printing of transparent and weakly absorbing liquids,” *Opt. Express* **18**(21), 21815–21825 (2010).
- [4] T. Hirano, M. Komatsu, H. Uenohara, A. Takahashi, K. Takayama, and T. Yoshimoto, “A novel method of drug delivery for fibrinolysis with Ho:YAG laser-induced liquid jet,” *Lasers Med. Sci.* **17**, 165–172 (2002).

Appendix A

Free space propagation of a paraxial ray

In free space propagation, specially, the paraxial optic such as laser optic, the approximation from wavelength on longitudinal smaller than the one on transverse leads to the Fresnel diffraction. By the analogy between paraxial optics and non-relativistic quantum mechanics, it was showed that the transient wave function has remarkable temporary interference pattern analogous to the spatial diffraction pattern of light diffracted by a sharp edge. This property of diffraction in time space, as result, called diffraction in time which is first proposed by Moshinsky [1]. The experiment of diffraction in time can be extended to several systems for example atom cooling, neutrons [2], electrons [3], Bose-Einstein condensates [4]. The significant in diffraction in time is not only the scientific studies but also the application related to the transient response of abrupt changes of potential in quantum device [5,6].

For an electromagnetic wave in free space, assume the vector field is time harmonic with an amplitude $\psi(x, y, z)$, the amplitude $\psi(x, y, z)$ term would obey Helmholtz equation:

$$\nabla^2 \psi + k^2 \psi = 0 \tag{A.1}$$

Apply the paraxial wave which the propagation vector k is inclined by a small angle with respect to the z axis, that k_z can be approximated as below,

$$kz = \sqrt{k^2 - k_x^2 - k_y^2} \approx k - \frac{k_x^2 + k_y^2}{2k}. \quad (\text{A.2})$$

and $\psi(x, y, z) = u(x, y, z)e^{-jkz}$, where $u(x, y, z)$ is amplitude distribution.

At any plane of z , the $u(x, y, z)$ can be implemented by superposition of the plane waves which plane waves have amplitude $U_0(k_x, k_y)$ with particular transverse components of k_x and k_y at $z = 0$ plane.

$$u(x, y, z) = \int_{-\infty}^{\infty} dk_x \int_{-\infty}^{\infty} dk_y U_0(k_x, k_y) e^{-j(k_x x + k_y y)} e^{j[(k_x^2 + k_y^2)/2k]z} \quad (\text{A.3})$$

Because conversion between the coordinate and momentum space is the Fourier transform, the $U_0(k_x, k_y)$ can be displayed,

$$U_0(k_x, k_y) = \left(\frac{1}{2\pi}\right)^2 \int_{-\infty}^{\infty} dx_0 \int_{-\infty}^{\infty} dy_0 u_0(x_0, y_0) e^{j(k_x x_0 + k_y y_0)} \quad (\text{A.4})$$

Combine (A.3) and (A.4), one has

$$u(x, y, z) = \int_{-\infty}^{\infty} dx_0 \int_{-\infty}^{\infty} dy_0 u_0(x_0, y_0) \left(\frac{1}{2\pi}\right)^2 \int_{-\infty}^{\infty} dk_x \int_{-\infty}^{\infty} dk_y e^{-j[k_x(x-x_0) + k_y(y-y_0)]} e^{j[(k_x^2 + k_y^2)/2k]z} \quad (\text{A.5})$$

This expression shows the convolution of $u_0(x_0, y_0)$ with the *Fresnel kernel*

$$h(x, y, z) = \left(\frac{1}{2\pi}\right)^2 \int_{-\infty}^{\infty} dk_x \int_{-\infty}^{\infty} dk_y e^{-j[k_x x + k_y y]} e^{j[(k_x^2 + k_y^2)/2k]z} \quad (\text{A.6})$$

The integral can be carried out by completion of the square in the exponent.

$$\int_{-\infty}^{\infty} dk_x e^{-jk_x x} e^{j(k_x^2/2k)z} = \sqrt{\frac{jk}{z}} e^{-j(kx^2/2z)} \int_{-\infty}^{\infty} d\xi e^{-\xi^2/2} = \sqrt{\frac{2\pi jk}{z}} e^{-j(kx^2/2z)} \quad (\text{A.7})$$

Where $\xi^2 = -j \frac{[k_x - k(x/z)]^2 z}{k}$

The derivation on k_y is the same as k_x , as a result, the $h(x, y, z)$:

$$h(x, y, z) = \frac{j}{\lambda z} e^{-j(x^2+y^2/2z)} \quad (\text{A.8})$$

The above equation (A.8) introduced in (A.5) gives the well know *Fresnel diffraction integral* in the paraxial approximation

$$u(x, y, z) = \frac{j}{\lambda z} \int_{-\infty}^{\infty} dx_0 \int_{-\infty}^{\infty} dy_0 u_0(x_0, y_0) e^{-j(k/2z)[(x-x_0)^2+(y-y_0)^2]} \quad (\text{A.9})$$

Next, Fraunhofer diffraction is the limit of the Fresnel diffraction when the distance of z from the plane with $u_0(x_0, y_0)$ approaches to infinity. In this limit, the term $(x-x_0)^2+(y-y_0)^2$ in the exponential term in equation (A.9) is approximated:

$$(x-x_0)^2+(y-y_0)^2 \approx (x^2+y^2)-2xx_0-2yy_0 \quad (\text{A.10})$$

Because the far-field pattern ideally expands to infinity which means $x(y) \gg x_0(y_0)$. Actually, the Fraunhofer diffraction is valid enough when the amplitude distribution in the near-field pattern extends over a transverse dimension

$$d \ll \sqrt{\frac{z}{k}}$$

The approximation in (A.10) gives the amplitude distribution in far field:

$$u(x, y, z) = \frac{j}{\lambda z} e^{-j(k/2z)(x^2+y^2)} \int_{-\infty}^{\infty} dx_0 \int_{-\infty}^{\infty} dy_0 u_0(x_0, y_0) e^{j(k/z)(xx_0+yy_0)} \quad (\text{A.11})$$

Apparently, the integral over x_0 and y_0 is the same as the Fourier transform of $u_0(x_0, y_0)$. That is why the correlation between near field and far field is related to the coordinate and momentum space.

Appendix B

Boundary Integral Method

Figure B.1 shows the schematic representation of the bubble inside a liquid domain and beneath an infinity expansion free surface. The problem is an axisymmetric cylindrical coordinate system in which the r and z denote the radial and vertical axis of a cylindrical polar coordinate. It should be noted that the normal vectors \hat{n} are outward from liquid across the free space to air domain or the vapor cavity of the bubble.

For simplifying the simulation, we assume the fluid domain is incompressible which is valid when the shock wave generation is poor or its speed in liquid are much smaller than the speed of sound in liquid. For incompressible fluid, the potential of velocity must be satisfied the Laplace's equation

$$\nabla^2 \phi = 0. \quad (\text{B.1})$$

The other assumptions are non-viscous and no surface tension. However, the process of smoothing on the boundary for convergent results (not discussed in detail) has the same effect with surface tension. Next, we introduce the Navier-Stokes equation for time evolution applied to the dynamic of bubble in an axisymmetric cylindrical coordinate.

The solution of Laplace's equation of a smooth boundary surface S in a domain Ω can be derived by the Green's integral formula from the Green's second identity, as shown below:

$$c(p)\phi(p) = \oint_S G(p, q) \frac{\partial \phi(q)}{\partial n} - \phi(q) \frac{\partial G(p, q)}{\partial n} da \quad (\text{B.2})$$

Where $G(p, q) = \frac{1}{|p - q|}$; $p \in \Omega \cap S$ is the observe point; $q \in S$ is the point on the boundary; and

$$c(p) = \begin{cases} 4\pi, & \forall p \in \text{fluid domain } \Omega \\ 2\pi, & \forall p \in \text{smooth boundary surface } S \\ \neq 2\pi, & \forall p \in \text{nonsmooth boundary surface } S \end{cases} \quad (\text{B.3})$$

From the cylindrical coordinate in Fig. B.1, the $G(p, q)$ is derived,

$$G(p, q) = \frac{1}{\sqrt{(r_p + r_q)^2 + (z_p - z_q)^2 - 4r_p r_q \cos(\theta/2)}} \quad (\text{B.4})$$

And the normal vector \hat{n} :

$$\begin{aligned} \hat{n} &= \hat{l} \times \hat{\theta} \\ &= \left(\frac{\partial r}{\partial l} \cos(\theta), \frac{\partial r}{\partial l} \sin(\theta), \frac{\partial z}{\partial l} \right) \times (-\sin(\theta), \cos(\theta), 0) \\ &= \left(-\frac{\partial z}{\partial l} \cos(\theta), -\frac{\partial z}{\partial l} \sin(\theta), \frac{\partial r}{\partial l} \right) \end{aligned} \quad (\text{B.5})$$

So the normal derivate of $G(p, q)$:

$$\begin{aligned} \frac{\partial G(p, q)}{\partial n} &= \frac{(r_p - r_q \cos(\theta), r_q \sin(\theta), z_p - z_q) \cdot \left(-\frac{\partial z}{\partial l} \cos(\theta), -\frac{\partial z}{\partial l} \sin(\theta), \frac{\partial r}{\partial l} \right)}{\left[\sqrt{(r_p + r_q)^2 + (z_p - z_q)^2 - 4r_p r_q \cos(\theta/2)} \right]^3} \\ &= \frac{\frac{\partial z}{\partial l} r_p \cos(\theta) - \frac{\partial z}{\partial l} r_q - \frac{\partial r}{\partial l} (z_p - z_q)}{\left[\sqrt{(r_p + r_q)^2 + (z_p - z_q)^2 - 4r_p r_q \cos(\theta/2)} \right]^3} \end{aligned} \quad (\text{B.6})$$

Due to the cylindrical symmetry, the integral by surface area can be simplified by firstly integrating the parameter θ . As a result,

$$\oint_S G(p, q) da = \int_{\Delta l} dl \frac{4r_q}{\sqrt{(r_p + r_q)^2 + (z_p - z_q)^2}} K(k) \quad (\text{B.7})$$

$$\oint_S \frac{\partial G(p, q)}{\partial n} da = \int_{\Delta l} dl \frac{4r_q \left\{ \left[\frac{dz}{dl} (r_p + r_q) + \frac{dr}{dl} (z_p - z_q) - \frac{2}{k^2} \frac{dz}{dl} r_p \right] \frac{E(k)}{1 - k^2} + \frac{2}{k^2} \frac{dz}{dl} r_p K(k) \right\}}{\left[\sqrt{(r_p + r_q)^2 + (z_p - z_q)^2} \right]^3} \quad (\text{B.8})$$

where $k^2 = \frac{4r_p r_q}{(r_p + r_q)^2 + (z_p - z_q)^2}$ and the $K(k)$, $E(k)$ are the complete elliptic integral of the first and second kind, respectively.

For numerically calculating the integration, we take N collocation points with index j on the surface, and the surface integral is then divided into a set of segments in which the end points on each segment are the N collocation points.

$$2\pi\phi_i + \sum_j \int_{S_j} \phi_j \frac{\partial G(p_i, q_j)}{\partial n} dl = \sum_j \int_{S_j} \frac{\partial \phi_j}{\partial n} G(p_i, q_j) dl \quad (\text{B.9})$$

The curve in each segment of line integration is approximated by cubic spline. The potential ϕ and the $\frac{\partial \phi}{\partial n}$ is approximated by linear interpolation from the end points of each segment. Finally, a matrix form $H\phi = G \frac{\partial \phi}{\partial n}$ is derived and can be used to calculate the normal derivate of velocity potential which is just the normal velocity on the boundary. Combined with the tangential velocity which is derived from the approximation of cubic spline, the velocity on the boundary can be derived for equation of motion in the time evolution.

The boundary dynamics of bubble and free surface are derived from the Bernoulli equation,

$$\rho \frac{\partial \mathbf{V}}{\partial t} + \rho \frac{1}{2} \nabla \mathbf{V}^2 = -\nabla \mathbf{P} + \rho \vec{g} \quad (\text{B.10})$$

The viscosity is neglected. Then, the \mathbf{V} is replaced by $\mathbf{V} = \nabla \phi$ and we assume that the ambient pressure is a constant P_∞ at z_∞ . This reference point of z_∞ is the initial central point of the bubble in our simulation.

$$\begin{aligned} \Rightarrow \rho \frac{\partial \nabla \phi}{\partial t} + \frac{\rho}{2} \nabla |\nabla \phi|^2 &= -\nabla \mathbf{P} + \rho \vec{g} \\ \Rightarrow \rho \frac{\partial \phi}{\partial t} + \frac{\rho}{2} |\nabla \phi|^2 &= -(P_{bubble} - P_\infty) + \rho g(z_{bubble} - z_\infty) \end{aligned} \quad (\text{B.11})$$

The pressure in the liquid domain on the boundary of bubble can be a constant pressure vapor bubble (Rayleigh, 1917 [7]), a vapor bubble (Theofanous, 1969 [8]) and ideal gas bubble with different polytropic indices (Soh and Shervani-Tabar, 1992a, 1992b and 1994 [9-11]). The unsteady Bernoulli equation of velocity potential is rewrite,

$$\begin{aligned} P_{bubble} &= P_{vapor} + P_o \left(\frac{V_o}{V} \right)^\kappa \\ \Rightarrow \frac{\partial \phi}{\partial t} + \frac{1}{2} |\nabla \phi|^2 &= -\frac{1}{\rho} \left[P_{vapor} + P_o \left(\frac{V_o}{V} \right)^\kappa - P_\infty \right] - g(z_{bubble} - z_\infty) \\ \Rightarrow \frac{\partial \phi}{\partial t} + \frac{1}{2} |\nabla \phi|^2 &= \frac{(P_\infty - P_{vapor})}{\rho} - \frac{P_o}{\rho} \left(\frac{V_o}{V} \right)^\kappa - g(z_{bubble} - z_\infty) \end{aligned} \quad (\text{B.12})$$

and $\frac{\partial \phi}{\partial t} + \frac{1}{2} |\nabla \phi|^2 = -g \cdot z_{free\ surface}$ (B.13) for the free surface.

The polytropic indices κ is 1.2~1.3 for gaseous explosion products resulting from material explosion like TNT explosion and about 1.4 for diatomic ideal gas.

Use the velocity calculated by the method which is described above chapter with the unsteady Bernoulli equation, the finite element method in time:

$$\begin{aligned}r_{i1} &= r_{i0} + V_{i0}^r \Delta t \\z_{i1} &= z_{i0} + V_{i0}^z \Delta t \\ \phi_{i1} &= \phi_{i0} + \left(\frac{\partial \phi}{\partial t} \right)_{i0} \Delta t\end{aligned}\tag{B.14}$$

The procedure of calculation is as following:

- (1) Assuming the initial state of location and potential on the boundary;
- (2) Calculate the velocity on the boundary by the Eq. B.9;
- (3) The next position and potential in a small time step Δt is derived from the unsteady Bernoulli equation,

Repeat from step (2) for the next time step.

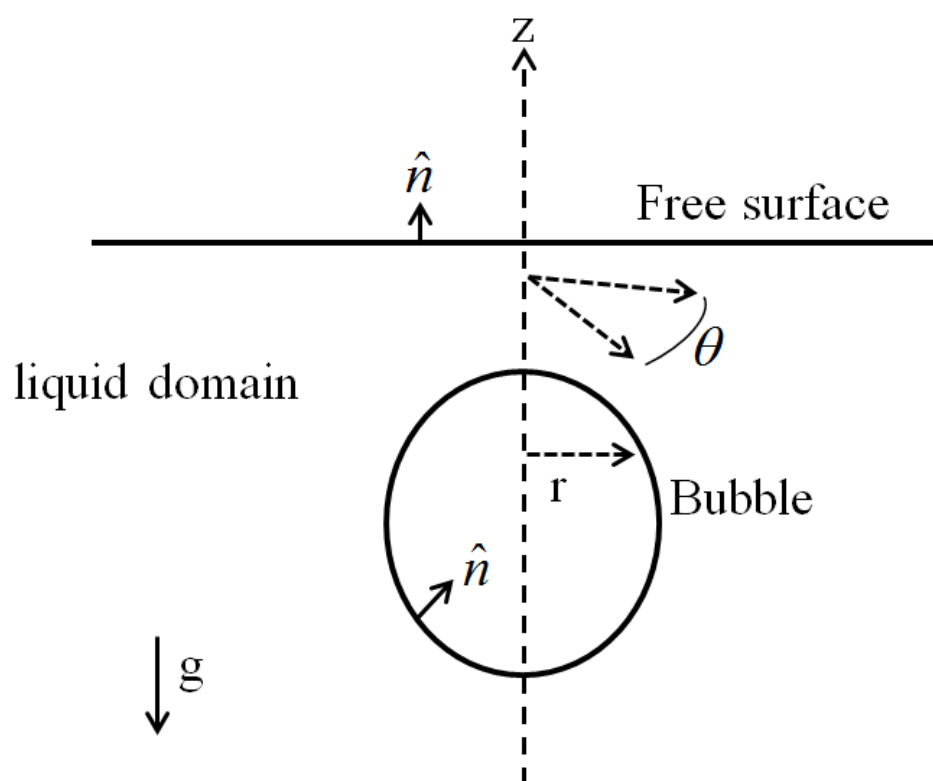


Fig. B.1 The geometry of scheme chosen for constructing the model of pulsation bubble beneath a free surface. The normal vector points out from the fluid domain. The azimuth angle is θ .

Reference for Appendix

- [1] M. Moshinsky, "Diffraction in Time," *Phys. Rev.* **88**, 625-631 (1952).
- [2] T. Hils, J. Felberg, R. Gähler, W. Gläser, R. Golub, K. Habicht, and P. Wille, "Matter-wave optics in the time domain: Results of a cold-neutron experiment," *Phys. Rev. A* **58**, 4784-4790 (1998).
- [3] F. Lindner, M. G. Schätzel, H. Walther, A. Baltuška, E. Gouliemakis, F. Krausz, D. B. Milošević, D. Bauer, W. Becker, and G. G. Paaulus, "Attosecond Double-Slit Experiment," *Phys. Rev. Lett.* **95**, 040401 (2005).
- [4] Y. Colombe, B. Mercier, H. Perrin, and V. Lorent, "Diffraction of a Bose-Einstein condensate in the time domain," *Phys. Rev. A* **72**, 061601R (2005).
- [5] F. Delgado, H. Cruz, and J. G. Muga, "The transient response of a quantum wave to an instantaneous potential step switching," *J. Phys., A: Math Gen.* **35**(48), 10377-10389 (2002).
- [6] F. Delgado, J. G. Muga, D. G. Austing, and G. García-Calderón, "Resonant tunneling transients and decay for a one-dimensional double barrier potential," *J. Appl. Phys.* **97**, 013705 (2005).
- [7] L. Rayleigh, "On the pressure developed in a liquid during the collapse of a spherical cavity," *Phil. Mag.* **34**, 94-98. (1917).
- [8] T. Theofanous, L. Biasi, and H. S. Isbin, "A theoretical study on bubble growth in constant and time-dependent pressure fields," *Chem. Eng. Sci.* **24** 885-897 (1969).
- [9] W. K. Soh and M. T. Shervani-Tabar, "Computer study of unsteady flow around a cavity bubble," *Computational Methods in Engineering; Advances and Applications*, Singapore, 529-534 (1992a).

- [10] W. K. Soh and M. T. Shervani-Tabar, "Computer study on the rebound of a vapour cavity bubble," 11th Australasian Fluid Mechanics Conference, University of Tasmania, Hobart, Australia, 199-202 (1992b).
- [11] W. K. Soh and M. T. Shervani-Tabar, "Computer model for a pulsating vapour bubble near a rigid surface," Computational Fluid Dynamics Journal, **3**(1), 223-236 (1994).

Curriculum Vitae

Personal Data

Name: Ross C. C. Chen

Sex: Male

Birthday: Aug. 4, 1987

Nationality: Taiwan

E-mail: s23hchs@hotmail.com

Mobile Phone: 886-915-510815

Education

2002-2005 National HsinChu Senior High School, HsinChu, Taiwan.

2005-2009 B.S. in Department of Electrophysics, National Chiao Tung University,
HsinChu, Taiwan.

2009-2013 Ph.D. in Department of Electrophysics, National Chiao Tung
University, HsinChu, Taiwan.

Work History

2010-2013 T. A. of Electronics.

Research Interest

Liquid jet formation

Semiconductor Lasers

Electronics

Publication List

1. H. C. Liang, **Ross C. C. Chen**, Y. J. Huang, K. W. Su, and Y. F. Chen, “Compact efficient multi-GHz Kerr-lens modelocked diode-pumped Nd:YVO4 laser, ” *Opt. Express*, **16**(25), 21149-21154 (2008).
2. **Ross C. C. Chen**, Y. T. Yu, Y. J. Huang, C. C. Chen, Y. F. Chen, and K. F. Huang “Exploring the origin of the directional emission from a microcavity with a large-aperture surface-emitting laser, ” *Opt. Lett.* **34**(12), 1810-1812 (2009).
3. C. C. Chen, Y. T. Yu, **Ross C. C. Chen**, Y. J. Huang, K.W. Su, Y. F. Chen, and K. F. Huang, “Transient Dynamics of Coherent Waves Released from Quantum Billiards and Analogous Observation from Free-Space Propagation of Laser Modes, ” *Phys. Rev. Lett.* **102**, 044101 (2009).
4. J. F. Chen, **Ross C. C. Chen**, C. H. Chiang, Y. F. Chen, and Y. H. Wu, “Bimodel onset strain relaxation in InAs quantum dots with an InGaAs capping layer, ” *Appl. Phys. Lett.* **97**, 092110, (2010).
5. J. F. Chen, **Ross C. C. Chen**, C. H. Chiang, M. C. Hsieh, and Y. C. Chang, “Compensation effect and differential capacitance analysis of electronic energy band structure in relaxed InAs quantum dots, ” *J. Appl. Phys.* **108**, 063705 (2010).
6. C.H. Chiang, Y.H. Wu, M.C. Hsieh, C.H. Yang, J.F. Wang, **Ross C.C. Chen**, L. Chang, and J. F. Chen, “Improving the photoluminescence properties of self-assembled InAs surface quantum dots by incorporation of antimony” *Appl. Surf. Sci.* **257**, 8784–8787 (2011).
7. Meng-Chien Hsieh, Jia-Feng Wang, Yu-Shou Wang, Cheng-Hong Yang, and **Ross C. C. Chen**, “Role of the N-related localized states in the electron emission properties of a GaAsN quantum well, ” *J. Appl. Phys.* **110**, 103709 (2011).

8. J. F. Chen, Y. C. Lin, C. H. Chiang, **Ross C. C. Chen**, and Y. F. Chen, “How do InAs quantum dots relax when the InAs growth thickness exceeds the dislocation-induced critical thickness?, ” J. Appl. Phys. **111**, 013709 (2012).
9. **Ross C. C. Chen**, Y. T. Yu, K. W. Su, J. F. Chen, and Y. F. Chen, “Exploration of water jet generated by Q-switched laser induced water breakdown with different depths beneath a flat free surface,” Opt. Express, **21**, 445-453 (2013).
10. **Ross C. C. Chen**, Y. T. Yu, K. W. Su, and Y. F. Chen, Phys. Rev. E (be prepared).